Generation and Processing of Electromagnetic Vortex Beams with Different Orbital Angular Momentum Mode Orders

Der Fakultät für Ingenieurwissenschaften
Abteilung Elektrotechnik und Informationstechnik
Universität Duisburg-Essen

zur Erlangung des akademischen Grades
Doktor der Ingenieurwissenschaften (Dr. -Ing.)

genehmigte Dissertation von
M.Sc. Mohamed Baker Youssef Haj Hassan
aus Libanon

Tag der mündlichen Prüfung: 26.11.2021

Gutachter:
Prof. Dr. sc. techn. Daniel Erni
Prof. Dr. -Ing. Aydin Sezgin

UNIVERSITÄT DUISBURG ESSEN

Open-Minded

marie SFB/TRR 196

Generation and Processing of Electromagnetic Vortex Beams with Different Orbital Angular Momentum Mode Orders

General and Theoretical Electrical Engineering (ATE)
Faculty of Engineering, University of Duisburg-Essen
47048 Duisburg, Germany

Thesis[1] submitted for the degree of
Doctor of Philosophy in Electrical Engineering

presented by
M.Sc. Mohamed Baker Youssef Haj Hassan
born on 01.01.1986 in Lebanon
mohamed.hajhassan@hotmail.de

Day of the oral examination: 26.11.2021

Doctoral supervisor and first reviewer:
Prof. Dr. sc. techn. Daniel Erni
General and Theoretical Electrical Engineering (ATE)
Faculty of Engineering
University of Duisburg-Essen
D-47048 Duisburg, Germany

Doctoral supervisor and second reviewer:
Prof. Dr. -Ing. Aydin Sezgin
Digital Communication Systems (DKS)
Faculty of Electrical Engineering and Information Technology
Ruhr University Bochum
D-44801 Bochum, Germany

[1]This thesis has been carried out in the framework of the DFG Collaborative Research Center / Transregio TRR 196 MARIE (Project-ID 287022738) on Mobile Material Characterization and Localization by Electromagnetic Sensing within the project S03 “Space-Time Signalling for MIMO Reflectometry with Vortex Waves”.

Acknowledgments

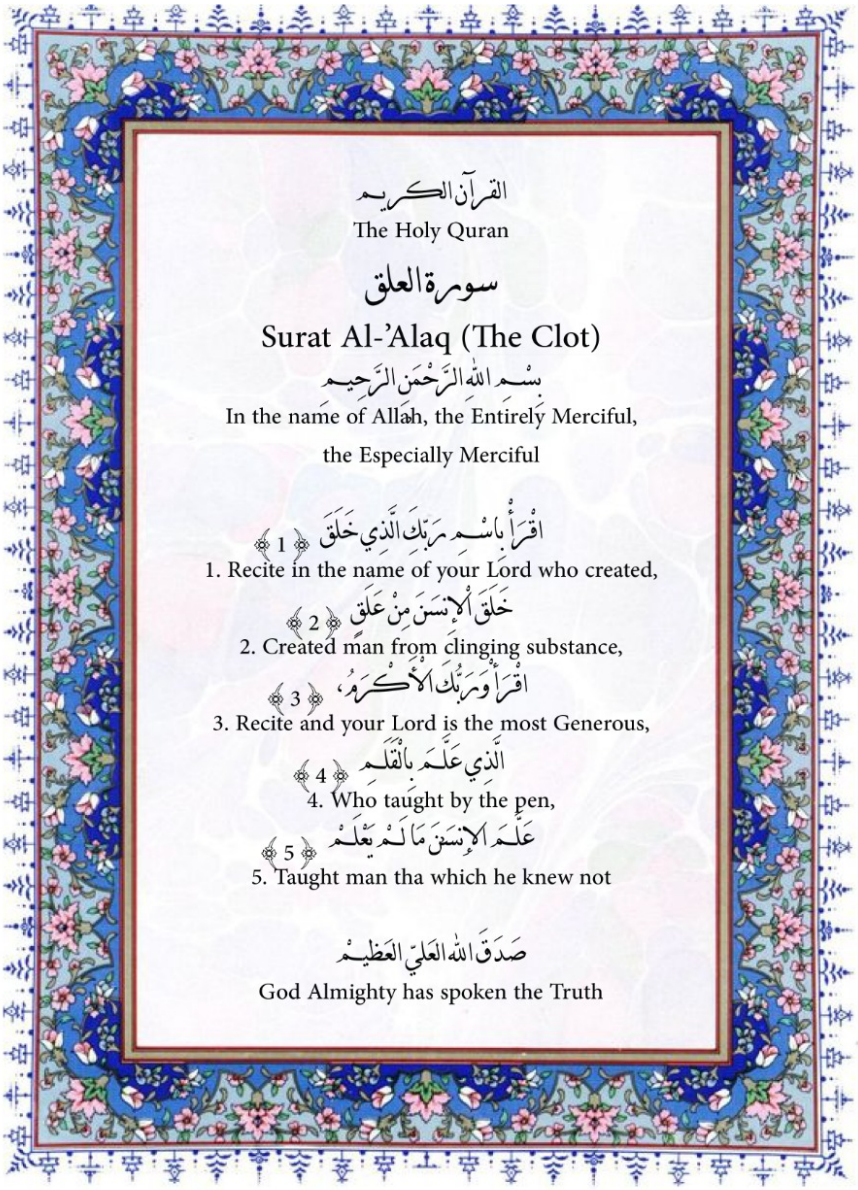
القرآن الكريم

The Holy Quran

سورة العلق

Surat Al-'Alaq (The Clot)

بسم الله الرحمن الرحيم

In the name of Allah, the Entirely Merciful,

the Especially Merciful

اقرأ باسم ربك الذي خلق ﴿1﴾

1. Recite in the name of your Lord who created,

خلق الإنسن من علق ﴿2﴾

2. Created man from clinging substance,

اقرأ وربك الأكرم، ﴿3﴾

3. Recite and your Lord is the most Generous,

الذي علم بالقلم ﴿4﴾

4. Who taught by the pen,

علم الإنسن ما لم يعلم ﴿5﴾

5. Taught man tha which he knew not

صدق الله العلي العظيم

God Almighty has spoken the Truth

Abstract

The permanently and ever-growing request for accurate, efficient, compact, cost-effective, high performance, and novel applications have inspired the researchers to detect new advanced techniques. After the successful deployment of the electromagnetic waves in the last decades in the field of wireless communication (GSM, LTE), sensing, navigation and positioning (GPS), detection and localization (RADAR), identification (RFID), imaging and mapping (SAR), and biomedical engineering (MRI), the vortex waves submit new methods to improve these fields more than the plane waves. Therefore, the vortex waves, also known as Orbital Angular Momentum (OAM) waves, are the main subject in this thesis set under investigation to explore some new approaches that can be applied to wireless technology.

Therefore, in this work, the conventional approach of uniform circular antenna array (UCA) and the elliptical patch approach are set to be compared together to a new approach based on crossed 2λ-dipole antennas (CDA) in order to generate vortex waves. The recent approach is a simple suggestion for generating vortex waves with radial polarization which is performed through using two or four crossed 2λ-dipole antennas. Upon the usage of a reflector, the radiation of this approach can be increased and focused.

Furthermore, an OAM beam steering has been implemented by the aid of uniform circular antenna array in which two different types of phase shifts are required for the beam steering unlike the UCA with subarrays (linear, circular, and rectangular), where three different ones are needed. The two approaches are simulated and studied to achieve better results thus solving the serious issue for OAM wireless communication knowing that the misalignment between the OAM transmitter and the OAM receiver is a very crucial point.

Moreover, the large beam divergence inherent to vortex waves has been reduced by the aid of a new special lens and reflector. Both the tailored lens and reflector are constructed by

an appropriately designed form function rotated around the center axis of the uniform circular antenna array (UCA) to be compared to the conventional one, then showing better simulated and measured results. Further, similar to the misalignment issue, the beam divergence reduction is also crucial for many applications such as wireless communication where the long-distance is seen as an obstacle, or such as the target detection and localization where the beam divergence reduction allows the resolution enhancement of the localization.

Finally, with the aid of helically arranged dielectric resonator arrays, a new application of vortex waves has been developed by converting an incoming OAM mode order m_{in} to an outgoing OAM mode order m_{out}. This application offers likewise improving the code number in the domain of Radio Frequency Identification (RFID) through new multi-valued digits rather than the conventional binary coding $\{0,1\}$. Also, these helically arranged dielectric resonator arrays are characterized by the rejection of the clutter from broadside direction due to the Butler matrix (BM), where the phase shift of the clutter interferes destructively unlike the DR-coded OAM-signal which interferes constructively.

Zusammenfassung

Die permanent und ständig wachsende Nachfrage nach Genauigkeit, Effizienz, Kompaktheit, hoher Qualität, und neuartiger Anwendungen haben die Forscher inspiriert, neue fortschrittliche Techniken zu entdecken. Nach dem erfolgreichen Einsatz der elektromagnetischen Wellen in den letzten Jahrzehnten im Bereich der drahtlosen Kommunikation (GSM, LTE), Sensorik, Navigation und Positionierung (GPS), Erkennung und Lokalisierung (RADAR), Identifizierung (RFID), Bildgebung und Kartierung (SAR), und Medizintechnik (MRI), dienen Spiralwellen als neue Methode, um diese Bereiche zu verbessern. Daher sind die Spiralwellen, auch bekannt als Orbital Angular Momentum (OAM) wellen, das Hauptthema dieser Dissertation. Es sollen neue Ansätze untersucht werden, die sich auf die drahtlose Technologie anwenden lassen.

Deshalb werden in dieser Arbeit der konventionelle Ansatz eines einheitlichen kreisförmigen Antennengruppe (UCA) und der elliptische Patch-Ansatz mit einem neuen Ansatz basierend auf gekreuzten 2λ-Dipolantennen (CDA) verglichen, um Spiralwellen zu erzeugen. Der letzte Ansatz ist ein einfacher Vorschlag zur Generierung von Spiralwellen mit radialer Polarisation, die durch die Verwendung von zwei oder vier gekreuzten 2λ-Dipole Antennen durchgeführt wird. Durch die Verwendung eines Reflektors kann der Gewinn dieses Ansatzes erhöht und fokussiert werden.

Zusätzlich, wurde eine OAM-Strahlschwenkung mit Hilfe einheitlicher kreisförmiger Antennengruppen angewandt, in der zwei verschiedene Arten von Phasenverschiebungen für die Strahlschwenkung erforderlich sind im Gegensatz zur UCA mit Subarrays (linear, kreisförmig und rechteckig), wo drei verschiedene Phasenverschiebungen benötigt werden. Die beiden Ansätze werden simuliert und untersucht, um bessere Ergebnisse zu erzielen und so das ernste Problem für die drahtlose OAM-Kommunikation zu lösen im Wissen, dass die Fehlausrichtung zwischen den OAM Sender und der OAM-Empfänger ein sehr entscheidender Punkt ist.

Außerdem, mit Hilfe einer neuen speziellen Linse und eines neuen Reflektors wurde die inhärente große Strahldivergenz der Spiralwellen reduziert. Die maßgeschneiderten Linse und Reflektor sind durch eine entsprechend gestaltete Formfunktion konstruiert. Diese Funktion wird um die Mittelachse der gleichförmigen kreisförmigen Antennengruppe (UCA) gedreht, was im Vergleich zur konventionellen Linse und Reflektor bessere simulierte und gemessene Ergebnisse zeigt. Wie bei dem Problem der Fehlausrichtung, ist auch die Verringerung der Strahldivergenz entscheidend für viele Anwendungen wie für die drahtlose Kommunikation, wo die große Entfernung als Hindernis angesehen wird, und wie bei der Zielerfassung und -lokalisierung, wo eine hohe Lokalisierungsauflösung notwendig ist.

Zum Schluss durch den Einsatz von spiralförmig angeordneten dielektrischen Resonatoranordnungen, wurde eine neue Anwendung von Spiralwellen entwickelt, indem eine eingehende OAM Mode m_{in} in eine ausgehenden OAM Mode m_{out} umgewandelt wurde. Diese Anwendung bietet eine Erweiterung der Codelänge im Kontext von Radiofrequenz-Identifikation (RFID), wo neue mehrwertige Ziffern anstelle der herkömmlichen binären Code $\{0,1\}$ verwendet wird. Auch diese spiralförmig angeordneten dielektrischen Resonatoranordnungen sind charakterisiert durch die Unterdrückung des Störsignals aus der Breitseitenrichtung. Das liegt an die Butler-Matrix (BM), bei der die Phasenverschiebung des Störsignals destruktiv interferiert, im Gegensatz zu dem DR-Code OAM-Signal, das konstruktiv interferiert.

Contents

List of Figures

List of acronyms

AF	Array Faktor
Balun	Balanced to Unbalanced
BM	Butler Matrix
CDA	Crossed Dipole antenna
DFG	Deutsche Forschungsgemeinschaft
DR	Dielectric Resonator
EM	Electro-Magnetic
FEKO	Feldberechnung für körper mit beliebiger oberfläche
FEM	Finite Element Method
GPR	Ground Penetrating Radar
GPS	Global Positioning System
HFSS	High Frequency Structure Simulator
HP	Holographic Plate
HPBW	Half Power Beamwidth
IEEE	Institute of Electrical and Electronics Engineers
LOS	line of sight
LTE	Long Term Evolution
MIMO	Multiple-Input Multiple-Output
MoM	Method of Moments
MRI	Magnetic Resonance Imaging
MS	Metasurfaces
PCB	Printed Circuit Board
PD	Power Divider

PEC	Perfect Electric Conductor
PP	Polypropylen
OAM	Orbital Angular Momentum
Radar	Radio Detection and Ranging
RCS	Radar Cross Section
RFID	Radio Frequency Identification
SAM	Spin Angular Momentum
SAR	Synthetic Aperture Radar
SLL	Side Lobe Level
SPP	Spiral Phase Plate
SISO	Single-Input Single-Output
UCA	Uniform Circular Array
VNA	Vector Network Analyzer

Chapter 1

Introduction

1.1 Motivation

Many centuries ago, the human being has invested great efforts to improve his life such as in agriculture, industry, trading, medicine, mobility, and communication. The initial type of communication that is still used today, uses the acoustic waves generated by the mouth of the human. However, this type suffers from many issues such as short distance, high efforts, and impermanently availability. Numerous methods have therefore been obtained to facilitate and improve this communication but unfortunately not for the intended purpose until the successful experiment of the electromagnetic waves carried out by the german physicist Heinrich Hertz [1]. Electromagnetic waves have opened crucial access to improve the field of communication and some other areas too.

Not to mention that they carry many types of data in form of applications e.g. data transmission [2], detection and localization [3], identification [4], navigation [5], positioning [6], and imaging [7] (cf. Fig. 1.1). These data are generated with the help of complicated and sophisticated equipment which consists of two interacting parts, namely the software and the hardware part. In the software part, the signals are manipulated to perform specific tasks, while the hardware part provides a convenient environment for the production of these signals. Besides, the hardware part consists of the digital and the analog part whose signals are employed. In the analog part, there are many essential components such as mixers [8], voltage controlled oscillators [9], low noise [10] and power amplifiers [11], filters [12], Butler matrices (BM) [13], power dividers (PD) [14], and antennas [15], where each member plays an active and crucial role. Noting that, the electromagnetic waves are the main component in the wireless communication

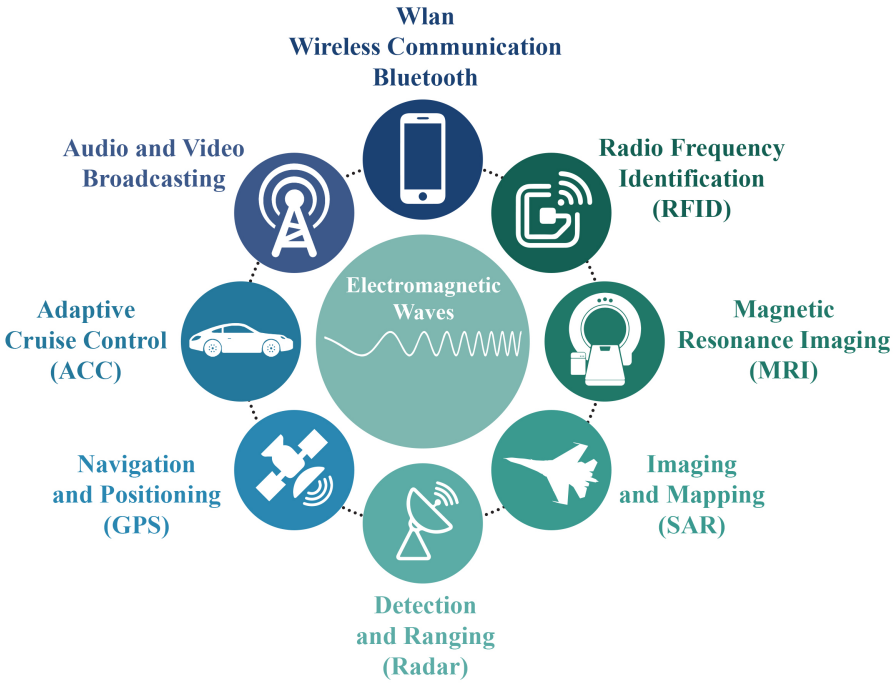

Figure 1.1: Radio frequency applications.

where it is transmitted and received by means of antennas. These antennas act as a converter between the electric current in the metal wires and the EM waves propagating through space. In recent decades, the utilization of EM waves has been intensively researched thus uncovering many successful applications. But for some applications, it still needs further improvement to reduce the costs, increase data rates, reduce the size, and increase the bandwidth of the equipment. After the successful use of vortex waves in the optical regime [16], it has attracted the interest of the researchers to the field of radio-, millimeter-, and terahertz wave technology. Rather than the two conventional states in circular polarized waves $(+1,-1)$, the vortex waves offer an unlimited number of mutual orthogonal OAM mode orders m, which contributes a new degree of freedom to develop and improve the above mentioned areas. This unlimited number of OAM mode orders opens a further door to enhance the data rate where many OAM mode orders are used to transmit multiple signals carrying the same frequency and within the same time interval. Hence, enhancing the capacity and spectral efficiency is attained [17]. Also, the vortex waves establish a new spatial division multiplexing method (OAM-MDM) [18], which can be also combined with the other multiplexing methods (frequency, time, coding, and polarization) yielding an enormous enhancement in the data transmission technology. Besides the unlimited number of OAM mode orders, the OAM waves are characterized with the high beam divergence which can be useful for some applications yet lack efficacy for others. These applications are successfully

studied and researched whereas some new regimes are not studied yet such as the area of medical engineering, navigation, ground penetration radar (GPR), guidance, or maybe a rescue system.

The optical vortex waves have presented some expectation in the field of chirality of a molecular system, where the vortex waves can deal with the chirality of materials and distinguish between the enantiomers, thus finding an application in chiral spectroscopy [19]. Moreover, the vortex waves have also shown advantages in extracting information (shape, thickness, and temperature) from physical objects, that can not be easily achieved using conventional approaches [20]. Furthermore, it is demonstrated that a vortex beam reflected from a dielectric surface exhibits a large transverse beam deformation due to the nonspecular transverse effect [21]. Also, a two-dimensional radar target imaging method is successfully developed by the usage of OAM waves in purpose to capture the azimuth information. This is done with the use of the fast Fourier Transform (FFT) and the back-projection method. It may be beneficial to enhance the capability and the resolution of the monostatic radar target detection and localization hence extracting more information concerning the objects and the materials. This can also be referred to as MIMO radar which increases the sensitivity towards the objects and the surfaces [22, 23]. After that, the rotational Doppler shift of OAM waves within the white light (broadband characterization) launches a new application for remote sensing and rotating object detection, where the rotational Doppler effect is achromatic, i.e. all spectral components are displaced at the same frequency [24]. Furthermore, with longitudinal and transverse waves aligned with angular momentum (spin and orbital) and with several polarizations in the optical domain, some new techniques facilitating the materials characterization field may be provided [25]. All of the above-mentioned achievements in the optical measurement scenarios stand behind the motivation for the wider investigation and study of surface and sub-surface materials (MIMO reflectometry and material characterization) in the THz-regime by using vortex waves. The reason for this is that the vortex waves offer two new additional degrees of freedom. The first one is the increased sensitivity due to the several OAM mode orders with complex phase distribution in the beam. This helps to extract many features and properties from the materials (sub- and surface) such as the permittivity. In addition, the combination of MIMO techniques with vortex waves, can improve the resolution of (sub- and surface) identification. Whereas the second degree of freedom is the increased spectral efficiency, which enables streaming with high data volumes. This work has been carried out with the framework of project S03[1], which is a part of MARIE (Mobile Material Characterization - a

[1]This work is funded by the Deutsche Forschungsgemeinschaft (DFG, German Research Foundation) – Project-ID 287022738 – TRR 196 MARIE in the framework of project S03.

special research project). Nevertheless, due to the necessity of an accurate phase shift for several antennas in the measurement, which is provided by the Butler matrix, the operating frequency is scaled down to $10\,\mathrm{GHz}$ to be the first step towards THz-range. However, many obstacles stand in front of our efforts, such as the distorted reflected beam from the target, the high cost and the complexity of the OAM setup which requires many antennas, cables and Butler matrices. Also, the increased divergence of the vortex beams especially at higher OAM mode orders (solved in chapter 5) and the radiation of each mode in a different direction (solved in [26]) are considered extra challenges. Not to mention, the misalignment between the OAM transmitter and receiver (bistatic setup) are one of the major impacts that also requires extensive efforts to obtain a narrow OAM pencil beam (solved in chapter 4). Some of these challenges have been investigated and solved in this work to facilitate the researches regarding this topic in the future.

1.2 Organization of the Thesis

This thesis is organized in seven chapters, including the chapter of the introduction.

- **Chapter 2: Theory and Fundamentals**

  This chapter discusses the theory and the fundamentals of several approaches operated in this work. Starting with the electromagnetic waves, which are the basics of electrical engineering, followed by the fundamentals of the antenna and the antenna array where the scattering parameters are one of the evaluation methods. Then, the lens and the reflector are handled enabling the enhancement of the antenna gain. After that the dielectric resonator is explained, which radiates once it is illuminated by antennas. Finally, the properties and the approaches to generate the vortex waves are presented.

- **Chapter 3: Vortex Waves Generation**

  In this chapter, the conventional UCA approach and the elliptical antenna approach are compared with a new approach based on crossed 2λ-dipole antennas (CDA) for the emission of vortex waves. Initially, the simulated and measured reflection coefficient S_{11} of a rectangular patch antenna are analyzed in the frequency domain besides the two and three dimensional simulated radiation patterns. Next, to generate vortex waves, the patch antenna is extended to create a uniform circular antenna array whose separation distance d_0 between each pair of adjacent antenna elements is variable to be studied. Moreover, the simulated three dimensional radiation pattern and the helical phase front are illustrated

to emphasize the emitting of the vortex waves by the UCA approach. After that, the two eigenmodes of the elliptical patch antenna, the three dimensional radiation pattern and the helical phase front are presented. Subsequently, the simulated realized and non-realized gain, the simulated reflection coefficient S_{11} and the current distribution of a dipole antenna with several lengths ($\lambda/2$, λ, $3\lambda/2$, and 2λ) are depicted where the dipole antenna with the length of 2λ can contribute to the generation of vortex waves. Therefore, two and four crossed 2λ-dipole antennas including and excluding reflector are presented and discussed. Finally, the comparison between the three approaches is concluded in a summary.

- **Chapter 4: Vortex Beam Steering**

  This chapter proposes the OAM beam steering through the UCA method with and without subarrays. Primarily, the first section discusses the beam steering of the UCA with 8 antenna elements with a separation d_0 between the adjacent antennas of $\lambda/2$, where the simulated two dimensional radiation pattern for many steerable angles are depicted. Besides, the simulated three dimensional radiation pattern and the helical phase front of the steered angle ($\vartheta = -20°$) and the non-steered OAM beam ($\vartheta = 0°$) are illustrated to demonstrate the preserve of the doughnut shaped radiation pattern and the helicity. Later on, the second section introduces the beam steering method with different subarrays (linear, circular, and rectangular) compared to a UCA of 4 antenna elements but with a separation d_0 of $3\lambda/2$. Therefore, the simulated two dimensional radiation pattern of the four scenarios are displayed. Furthermore, the simulated three dimensional radiation pattern and the helical phase front of the case with rectangular subarray are displayed for the steered angle ($\vartheta = -20°$) and for the non-steered one ($\vartheta = 0°$). Finally, the last section concludes this chapter.

- **Chapter 5: Vortex Beam Divergence Reduction**

  With the aid of a tailored lens and a tailored reflector, the OAM beam divergence reduction is the major topic of this chapter. In Section I, a tailored lens is evaluated and compared to the cases of with and without conventional one. Therefore, a simulated and measured wave and phase front are presented alongside the simulated and measured two and three dimensional radiation patter. After that, a similar procedure is applied in Section II with the tailored reflector, however it is assigned only once with OAM impressed field source and once with realistic UCA antennas. The evaluation of the three cases is depicted with the simulated and measured wave and phase front as well as with the simulated and measured

two and three dimensional radiation patter. Finally, Section III compares and discusses the two different approaches.

- **Chapter 6: Mode Order Conversion and Clutter Rejection with OAM**

  In this chapter, a new application of vortex waves with a dielectric resonator is presented. The first section deals with a cylindrical dielectric resonator, where the simulated and measured transmission coefficient S_{21} are depicted. Then, Section II introduces the OAM mode order conversion from an incoming OAM mode order m_{in} to an outgoing OAM mode order m_{out} by means of helically arranged dielectric resonator array, where the simulated two dimensional radiation pattern and the phase front are illustrated. In Section III, the number of RFID codes is increased if helically arranged dielectric resonator arrays are applied. Further, the simulated two dimensional radiation pattern and the phase front highlight this new concept. Followed by Section IV, an experimental verification shows the change of OAM mode order from mode 0 to mode 1, where the simulated and measured transmission coefficient S_{21} emphasize the rejection of the clutter that comes from a metal sheet. Finally, Section V is presented as a summary of this chapter.

- **Chapter 7: Conclusion and Outlook**

  This chapter summarizes the achievements and the favorable results of this work. Also, some recommendations and future works are proposed.

Chapter 2

Theory and Fundamentals

This chapter is intended to simplify the conception of this work. Therefore, the basics of the electromagnetic waves, antennas, antenna array, lens, reflector, dielectric resonator, and vortex waves are discussed.

2.1 Electromagnetic Waves

Besides the gravity, the weak nuclear force, and the strong nuclear force, electromagnetism is one of the four major fundamental forces which have been discovered by the physicists in the last centuries. All of these forces are considered interactions between particles and fields. In purpose to understand the behavior of electric and magnetic fields, the four Maxwell's equations [1, 27] which contain the Ampere's law, the Faraday's law, and the two Gauss's laws, form the basis of the classical electromagnetism. It is a relationship between the electric field $\vec{E}$, the magnetic field $\vec{H}$, the current density $\vec{J}$, and the charge density ρ. In 1785, Charles Augustin de Coulomb discovered the connection between the electric field $\vec{E}$ and the charge (stationary) [28]. Coulomb's law is the name of this discovery, where it is considered the starting point in the theory of electromagnetism. This study had been carried out without the consideration of the current density $\vec{J}$ and the magnetic field $\vec{H}$. Then, Hans Christian Oersted has experimentally verified in 1819 that a constant current density $\vec{J}$ flowing in a wire can generate a magnetic field rotated around this wire (Ampere's law) (2.1). This was the first relation between electricity and magnetism [28]. After that, in 1831 Michael Faraday proved that time-varying magnetic fields $\vec{H}$ can produce electric field in an electric circuit. This new proof was called the Faraday's law or the electromagnetic induction (2.2). Faraday also believed

in the duality between the electric and magnetic fields, where a time varying electric fields is also capable of generating a magnetic field. This theory had been without any proof until the coming of James Maxwell in 1864 [28]. He proved that Faraday's hypothesis is correct and that the Ampere's law is not completed and has to be modified in which a time-varying electric flux density $\vec{D}$, known also as displacement current, can also generate current density $\vec{J}$ (2.1) [28]. Therefore, the Ampere's law emphasizes that the magnetic field $\vec{H}$ is related to both of the current density $\vec{J}$ and to the displacement current $\frac{\partial \vec{E}}{\partial t}$ and vice-versa (2.1). While, the Faraday's law revealed that time-varying magnetic fields can produce electric field and vice-versa (2.2). This law shows that the electric and magnetic field are coupled with each other and that the electromagnetic waves can propagate. Moreover, the Gauss's law of the mathematician Carl Friedrich Gauss was used to form the third and the fourth Maxwell's equations in which Gauss's law relates the charges with the field. In the case of electricity, the divergence of the electric flux is proportional to the charge density across a closed surface (2.3), while the Gauss's law for magnetism states that due to the unavailability of magnetic monopoles, the divergence of a magnetic flux cross a close surface is equal to zero (2.4).

$$\nabla \times \vec{H} = \vec{J} + \frac{\partial \vec{D}}{\partial t} \tag{2.1}$$

$$\nabla \times \vec{E} = -\frac{\partial \vec{B}}{\partial t} \tag{2.2}$$

$$\nabla \cdot \vec{D} = \rho \tag{2.3}$$

$$\nabla \cdot \vec{B} = 0 \tag{2.4}$$

These equations can be also written in integral form.

$$\oint_{\partial A} \vec{H} \cdot d\vec{s} = \iint_{A} \vec{J} \cdot \vec{n} dA + \frac{d}{dt} \iint_{A} \vec{D} \cdot \vec{n} dA \tag{2.5}$$

$$\oint_{\partial A} \vec{E} \cdot d\vec{s} = -\frac{d}{dt} \iint_{A} \vec{B} \cdot \vec{n} dA \tag{2.6}$$

$$\oint_{\partial V} \vec{D} \cdot \vec{n} dA = \iiint_{V} \varrho \, dV \tag{2.7}$$

$$\oint_{\partial V} \vec{B} \cdot \vec{n} dA = 0 \tag{2.8}$$

Moreover, the electric and magnetic flux densities $\vec{D}$ and $\vec{B}$ are related to the electric and magnetic fields $\vec{E}$ and $\vec{H}$ by the permittivity ε and the permeability μ of the material, respectively.

$$\vec{D} = \epsilon \vec{E} \tag{2.9}$$

$$\vec{B} = \mu \vec{H} \tag{2.10}$$

Furthermore, due to the continuity equation the charge density ρ and the current density $\vec{J}$ are connected to each other.

$$\nabla \cdot \vec{J} = -j\omega\rho \tag{2.11}$$

2.2 Fundamentals of Antennas

Understanding Maxwell's equation deeper, Heinrich Rudolph Hertz built the first wireless electromagnetic system in 1886. He has validated the theory of electromagnetic waves experimentally. In his laboratory, he succeeded to produce electromagnetic waves generated by a transmitting $\lambda/2$ dipole and to detect these waves by a loop over a short distance [1, 29]. After that, in 1901 Guglielmo Marconi achieved to transmit radio signals over a long distance through the use of monopole antennas declaring the first application of electromagnetic waves [1]. The antennas are one of the crucial components which are responsible for several applications in the radio- and microwave domain. Antennas enable mainly the transmission and reception of electromagnetic waves, and it can also be defined as a transition between the EM guide device (coaxial cables, hollow waveguide) and free space. The antennas can be classified into many categories such as planar antennas [30], loop antennas [31], broadband antennas [32], reflector antennas [33], linear antennas [34], and aperture antennas [35] (cf. Fig 2.1). The reason for these multiple categories of antenna belongs to the presence of several parameters and characteristics which

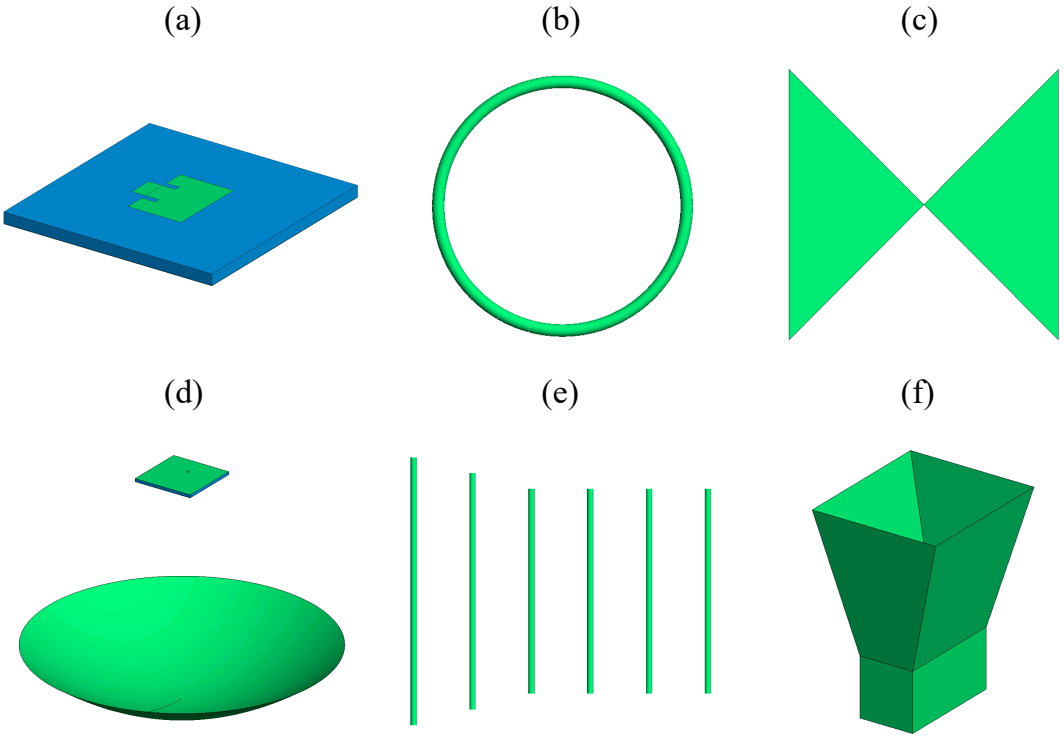

Figure 2.1: Illustration of the antenna types such as planar antenna (patch) (a), loop antenna (b), broadband antenna (Bowtie) (c), reflector antenna (d), linear antenna (Yagi-Uda) (e), and aperture antenna (Horn) (f).

affects positively and negatively on the applications [1].

The most important antenna's parameters are presented in the following:

- **Directivity**: The directivity (D) (2.13) is the ratio of the maximum radiated power density (S_{max}) over the power density (S_i) of an isotopic radiator without taking into account the losses (conduction and dielectric). Also, the reflected energy at the feeding point is neglected in which the power density (S_i) of an isotopic radiator is the ratio of the radiated power (P) over the area of a sphere (2.12). The unit of the directivity is (dBi) (2.14) [36].

$$S_i = \frac{P}{4\pi r^2} \tag{2.12}$$

$$D = \frac{S_{max}}{S_i} \tag{2.13}$$

$$D[dBi] = 10\log_{10}(D) \tag{2.14}$$

- **Antenna Efficiency (η)**: The antenna's efficiency η is represented by the radiated power (P_s) and an individual antenna's emitted power (P_{in}) (2.15) [36]. In other words, the conductive and the ohmic losses in addition to the energy reflection at the feeding point are here considered to be the cause of a decline in directivity. The antenna efficiency can reach maximum 1.

$$\eta = \frac{P_s}{P_{in}} \tag{2.15}$$

- **Gain (G)**: The gain (2.16) is the same as directivity but with taking into consideration the losses [36]. It can also be described by the following equation.

$$G = \eta D \tag{2.16}$$

A directional beam of an antenna array has generally one main lobe, which has one gain maximum located in the optical axis. Whereas, the ideal OAM beam has theoretically a doughnut-shaped OAM radiation pattern characterized by an occurring zero in the optical axis and by a distributed radiation maximum, which extends along a circular line. This is probably not the way it precisely works for realistic potentially distorted OAM beams, where the circular line may become a deformed closed contour containing several relative extrema and the maximum gain. This maximum gain rarely lies in the E- respective H-plane and is therefore barely represented these crossectional images leading to a pragmatic definition for the antenna gain in the context of emitted doughnut-shaped OAM beams. Therefore, the maximum gain can be determined in one of these two crossectional images (E- or H-plane), where two apparent lobe-like curves appear. However, the gain deviations between the selected maximum gain and the missed real maximum gain is not supposed to be very large. In the following and for simplicity reasons only the crossectional data of the OAM radiation pattern in the H-plane has been taken into account to identify the gain of the underlying OAM antenna. Please note that these two apparent lobe-like curves are not similar the conventional side lobes.

- **Bandwidth**: The bandwidth of an antenna is a frequency band in which the antenna performs well [1]. In practice, the reflection coefficient S_{11} shall be less than e.g. $-10\,\mathrm{dB}$.

- **Polarization**: The polarization of an electromagnetic wave describes the orientation of the oscillating electric field represented by the direction of the dominant transversal electric

field component [29]. The most two popular polarizations are linear and circular. The electric field oscillates linearly, whereas the electric field continuously oscillates in a circular form in the case of circular polarization.

- **Half Power Beamwidth (HPBW)** :

  The antennas have many beams which the wide one (the main lobe), plays the most important role. The angular width of this lobe, at which the signal power is half the value of the peak, is called half-power beamwidth (HPBW) (cf. Fig 2.2) [1].

- **Side lobe Level (SLL)**: Besides the main lobe, there are some undesirable lobes well known as the side lobes (cf. Fig 2.2). These side lobes have to be suppressed in order to decrease the undesirable radiated waves [1]. The level between the main and these lobes is called the side lobe level (SLL), which has to be higher than $10\,\mathrm{dB}$.

- **Antenna effective area**: In addition to all these antenna parameters, the antenna effective area (A_e) is also crucial in which it measures how effective is an antenna by capturing the electromagnetic waves. It depends on the power density of the incident waves (W_i) and the power delivered to the load (P_T) [1].

$$A_e = \frac{P_T}{W_i}, \tag{2.17}$$

  It can also be described with the wavelength and the Gain [1].

$$A_e = \frac{\lambda^2 G}{4\pi}, \tag{2.18}$$

2.3 Phased Antenna Array

In the previous section, the mentioned antenna's parameters were subjected only to one single antenna element. Generally, the radiation pattern of one single antenna is wide and unable to provide very high directivity. Therefore, the enhancement of the antenna elements number in some special geometrical configurations helps in increasing the directivity as well in reducing the beam divergence. These configurations are known as arrays where mostly identical antenna elements are applied to form some specific arrangements such as linear, circular, and rectangular ones. The radiated fields of each individual antenna interfere constructively in the desired

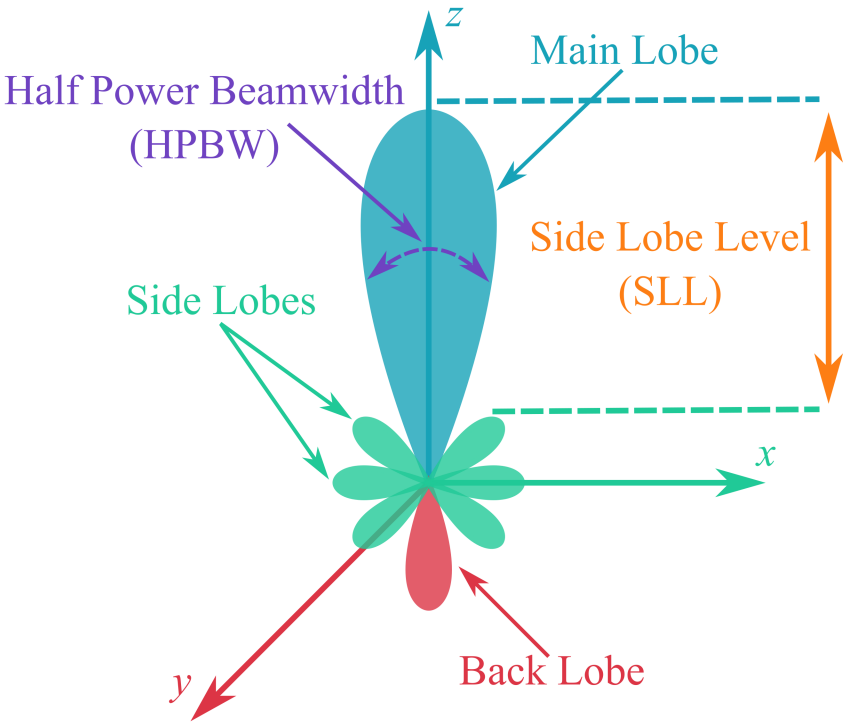

Figure 2.2: Illustration of antenna parameters.

directions however destructively with the other directions. Hence, the maximum gain of the array is larger than the field of an individual antenna. This conclusion depends on many factors, such as the separation between the antenna elements, the excitation's amplitude and phase, and on the geometrical configuration [1]. In the case of N-antenna elements, the total field is equal to the sum of all these fields. In other words, the total field E_{total1} (2.19) is identical to the field of one antenna element E_{ant} multiplied by the array factor AF. Each configuration has its array factor.

$$E_{total} = E_{ant} \cdot AF, \tag{2.19}$$

For the circular array, where the antenna elements are distributed in a circular ring, the total E-Field is described with the next equation

$$E_{total}(r, \vartheta, \varphi) = \frac{e^{-jkr}}{r} \cdot AF(\vartheta, \varphi), \tag{2.20}$$

where r is the separating distance between the center of the array and the observation point, and k is the wave vector. The array factor of a circular array with uniform amplitude excitation is determined using the following equation [1]

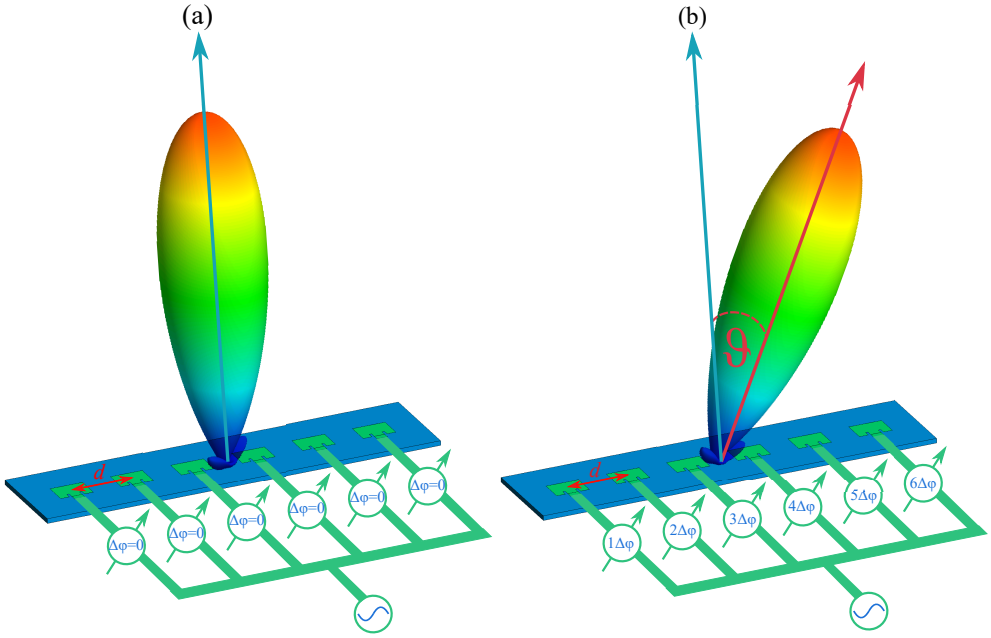

Figure 2.3: Illustration of the phased antenna array without steering (a), and with steering (b).

$$AF(\vartheta, \varphi) = NI_0 \sum_{n=-\infty}^{+\infty} J_{mN}(k\rho_0) e^{jmN(\pi/2-\xi)}, \tag{2.21}$$

where N is the number of the antenna elements, I_0 is a uniform amplitude excitation, $J_{mN}(k\rho_0)$ is the Bessel function, and ξ is a function specified as

$$\xi = \arctan\left(\frac{\sin\vartheta\sin\varphi - \sin\vartheta_0\sin\varphi_0}{\sin\vartheta\cos\varphi - \sin\vartheta_0\cos\varphi_0}\right). \tag{2.22}$$

Besides the improvement of the gain, the antenna array can also offer much desirable properties such as modifying the shape of the radiation pattern by changing the distance between the antenna elements, suppressing the side lobe level by using non-uniform amplitude distribution such as Binomial [37], and Dolph-Tschebyscheff [38], and beam steering by manipulating the phase excitation [36] of each antenna element. In this case, this array can be called a phased array [39]. The required phase shift φ (2.23) between each antenna element is defined as

$$\varphi = \frac{2\pi \cdot d \cdot \sin\vartheta}{\lambda}, \tag{2.23}$$

where d is the separation distance between each pair of adjacent antenna, ϑ is the desirable steering angle, and λ is the wavelength in free space. Fig. 2.3 illustrates the phased array of a linear configuration.

2.4 Scattering Parameters

In the domain of radio and microwave frequencies, the inputs and the outputs of electrical networks are not defined by voltage and current, since it is difficult to define voltages and currents for non-TEM modes [29], but by wave amplitudes whose amplitude and phase can be measured. In a network with N ports, the incoming signal (wave amplitude) at port y is dispersed in such a way that a part is reflected at the input and the rest of the signal is transmitted to the other ports, under the condition that all ports are set to zero [40], i.e. these ports are terminated with matched loads in order to avoid reflections and therefore false measurements. Thus, S_{xx} is the reflection coefficient, and S_{xy} is the transmission coefficient from port y to port x (2.24). Fig. 2.4 illustrates the scattering parameters (S-parameter) of an electrical network of two ports. The number of S parameters depends on the quantity of ports in the network. In the case of the two ports, there are 4 S-parameters (2.25) A vector network analyzer can directly contribute to the measurement of the scattering parameters.

$$S_{yx} = \frac{b_y}{a_x}|_{a_y=0} \tag{2.24}$$

$$\begin{aligned} b_1 &= S_{11}a_1 + S_{12}a_2 \\ b_2 &= S_{21}a_1 + S_{22}a_2 \end{aligned} \tag{2.25}$$

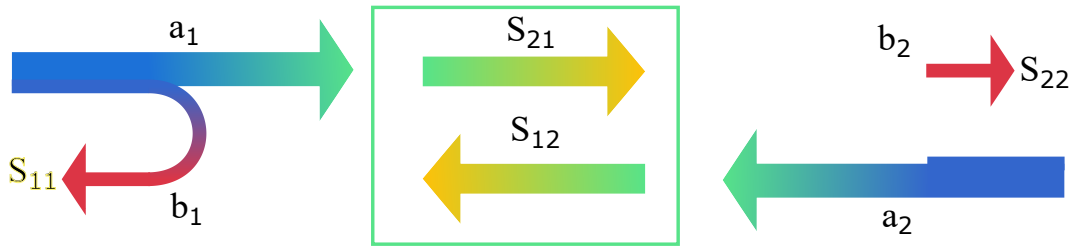

Figure 2.4: Illustration of the scattering parameters of two ports.

2.5 Lens

As mentioned in section 2.3, the antenna array has the feature of reducing the beam divergence. Unfortunately, it makes the whole system sophisticated that it requires more new equipment

such as cables, power dividers, etc. However, other approaches other than the antenna array can reduce the beam divergence like using lenses. The primary purpose of using lenses is to collimate the emitted waves coming from an antenna towards the lens to be focussed in one direction. The spherical waves are transformed into waves with uniform phase front, thus reducing the divergence and enhancing the gain in order to transmit and receive signals over long distances. The radiated electromagnetic waves can also be conceptualized and simplified as rays, whereby each ray coming from the origin have to be refracted at a certain point on the lens aligning parallel rays. In the case of reception, the incident waves are focused on one point. The lens should have a convenient geometrical configuration made of a dielectric material with a specific permittivity ϵ_r, which reduces the speed of waves propagated in the lens (2.26).

$$v = \frac{c_0}{e_r^2} = \frac{c_0}{n} \tag{2.26}$$

A lens is a beneficial tool to counteract the beam divergence once integrated into the antenna. However, it suffers from its heavyweight particularly when lower frequencies are required. There are many kinds of lenses that can be used with antennas in the RF and microwave domain, but the extensively used ones are the elliptical [41] and the Luneburg lens [42]. The elliptical lens is a lens with an elliptical shape where the antenna is mounted directly on the focal point permitting easy integration with the antenna (cf. Fig. 2.5 (b)). The shape function of the elliptical lens is designed according to the Fermat's principle [43], which mentioned that the optical path length of all rays should be identical, as illustrated in Fig. 2.5 (a). This is determined by the next relationship

$$n_1 r_0 + n_2 L = n_1 r(\varphi) + n_2 l, \tag{2.27}$$

where n_1 and n_2 are the refractive indices of two different layers, and r_0 denotes the focal point. Therefore, the shape function of the elliptical lens is described as following

$$r(\varphi) = \left(\frac{r_0(n_1 - n_0)}{n_1 - n_0 \cos(\varphi)} \right), \tag{2.28}$$

where n_1 and n_0 represents the refractive index of the lens and the air, respectively, and r_0 is the height of the lens at $\varphi = 0°$. The shape of the elliptical lens depends on the refractive index n of the material whereby the higher the permittivity is, the smaller the lens is. Further, the size of the elliptical lens can be minimized making it more compact and thinner thus saving some weight

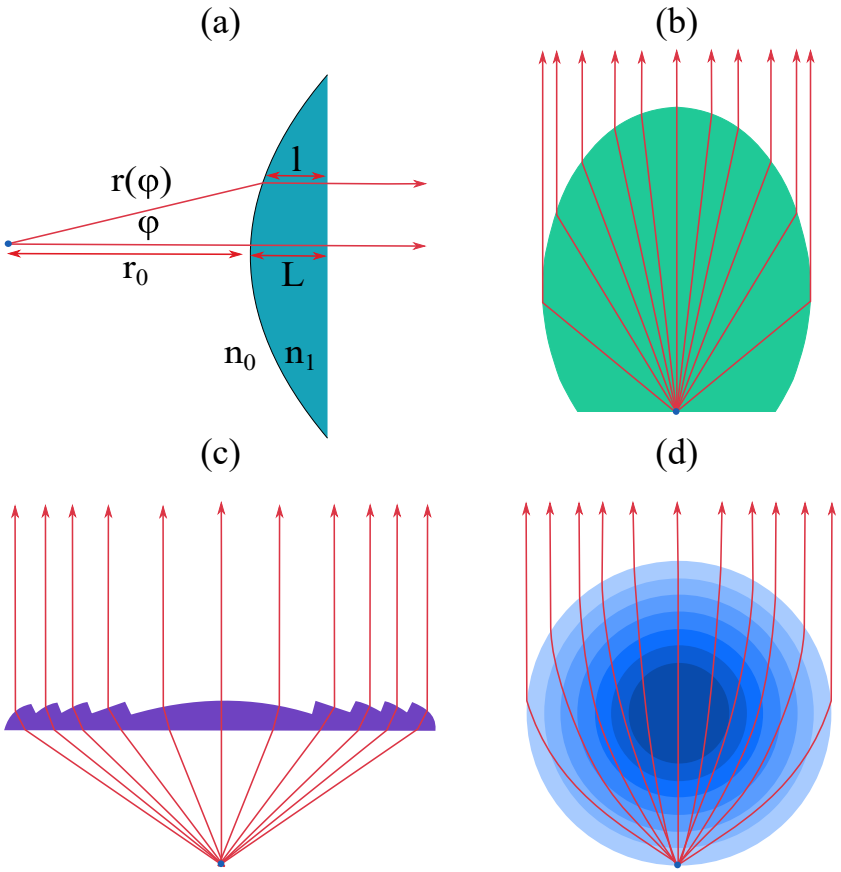

Figure 2.5: Illustration of elliptical lens (a), Fresnel lens (b), and Luneburg lens (c).

and volume. This lens is well known as Fresnel lens [44], as depicted in Fig. 2.5 (c). On the other hand, the Luneburg lens is a spherical gradient-index lens where the permittivity ϵ_r varies in dependency of the radius r (2.29) (cf. Fig. 2.5 (d)).

$$\epsilon_r = 2 - (\frac{r}{R})^2 \tag{2.29}$$

where R is the radius of the lens. The Luneburg lens offers a special feature in which its focal point is almost on its surface allowing the lens to be used from many directions due to its round shape [1, 43].

2.6 Reflector

Similar to the lens, the reflector is capable of reducing the beam divergence and thus increasing the gain for several applications such as deep space communication. The reflector applies the same concept as the lens, but instead of refracting the waves in the lens, it reflects the propagated

waves towards the reflector due to its highly conductive material which permits the reflection of the transmitted field. The reflector can take many geometrical configurations where the most popular shape is the parabolic one [45], also known as paraboloid, which collimates the incident waves from the focal point into one direction, similar to the lenses (cf. Fig. 2.6 (a)). As in the lenses, Fermat's principle allows the shape function of the parabolic reflector to be formed where the following equation describes the relationship

$$r(\varphi) = \left(\frac{2r_0}{n_1(1 + \cos(\varphi))} \right), \tag{2.30}$$

where r_0 is the height of the reflector at $\varphi = 0°$. The issue concerning the heavyweight of the lens can be solved by the aid of the reflector. Nevertheless, it is hard to align the antenna with the reflector. Moreover, the location of the antenna in the focal point and the long feeding cable happens to be another issue that can disturb the reflected waves and cause some deformation in the beam. Therefore, some methods can be the solution of this problem such as offset-fed [46], Cassegrain [47] and Gregorian parabolic reflector [48]. The offset-fed parabolic reflector is a part of the parabolic reflector (front-feed parabolic reflector), where the antenna is not suspended in front of the reflector like the parabolic antenna, as depicted in Fig. 2.6 (b). In other words, the focal point is not in the path of the waves, so the distortion of the reflected waves caused by the antennas is avoided. The other approaches are the Cassegrain and the Gregorian parabolic reflector (cf. Fig. 2.6 (c, and d)), where rather than using only one reflector, two reflectors (primary and secondary) are correlated. The antenna is located in the middle of the primary reflector, where the secondary reflector is a small convex reflector for the case of Cassegrain, whereas it is a concave one in the case of Gregorian [1].

2.7 Dielectric Resonator

Not only can the antennas emit electromagnetic waves, but so does the dielectric resonators which behave similar to the rectangular or cylindrical cavity resonator. The dielectric resonator (DR) is composed of a dielectrical material (nonconductive) with very low losses and a high permittivity ϵ_r. The dielectric resonators are generally small, cost-effective and lightweight offering some applications in the microwave and millimeter domain. A dielectric resonator reacts and resonates once illuminated by incident plane waves. Hence, the displacement current generated inside the DR can radiate one of the four supported modes (Transverse Electric (TE), Transverse Magnetic

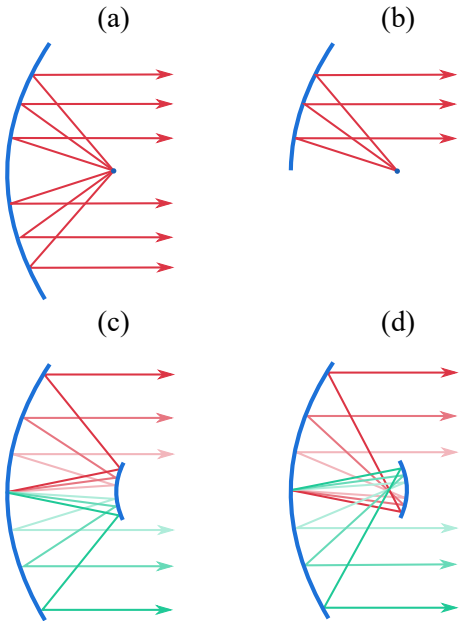

Figure 2.6: Illustration of parabolic reflector (a), offset-fed parabolic reflector (b), Cassegrain parabolic reflector (c), and Gregorian reflector (d).

(TM) and Hybrid Modes (HE and EH)), whose eigen frequency and corresponding quality factor Q depend mainly on the relative permittivity ε_r, the size, the loss tangent ($\tan\delta$), and the orientation of the DR [29]. Further, the DR also can be used in the microwave circuits as oscillators or filters [49]. The dimensionless quality factor Q evaluates the DR by indicating the amount of the stored energy inside the dielectric resonator. It can be determined with two different definitions

$$Q = 2\pi \times \frac{Energy\ Stored}{Energy\ Dissipated\ per\ cycle}, \tag{2.31}$$

$$Q = \frac{f_0}{\Delta f}, \tag{2.32}$$

where f_0 is the resonant frequency and Δf is the bandwidth in which the power is $3\,\mathrm{dB}$ lower than the maximum one. The greatest dissipation in the dielectric resonators is dielectric and radiative since the conductive one is unavailable. A DR with a lower quality factor is required for the intention of high radiation. The radiation process occurs as a result of the fringing or leakage from the sides of the dielectric resonator [29]. Various configurations are already available on the market, and one of the most common and used ones is the cylindrical resonator. The fourth modes can be classified as follows:

- **(Transverse electric $\mathbf{TE_{mnp}}$ (H-mode))**: The z-component of the E-field is unavailable ($E_z = 0$).
- **(Transverse magnetic $\mathbf{TM_{mnp}}$ (E-mode))**: The z-component of the H-field is unavailable ($H_z = 0$).
- **(Hybrid mode ($\mathbf{HE_{mnp}}$ and $\mathbf{EH_{mnp}}$)**: The E-field is more dominant in the case of $\mathrm{HE_{mnp}}$ with the presence of E_z, while the H-field is more dominant in the case of $\mathrm{EH_{mnp}}$ with the presence of H_z.

where m, n, and p are indices that denote a integer multiple of half the wavelength at the resonant frequency in the x, y, and z directions concerning the cartesian coordinate system. Whereas regarding the cylindrical coordinate system, the number of wavelengths is induced in the azimuthal, radial and axial directions. The fields are neither TE nor TM mode and have no azimuthal variations for $m = 0$. Whereas, the fields are HEM for $m > 0$ and have two parts in the z-direction (TE and TM part). The E_z component can be described with the following equations for the four different modes

$$\begin{aligned} TM_{0np}, HE_{mnp} : E_z &= AJ_m(k_1\rho) \begin{bmatrix} \cos(m\phi) \\ \sin(m\phi) \end{bmatrix} \quad \begin{Bmatrix} \cos(\beta z) \\ \sin(\beta z) \end{Bmatrix} \\ TE_{0np}, EH_{mnp} : H_z &= AJ_m(k_1\rho) \begin{bmatrix} \cos(m\phi) \\ \sin(m\phi) \end{bmatrix} \quad \begin{Bmatrix} \cos(\beta z) \\ \sin(\beta z) \end{Bmatrix} \end{aligned} \tag{2.33}$$

where A is a constant, and J_m is the Bessel function of the first type with the order m

$$J_m(x) = \sum_{k=1}^{+\infty} \frac{(-1)^k (x/2)^{m+2k}}{k!(m+k)!} \tag{2.34}$$

In Fig.2.7, the simulated Radar Cross Section (RCS) [$\mathrm{dBm^2}$] of the cylindrical dielectric resonator is presented. The RCS is a characterization of a target, i.e. it is a ratio between the scattered power of the target P_s to the incident power density P_i (2.35), where R is the distance between the radar and the target.

$$\sigma = 4\pi R^2 \frac{P_s}{P_i} \tag{2.35}$$

The DR is illuminated from three different directions $\vartheta = 0°$, $\vartheta = 45°$, and $\vartheta = 90°$, where four modes occur, namely HE_{11} at 10.1 GHz, EH_{11} at 10.8 GHz, TM_{01} at 12.1 GHz, and HE_{21} at 12.5 GHz, as shown in Fig.2.8. In Figs. 2.9, 2.10, 2.11, 2.12, the field distribution of the electric and magnetic fields for the four modes are illustrated.

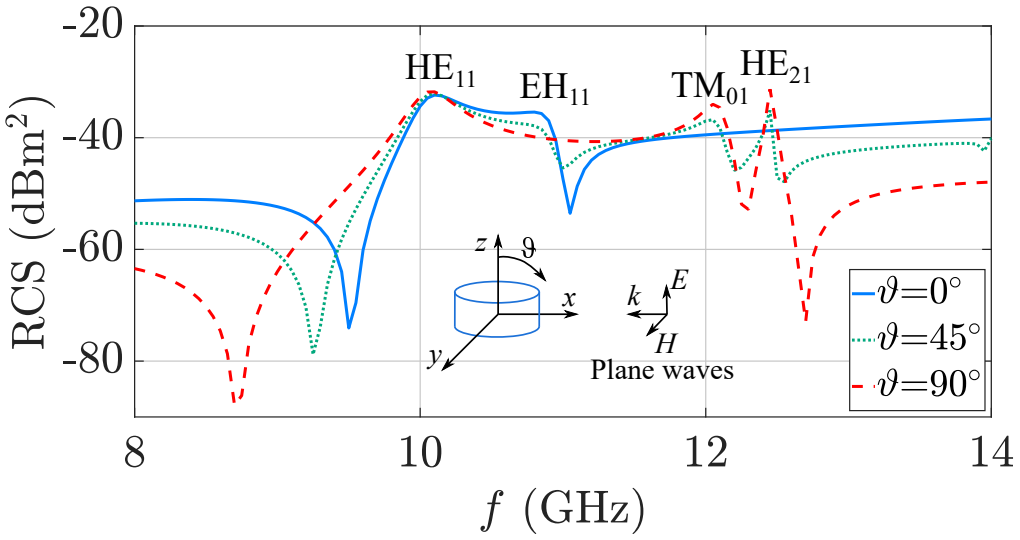

Figure 2.7: Simulated Radar Cross Section (RCS) dBm^2 of the cylindrical DR when it is illuminated by planes waves from three different direction $\vartheta = 0°$, $\vartheta = 45°$, and $\vartheta = 90°$

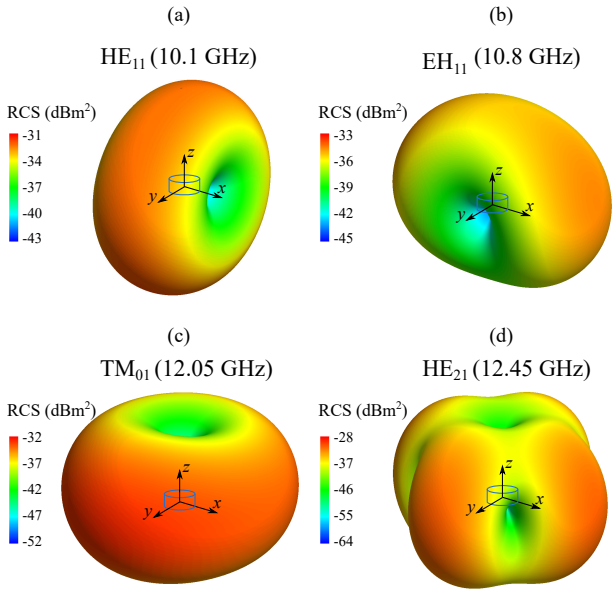

Figure 2.8: Simulated radiation pattern of the resonant modes of the DR when it is illuminated by planes waves with the mode HE_{11} at 10.1 GHz, EH_{11} at 10.8 GHz, TM_{01} at 12.1 GHz, and HE_{21} at 12.5 GHz.

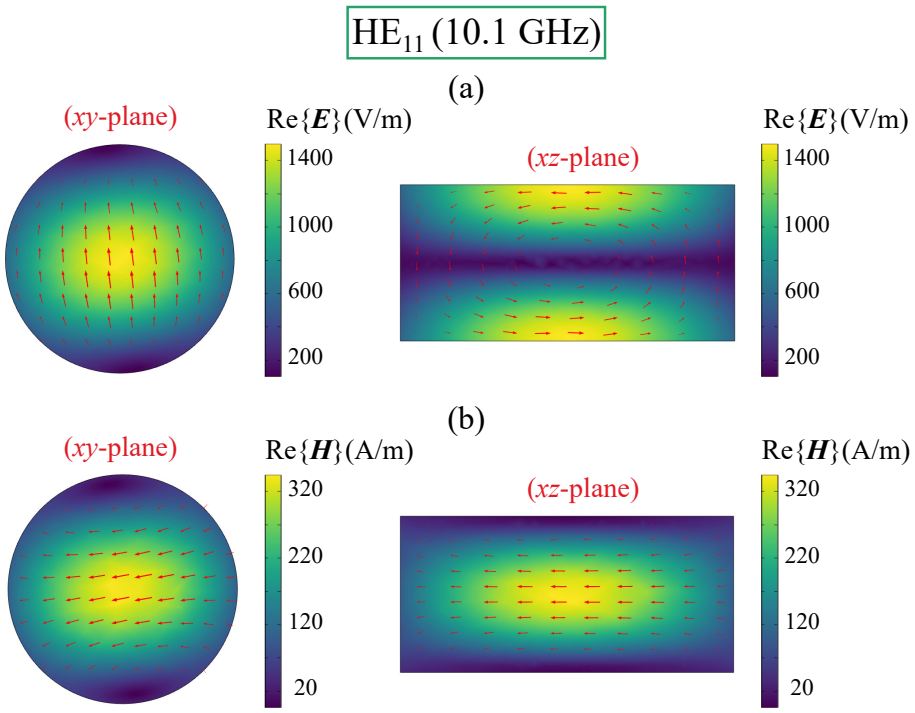

Figure 2.9: Field distribution of the mode HE_{11} at $10.1\,\mathrm{GHz}$ of the electric field in xy-plane at $z = 3$ mm and in xz-plane at $y = 0$ (a), and of the magnetic field in xy-plane at $z = 1.5$ mm and in xz-plane at $y = 0$ (b).

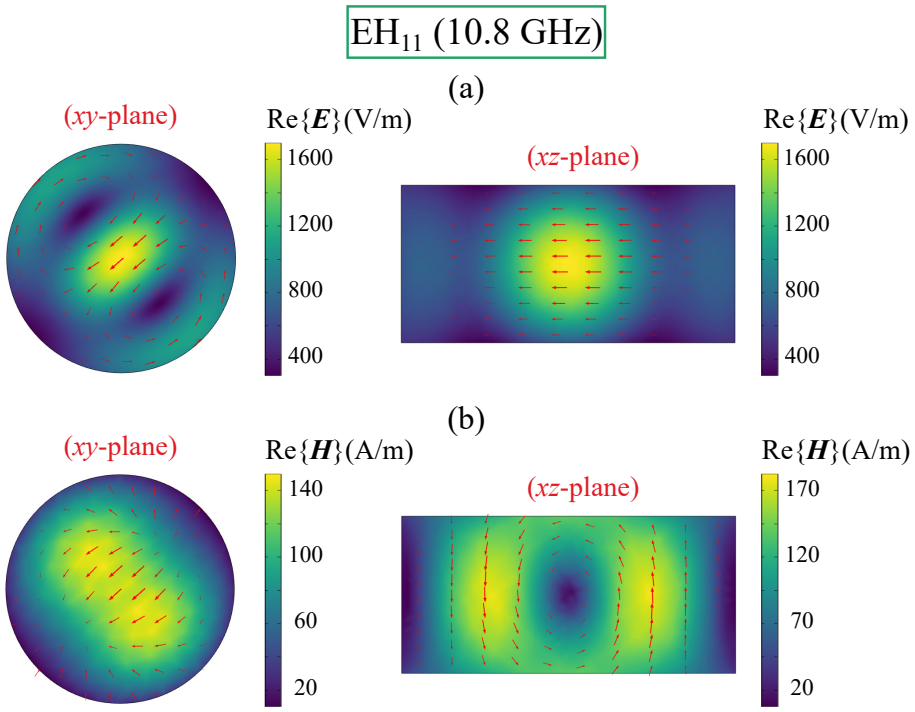

Figure 2.10: Field distribution of the mode EH_{11} at $10.8\,\mathrm{GHz}$ of the electric field in xy-plane at $z = 1.5$ mm and in xz-plane at $y = 0$ (a), and of the magnetic field in xy-plane at $z = 3$ mm and in xz-plane at $y = 0$ (b).

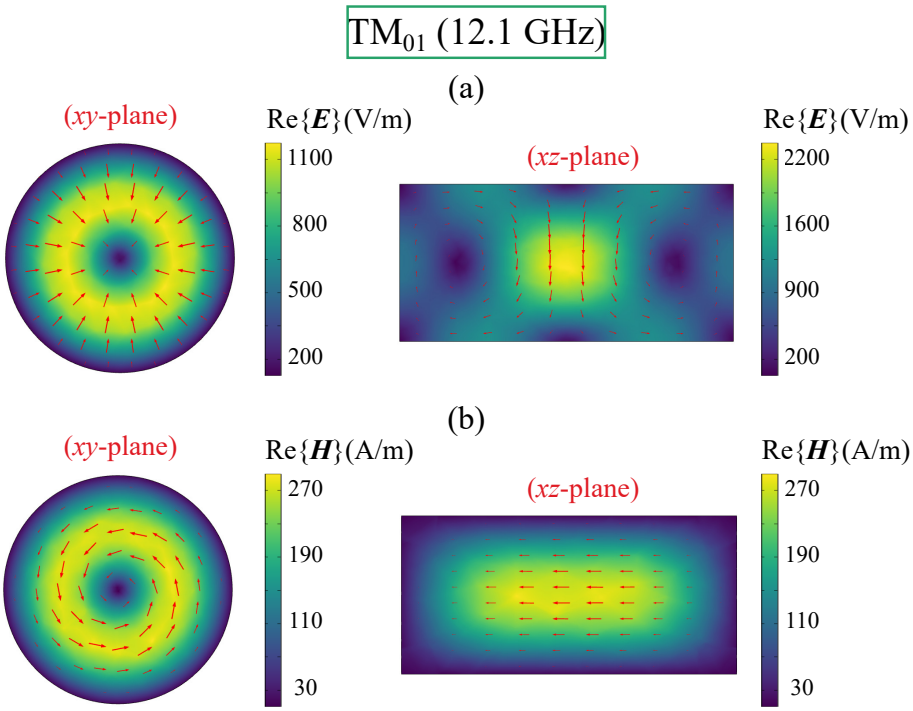

Figure 2.11: Field distribution of the mode TM_{01} at 12.1 GHz of the electric field in xy-plane at $z = 3$ mm and in xz-plane at $y = 0$ (a), and of the magnetic field in xy-plane at $z = 1.5$ mm and in xz-plane at $y = 1.5$ (b).

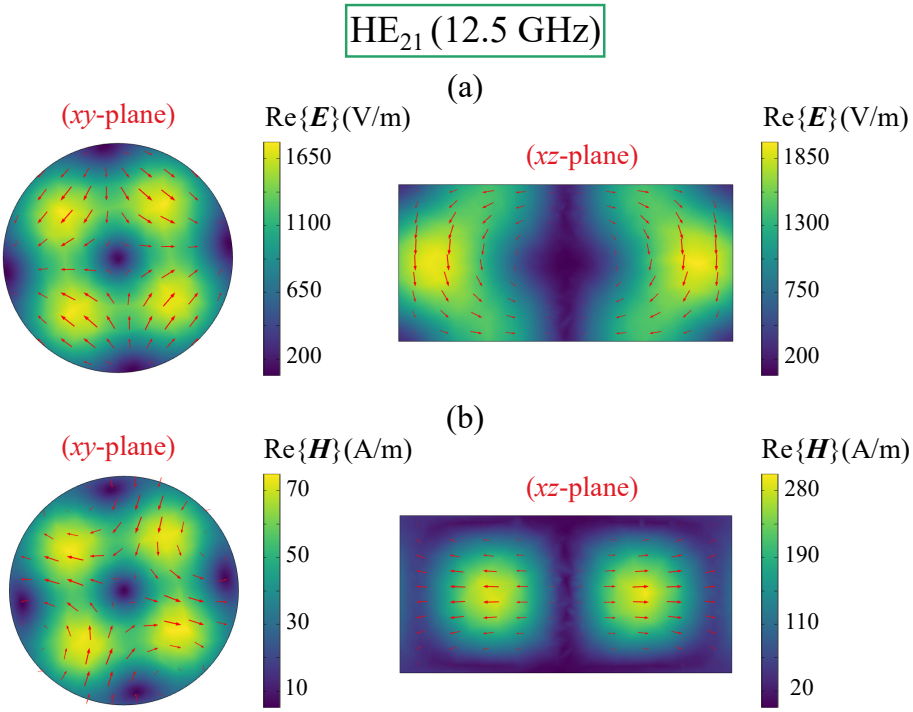

Figure 2.12: Field distribution of the mode HE_{21} at 12.5 GHz of the electric field in xy-plane at $z = 3$ mm and in xz-plane at $y = 0$ (a), and of the magnetic field in xy-plane at $z = 1.5$ mm and in xz-plane at $y = 0$ (b).

2.8 Vortex Waves

The electromagnetic waves (EM) are radiated waves that propagate in a medium carrying simultaneously energy and momentum. The momentum is formulated of linear and angular ones where the angular J (2.36) consists of two parts, namely the spin angular momentum S (SAM) (2.37) and the orbital angular momentum L (OAM) (2.38). The spin angular momentum describes the intrinsic property of the spin with respect to the EM rotational degrees of freedom (intrinsic rotation of the polarization). On the other hand, the orbital angular momentum is an extrinsic property that illustrates the orbital's rotational degrees of freedom (extrinsic rotation) including a helical transverse phase structure of $\exp(-j\varphi m)$. φ is the transverse azimuthal angle, and m is an unbounded integer that indicates the OAM mode order.

$$\vec{J} = \vec{S} + \vec{L} = \int \epsilon_0 \vec{r} \times Re\{\vec{E} \times \vec{B}^*\} dV, \tag{2.36}$$

where

$$\vec{S} = \epsilon_0 \int Re\{\vec{E}^* \times \vec{A}\} dV, \tag{2.37}$$

$$\vec{L} = \epsilon_0 \int Re\{i\vec{E}^* (\hat{\vec{L}} \cdot \vec{A})\} dV, \tag{2.38}$$

where $\hat{\vec{L}} = -i(\vec{r} \times \nabla)$ and $\vec{A}$ is the magnetic vector potential [50]. The OAM beam is also a Laguerre-Gaussian beam ($LG_{p,l}$) but with a $p = 0$ [51]. In the cylindrical coordinate system (ρ, φ, z), the EM waves (TE) propagating in the z-direction can be described with the following equations

$$\boldsymbol{E}_\rho = j \frac{Z_0 \omega m}{k\rho} E_0 J_l(k_\rho \rho) e^{-jk_z z} e^{-jm\varphi} \boldsymbol{e}_\rho, \tag{2.39}$$

$$\boldsymbol{E}_\varphi = -\frac{Z_0 \omega k_\rho}{k} E_0 J_l'(k_\rho \rho) e^{-jk_z z} e^{-jm\varphi} \boldsymbol{e}_\varphi, \tag{2.40}$$

$$\boldsymbol{E}_z = 0, \tag{2.41}$$

$$\boldsymbol{H}_{\rho} = -\frac{\omega k_{\rho} k_z}{k^2} E_0 J_l'(k_{\rho}\rho) e^{-jk_z z} e^{-jm\varphi} \boldsymbol{e}_{\rho}, \tag{2.42}$$

$$\boldsymbol{H}_{\varphi} = j\frac{\omega m k_z}{k^2 \rho} E_0 J_l(k_{\rho}\rho) e^{-jk_z z} e^{-jm\varphi} \boldsymbol{e}_{\varphi}, \tag{2.43}$$

$$\boldsymbol{H}_{z} = -j\frac{k_{\rho}^2}{k^2} J_l(k_{\rho}\rho) e^{-jk_z z} e^{-jm\varphi} \boldsymbol{e}_{z}, \tag{2.44}$$

where Z_0 is the characteristic impedance in free space, ω is the angular frequency, m is the OAM mode order, E_0 is the wave amplitude, $J_l(k_\rho\rho)$ is the l^{th} order Bessel function, k_0 is the free-space wave number

$$k_0^2 = k_{\rho}^2 + k_z^2 = \frac{\omega^2}{c^2}, \tag{2.45}$$

where c is the speed of light [52].

The vortex waves are essentially characterized by a doughnut-shaped radiation pattern where the phase located in the center specifically on the beam axis is indeterminable, thus defining a phase singularity. The helical phase distribution that varies linearly around the beam axis is one of the vortex waves' features. The higher the OAM mode order m, the larger the beam divergence and therefore the lower the gain (cf. 2.2) as depicted in Fig. 2.13 (a, b, c, and d) [53]. Whereas the number of the helices and the OAM mode order m are proportional (cf. Fig. 2.13 (e, f, g, and h)). Using the right-handed thread, when the OAM mode order m appears positive, the rotation of the phase is clockwise, whereas the negative OAM mode order rotates the phase counterclockwise with respect to the propagation direction.

2.9 Generation of Vortex Waves

Up to today, the researchers have developed a lot of approaches to emit vortex waves such as spiral phase plates (SPP) [54–57], holographic diffraction gratings (HP) [58–60], reflective and transmissive metasurfaces [61–63], reflectors [64–66], one specific antenna (radiating two eigenmodes) [67–69], and uniform circular antenna arrays [53, 70, 71]. Among them, the first two approaches arrive from the optical regime, where they have been used very successfully in the transition of multiple OAM mode orders in fiber optics, thereby improving the communication. The dielectric spiral phase plate is a spiral-shaped piece with a constant relative permittivity,

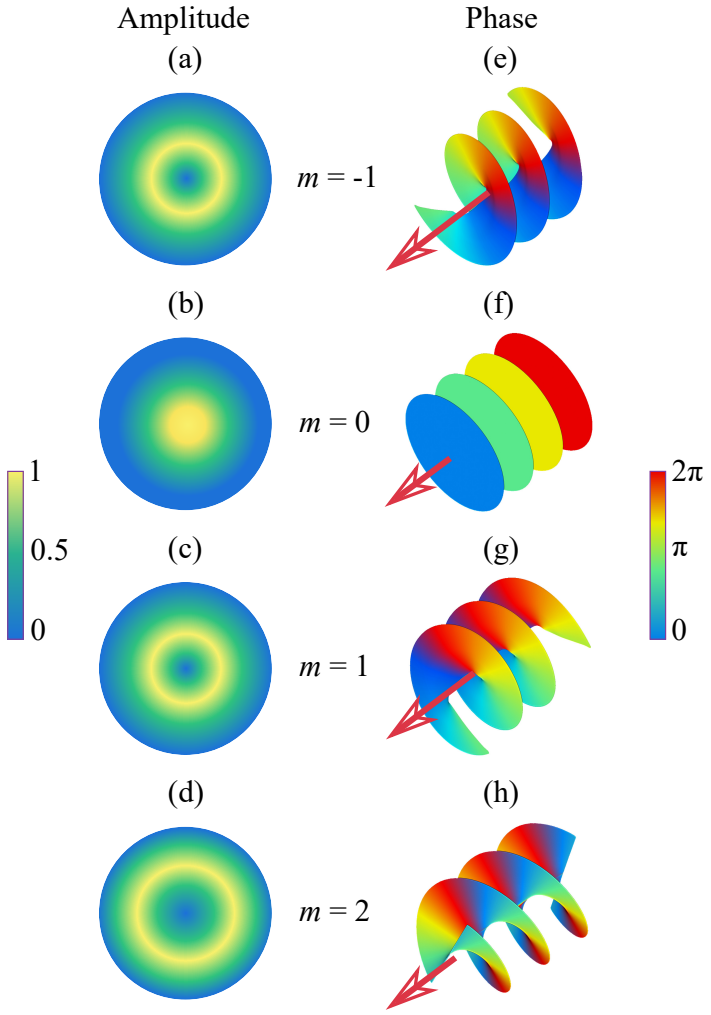

Figure 2.13: The intensity and the phase front of the OAM mode order $m = -1$, $m = 0$, $m = +1$, and $m = +2$.

which responds like a spatial phase modulator in order to convert the plane waves characterized with uniform phase up to vortex waves characterized with helical phase (cf. Fig. 2.14 (a)). The plane waves propagate through the dielectric SPP, where each part of the waves needs a certain period of time to pass through the SPP and thus generating the helical phase front. Whereas, the holographic grating (HP) reacts like a diffractor, which diffracts the incident waves into multiple beams in several directions (cf. Fig. 2.14 (b)). This approach can be beneficial in the multiplexing and de-multiplexing of the OAM states [60]. However, these two approaches besides the metasurfaces and the reflectors need additional antenna to have the possibility to radiate vortex waves, i.e. they are not directly radiating vortex waves from itself. The metasurfaces (MS) are artificial sub-wavelength planar resonator arrays in contrast to the three-dimensional metamaterial (cf. Fig. 2.14 (c)). They have unprecedented capability to control the amplitude,

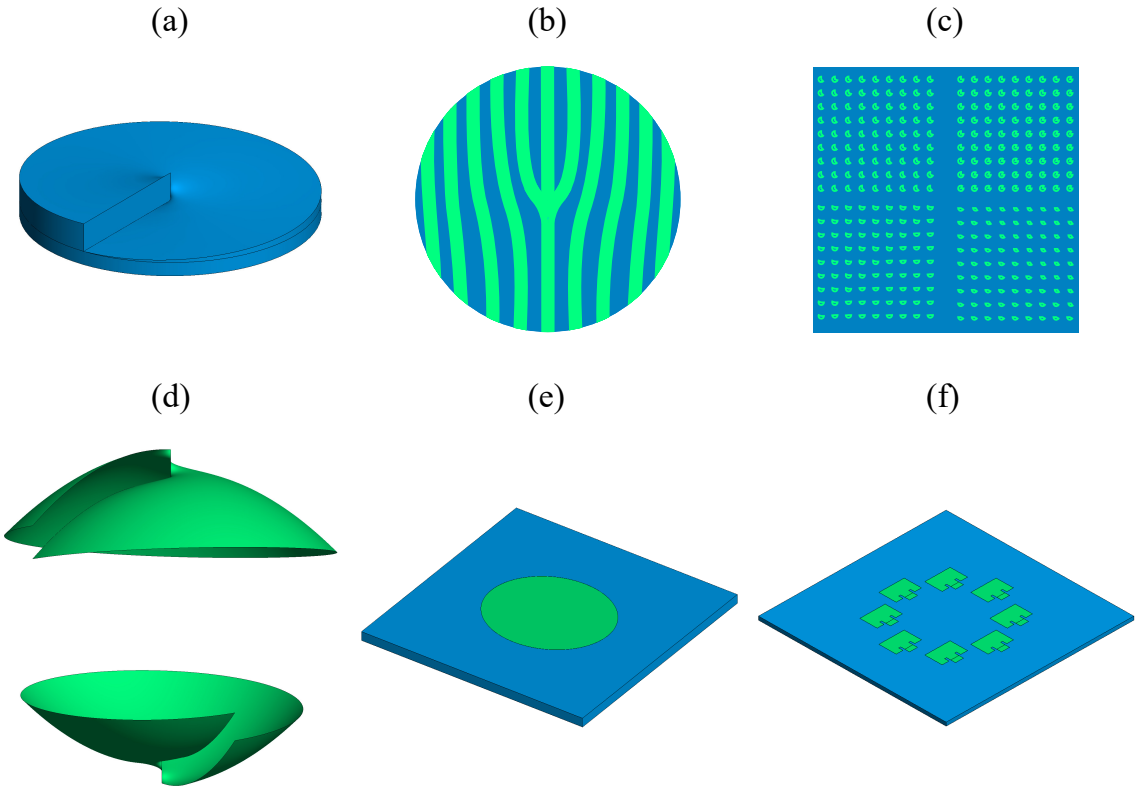

Figure 2.14: Illustration of the available approaches to generate vortex waves spiral phase plate (SPP) (a), holographic diffraction grating (HP) (b), metasurfaces (c), reflector (d), elliptical antenna (e), and uniform circular antenna array (UCA) (f).

the phase, and the polarization of the incident waves in order to generate many kinds of waves such as vortex waves. The metasurfaces have the advantages compared to the other approaches of high degree of functionality, easy production for non-complex unit cells with lower frequencies, and the compactness for some applications. Meanwhile, a conventional azimuthally deformed reflector (twisted reflector) can also modulate the Gaussian beam to vortex beam (cf. Fig. 2.14 (d)). It is a reflective and electrically conductive surface, which converting the field coming from the focal point into vortex beam. As mentioned before, these four approaches belong to vortex waves conversion in contrast to the one single antenna and antenna arrays, which are radiating directly vortex waves. For the case of one specific antenna such as elliptical [67] and octagon patch antenna [68], two different modes are excited and manipulated in the same time to synthesize the required helical beam (cf. Fig. 2.14 (e)). The excited $\mathrm{TM}_{\mathrm{n1}}$ mode is radiated in order to generate the OAM mode order $m = (n - 1)$. However, this approach suffers from the difficult feeding point. All till now discussed approaches have an issue to transmit multiple OAM mode orders. The last approach involves the uniform circular antenna array which paves to be the preferred solution (cf. Fig. 2.14 (f)). The UCA consists of circular arranged antenna

elements with a unifom amplitude distribution and with a specific required phase shift for each antenna element, which depends on the number of antenna elements, and the OAM mode order m. By changing only the phase shift between each adjacent pair antenna, the OAM mode order m can be modified. This mode modification need to be equipped with a controllable Butler matrix (BM) or phase shifters to provide the different OAM mode orders. Nevertheless, this increases the complexity and the costs of the whole system.

2.10 Conclusion

In this chapter, the theory and the basics of the applied methods have been discussed point by point to clarify this work. First of all, the basics of the electromagnetic waves are introduced with Maxwell's equations describing the relationship between the electric, magnetic and current field. Followed by the fundamentals of the antennas, where due to a large number of antenna parameters, there are many types of antennas, which are suitable to be extended to form a group of antennas (antenna array) to steer the beam in many directions if the phases are manipulated in the right way. Then, the scattering parameters are introduced to evaluate the reflected and transmitted waves at the antennas in the presence and absence of an integrated lens or reflector, which can increase the gain if the antennas are located at the focal point. After that, the analysis of the cylindrical dielectric resonator demonstrates the ability to support four different eigenmodes where the RCS is being the highest. Subsequently, the principles and the characterization of the vortex waves are explained through many methods to generate the OAM waves which are split into two categories, namely the generation and the conversion of OAM waves.

Chapter 3

Vortex Waves Generation

The previous chapter focused on the fundamentals and the theory of the vortex waves, the antennas, the beam steering with phased antenna array, the lenses, the reflectors, and the dielectric resonators. It has already been investigated and studied numerically and experimentally in the relevant literature. Among all the approaches of generating vortex waves, which are already discussed in section 2.9, this chapter examines a comparison between the generation of vortex waves using the uniform circular rectangular patch antenna array (UCA) besides the elliptical patch antenna on one side and with a new approach, which is the crossed 2λ-dipole antennas[1] on the other side. This chapter consists mainly of three sections. Initially, the design of a rectangular patch antenna is carried out to be later extended to form a uniform circular rectangular patch antenna array (UCA) thus generating vortex waves. Secondly, an elliptical patch antenna is designed and discussed. Subsequently, a dipole antenna with a length of 2λ is modeled and expanded to configure a crossed 2λ-dipole antennas. Finally, the three approaches are compared in the conclusion.

3.1 Generation of Vortex Waves with Uniform Circular Patch Antenna Array (UCA)

3.1.1 Modeling of Rectangular Patch Antenna

A rectangular patch antenna operating at $10\,\mathrm{GHz}$ is simulated by the full-wave simulator FEKO's solver to be used in the experimental studies. The FEKO's solver uses the Method of Moments

[1] This work has already been published in [72]

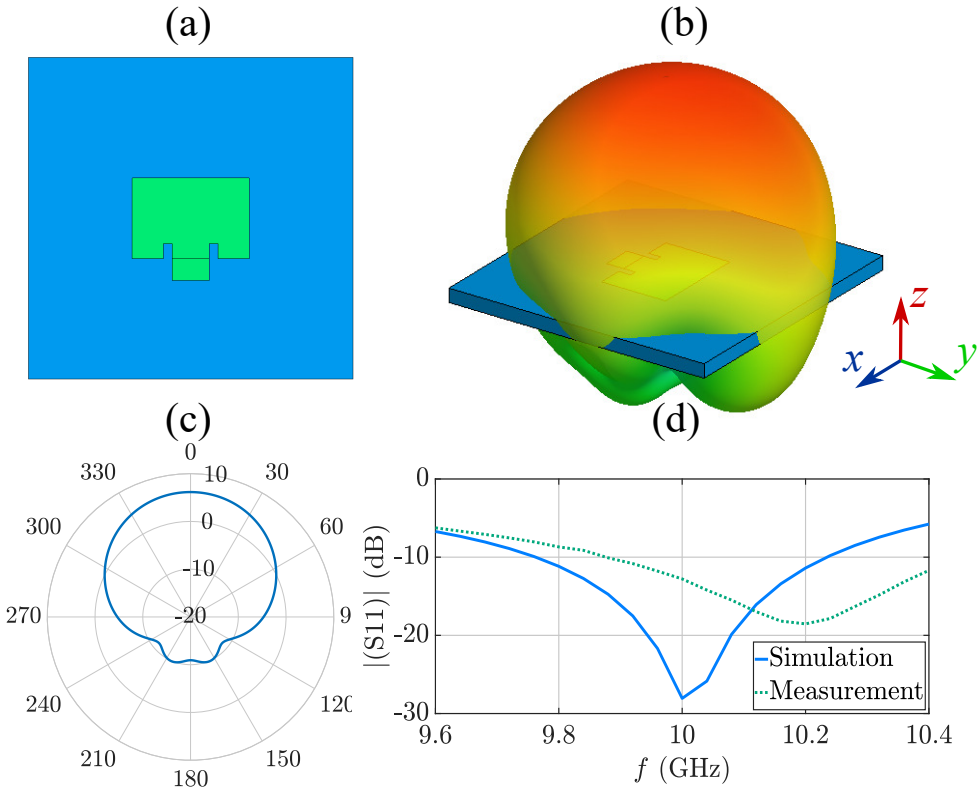

Figure 3.1: The top view of rectangular patch antenna (a), the simulated radiation pattern (dBi) in 3D at 10 GHz (b), the simulated radiation pattern (dBi) in 2D at $\varphi = 0°$ (H-plane) (c), and the simulated and measured return loss S_{11} (d).

(MoM) technique to perform a numerical calculation thus providing a high structure efficiency. The linearly y-polarized patch antenna with a length of $7.4\,\mathrm{mm}$ (about $\lambda_{\mathrm{eff}}/2$) and a width of $10.8\,\mathrm{mm}$ is designed on a Rogers RO4003C substrate characterized with a relative permittivity of 3.55 and a height of $1.524\,\mathrm{mm}$. And, the underlying printed circuit board (PCB) has an area of $30\,\mathrm{mm} \times 30\,\mathrm{mm}$. In Fig. 3.1 (a, b, and c), the top view with the three and the two dimensional radiation pattern of the designed rectangular patch antenna are illustrated. Two insets in the antenna element permit the easy matching between the patch antenna and the $50\,\Omega$ characteristic impedance thus avoiding the reflections of the incident waves in the feeding point and maximizing the realized gain to $6.1\,\mathrm{dBi}$ (c.f. Fig. 3.1 (b, and c)). Furthermore, the simulated return loss S_{11} is about $-28\,\mathrm{dB}$ in contrast to the measured one which is about $-12.7\,\mathrm{dB}$ at the operating frequency of $10\,\mathrm{GHz}$ (Fig. 3.1 (d)). This is caused by the change of the characteristic impedance of the antenna leading to more reflections at the feeding point and to a shift of the resonance frequency to $10.2\,\mathrm{GHz}$.

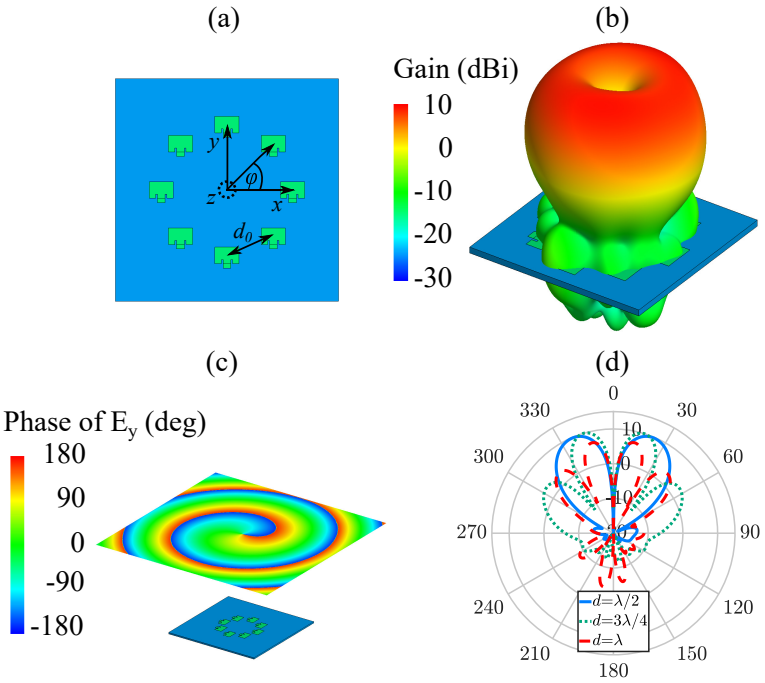

Figure 3.2: Top view of the UCA (a), the simulated radiation pattern (dBi) in 3D of the UCA for the OAM mode order $m = -1$ with a d_0 of $\lambda/2$ (b), the helical phase distribution for the OAM mode order $m = -1$ (c), the simulated radiation pattern (dBi) in 2D of the UCA for the OAM mode order $m = -1$ at $\varphi = 0°$ (H-plane) for an element separation d_0 of $\lambda/2$, $3\lambda/4$, and λ ($\lambda = 30\,\mathrm{mm}$ at $10\,\mathrm{GHz}$) (d).

3.1.2 Extension of Patch Antenna to UCA

In the following, the single patch antenna, already discussed in the previous section, has been extended to constitute a uniform circular patch antenna array (UCA) composed of 8 antenna elements separated by precisely d_0. (c.f. Fig. 3.2 (a)). Upon changing the phase shift φ_1 between each pair of adjacent antenna element, the UCA is able to radiate a vortex beam characterized by a doughnut-shaped radiation pattern (c.f. Fig. 3.2 (b)) and a helical phase distribution (c.f. Fig. 3.2 (c)). Regarding the radiation pattern, the phase in the center of the dark zone is indeterminable thus defining a phase singularity. Whereas for the phase distribution, it changes linearly around the beam axis. The required phase shift φ_1 between each couple of adjacent antennas is defined with the following relation

$$\varphi_1 = \frac{2\pi m}{N}, \tag{3.1}$$

where m denotes the mode order of the vortex waves, and N is the number of the antenna elements. Therefore, with a UCA of 8 antenna elements a phase shift of $45°$ is necessary to

generate the first OAM mode order $m = -1$ (c.f. Fig. 3.2). The direction of the rotation is determined by the right-handed thread, where the clockwise rotation is positive in contrary to the negative one, which is rotating counterclockwise. In order to study the effect of the separation d_0 on the behavior of the vortex waves, the UCA is simulated with three different values of d_0 ($\lambda/2$, $3\lambda/4$, and λ), where the wavelength λ corresponds to $30\,\mathrm{mm}$ at $10\,\mathrm{GHz}$. The two dimensional simulated radiation pattern (dBi) of the UCA for the OAM mode order $m = -1$ at $\varphi = 0^\circ$ (H-plane) of the three scenarios are shown in Fig. 3.2 (d), where it obviously shows that the separation with $d_0 = \lambda/2$ is the best choice. This would cause a higher gain of about $9.5\,\mathrm{dBi}$ and lower side and back lobes, i.e. the larger the radius is, the smaller the gain and the higher the number of side lobes are. The radiation pattern asymmetry is caused by the single-sided, hence asymmetric feeding of each patch antenna element. This asymmetry is more visible at larger radii. Further, the reflection coefficient S_{11} of the antenna elements in the UCA are between $-17\,\mathrm{dB}$ and $-20\,\mathrm{dB}$ at the operating frequency of $10\,\mathrm{GHz}$. The area of the underlying PCB board is $100\,\mathrm{mm} \times 100\,\mathrm{mm}$.

3.2 Generation of Vortex Waves with Elliptical Patch Antenna

Following the discussion of the UCA in the previous section, this section discusses the elliptical patch antenna (c.f. Fig. 3.3 (a)), which, in contrast to the high cost and complexity of the UCA, offers a simple and small configuration with only one specific antenna. The concept of generating the vortex waves via the elliptical patch centers on the simultaneous excitation of the hybridized dual-mode $\mathrm{TM_{n1}}$, where the OAM mode order $m = n - 1$ will be emitted, as shown in Fig. 3.3 (b), where the excited $\mathrm{TM_{21}}$ mode is present at $9.94\,\mathrm{GHz}$, and $10.06\,\mathrm{GHz}$ permitting the radiation of the OAM mode order $m = 1$ at $10\,\mathrm{GHz}$. After the analysis of the eigenmodes with the field simulator Comsol, the resonating frequency between these two modes can radiate a vortex beam. Fig. 3.3 (c) illustared the radiation pattern of the elliptical antenna with a gain of about $2\,\mathrm{dBi}$, while Fig. 3.3 (d) reveals the helical phase front for the $x-$ and $y-$components thus indicating radiation of radially polarized vortex waves for the OAM mode order $m = 1$. Unfortunately, this setup suffers from a high sensitivity with respect to the proper position of the feeding point (probe feed), where the feeding point has to be placed with high precision, otherwise the desired OAM wave emission will be severely compromised. Please note that this antenna can only radiate one or, if necessary, two opposite OAM mode orders simultaneously, and is therefore not suitable for the radiation of other OAM mode orders.

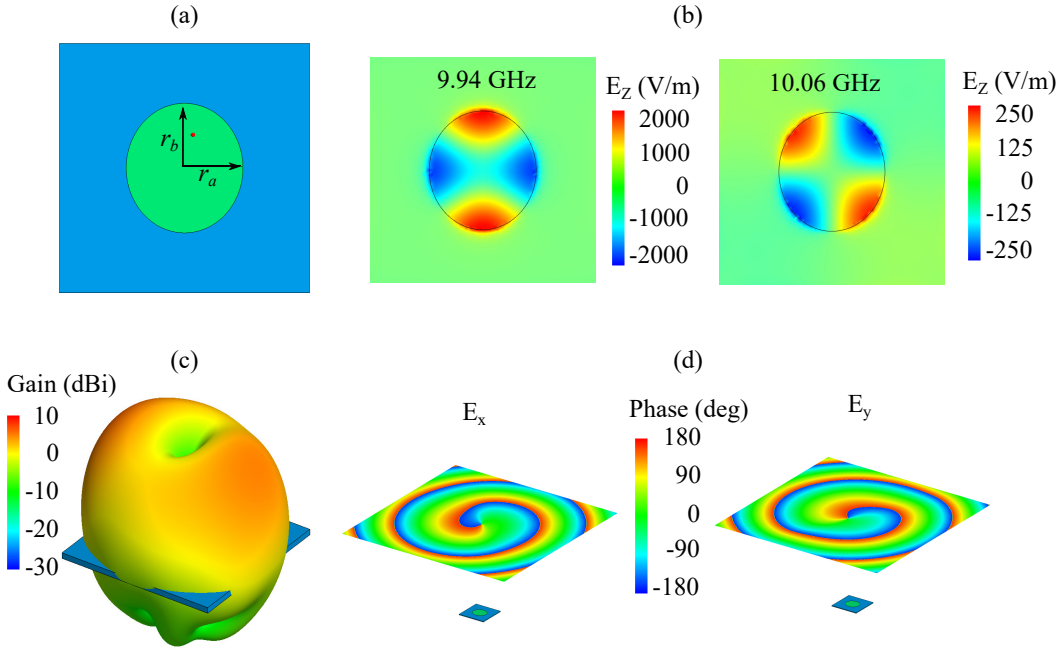

Figure 3.3: Top view of the elliptical patch antenna (a), the two excited eigenmodes TM_{21} at $9.94\,\mathrm{GHz}$, and $10.06\,\mathrm{GHz}$ (b), the simulated radiation pattern (dBi) in 3D of the elliptical patch antenna for the OAM mode order $m = 1$ (c), and the helical phase distribution for the OAM mode order $m = 1$ (d) for $x-$ and $y-$components.

3.3 Generation of Vortex Waves with Crossed 2λ-Dipole Antennas

3.3.1 Modeling of Dipole Antenna

The UCA and the elliptical patch antenna are two promising approaches for radiating OAM waves with many advantages. Unfortunately, they suffer from complexity and expensive equipment in the case of UCA, and in the case of the elliptical antenna from the low gain and the difficulty to set the feed point due to its high sensitivity with respect to the position. Therefore, there is a necessity to develop a new approach that offers a high gain and less complexity. By means of the full-wave simulator FEKO, a single dipole antenna is fed in the center to operate at $10\,\mathrm{GHz}$. Through changing the dipole length l ($\lambda/2$, λ, $3\lambda/2$, and 2λ) the radiation pattern changes automatically. At a length of $\lambda/2$ and λ, the dipole antenna exhibits a maximum gain of $2.1\,\mathrm{dBi}$ and $3.9\,\mathrm{dBi}$ (c.f. Fig. 3.4 (a, and b)) in the broadside direction, respectively. While for lengths of $3\lambda/2$ and 2λ, the maximum gain amounts to $3.6\,\mathrm{dBi}$ and $4\,\mathrm{dBi}$ (c.f. Fig. 3.4 (c, and d)), respectively. Unfortunately, the dipole antenna suffers from the mismatch between the antenna and the characteristic impedance of the feeding port ($50\,\Omega$), which led to a decrease in the gain to $1.4\,\mathrm{dBi}$, $-4\,\mathrm{dBi}$, $2.4\,\mathrm{dBi}$, and $-3.9\,\mathrm{dBi}$ (c.f. Fig. 3.4 (e, f, g and h)) for each of $\lambda/2$,

λ, $3\lambda/2$, and 2λ lengths, respectively. The reflection coefficient S_{11} is depicted from $9\,\mathrm{GHz}$ till $11\,\mathrm{GHz}$ in Fig. 3.5, where the S_{11} is $-7.8\,\mathrm{dB}$, $-0.6\,\mathrm{dB}$, $-6.2\,\mathrm{dB}$, and $-0.7\,\mathrm{dBi}$ for the length l of $\lambda/2$, λ, $3\lambda/2$, and 2λ at $10\,\mathrm{GHz}$, respectively. The mismatch for the cases (λ and 2λ) is due to the difference between the voltage-current ratio and the characteristic impedance ($50\,\Omega$) of the antenna. Therefore, a matching circuit is requested to reduce this mismatch. Fig. 3.6 illustrates the current distribution for the four different cases.

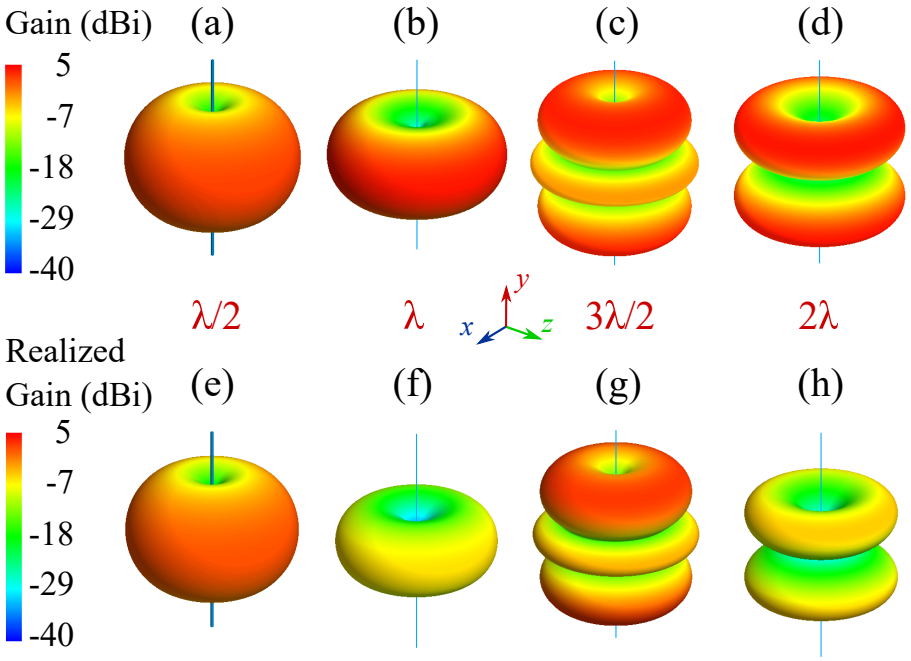

Figure 3.4: The simulated radiation pattern (dBi) (gain (a, b, c, and d)) and (realized gain (e, f, g, and h)) of dipole antennas with a length l of $\lambda/2$ (a, and e), λ (b, and f), $3\lambda/2$ (c, and g) and 2λ (d, and h).

3.3.2 Extension of Dipole Antenna to Crossed 2λ-Dipole Antennas

As shown in the previous section, for the length of 2λ, the radiation pattern behave in a symmetry with respect to the vertical direction (c.f. Fig. 3.4 (d and h) and Fig. 3.6 (d)) but with a $180°$ phase shift. This behavior creates a new possibility of emitting OAM waves with radial polarization ($m = +1$ or $m = -1$), through the use of two crossed 2λ-dipole antennas with a phase shift of $90°$ between them. This approach transmits in two directions (c.f. Fig. 3.7 (a)) due to the multidirectional radiation of the 2λ-dipole antenna. By adding two extra dipoles to the original two, a gain improvement occurs from $1\,\mathrm{dBi}$ to $2.1\,\mathrm{dBi}$ at $\varphi = 90°$, as shown in Fig. 3.7 (b). Due to the field interference of the crossed 2λ-dipole antennas, the emitted gain is low compared to

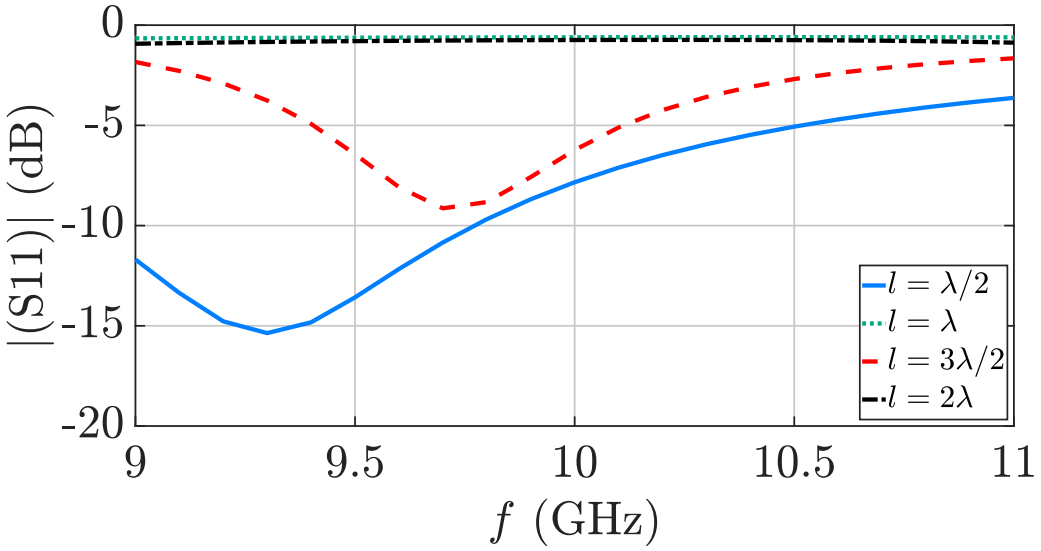

Figure 3.5: The simulated reflection coefficient S_{11} (dB) of the four cases.

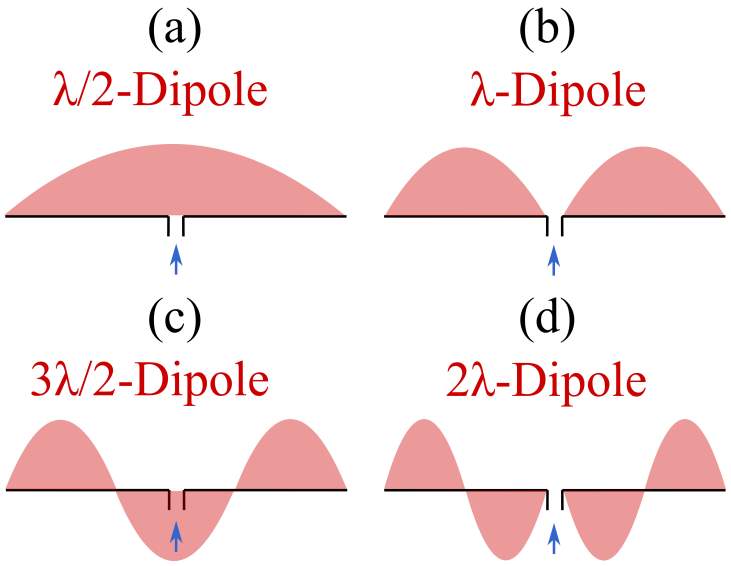

Figure 3.6: The current distribution of the dipole antenna for a length of $\lambda/2$ (a), λ (b), $3\lambda/2$ (c), and 2λ (d).

$\lambda/2$ dipole antenna, leading to the beam divergence. The phase shift φ_{cross} between the adjacent dipoles is given by

$$\varphi_{cross} = \frac{\pi}{N}, \tag{3.2}$$

where N is the number of crossed 2λ-dipole antennas ($N \geq 2$). By introducing the same crossed 2λ-dipole antenna configuration at a distance of $\lambda/4$ in parallel to the prior dipole configuration

with the aid of a corresponding excitation with phase difference of $\pi/2$, a unidirectional radiation effect can be obtained, which can be termed crossed 2λ-dipole phased array. Therefore, by using this concept of the crossed 2λ-dipole phased array with two or four dipole antenna elements, the gain is raised to $2.4\,\mathrm{dBi}$, and $4.8\,\mathrm{dBi}$ at $\varphi = 90°$ (c.f. Fig. 3.7 (c, and d)), respectively. One PEC

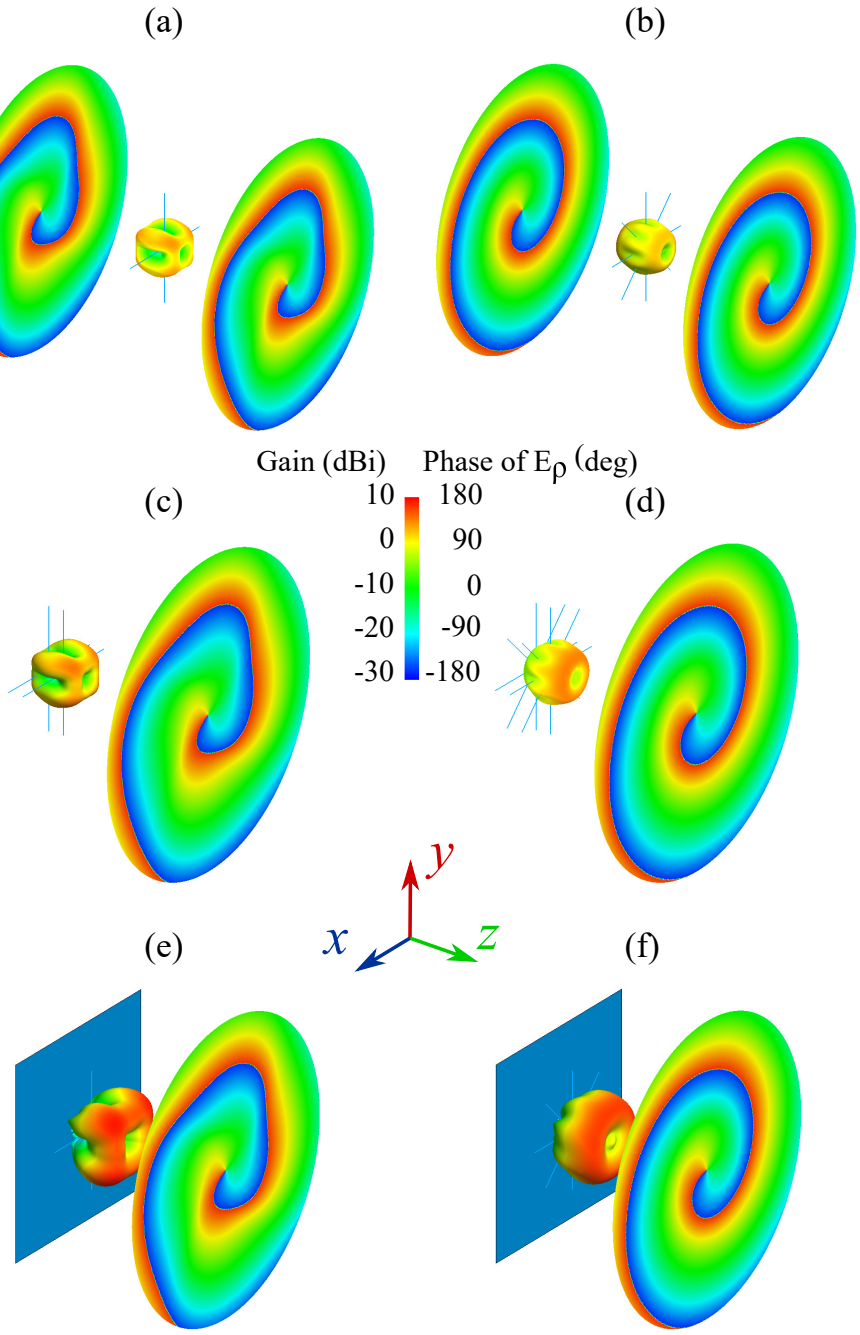

Figure 3.7: The simulated radiation pattern (dBi) of two (a) and four (b) crossed 2λ-dipole antennas, of two (c) and four (d) crossed 2λ-dipole phased array with 2 elements, and of two (e) and four (f) crossed 2λ-dipole antennas with a reflector for a distance of $\lambda/4$ and an area of $100\,\mathrm{mm} \times 100\,\mathrm{mm}$.

reflector ($100\,\mathrm{mm} \times 100\,\mathrm{mm}$) located at a distance of $\lambda/4$ is also able to enhance the gain to $6.6\,\mathrm{dBi}$ and $7.5\,\mathrm{dBi}$ at $\varphi = 90°$ (c.f. Fig. 3.7 (e, and f)). This enhancement in gain is primarily due to the single-directive OAM wave radiation.

3.4 Conclusion

In this chapter, among the various possibilities for generating vortex waves, three of them are discussed and evaluated. The first two approaches are the conventional uniform circular antenna array UCA and the elliptical patch antenna. While the third is a new approach based on crossed 2λ-dipole antennas. The UCA has the benefit of generating any OAM mode order in the presence of a Butler matrix (BM). It can also increase the gain while reducing the beam divergence by increasing the number of antenna elements or by using highly directional antenna elements such as horn antenna or Vivaldi antenna. However, it suffers from a heavy system that uses a large number of antennas, coaxial cables and BM. On the other hand, the elliptical antenna approach offers the simplicity and low cost of the whole system, but at the same time, it does not provide high gain and suffers from the difficulty of setting the feeding point. The newly proposed approach provides a simple system that requires only two or more 2λ-dipole antennas. Nevertheless, this approach requires an additional matching circuit to avoid reflections at the feeding point which cannot be easily integrated into a system device. In summary, the UCA approach is chosen to be applied in the next chapters to generate OAM waves.

Chapter 4

Vortex Beam Steering

In the prior chapter, the main topic was the generation of OAM waves. Among the various approaches, three of them (UCA, elliptical patch antenna and crossed 2λ-dipole antennas) are mainly discussed and evaluated. Regretfully, the concept of the crossed 2λ-dipole antennas and the elliptical patch antenna are not suitable for our purposes, therefore this chapter and the following are treated with the UCA. The vortex waves are affected from many issues, but the misalignment between the OAM transmitter and the OAM receiver, and the high beam divergence are the crucial ones. This chapter focuses on the beam steering of vortex waves (OAM beam steering[1]), providing a way to solve the misalignment issue, which is very critical for some applications such as OAM communication (SISO or MIMO). At first, a UCA of 8 antenna elements is proposed in this chapter to radiate and steer the OAM beam. While in the second section, a UCA with various subarrays is used for the same purpose. In the end, the results of the different methods are discussed and concluded in the last section.

4.1 OAM Beam Steering by Using UCA with 8 Antenna Elements

In this section, in order to generate OAM waves a UCA with 8 antenna elements operated at $10\,\mathrm{GHz}$ and with a d_0 of $15\,\mathrm{mm}$ ($\lambda/2$) is designed with the full-wave simulator HFSS, which applies the Finite Element Method (FEM). The required phase shift φ_1 (3.1) between each couple of adjacent antennas is $45°$ so that the OAM mode order would be $m = -1$. Fig. 4.1 presents the top (e) and the side view (f) of the UCA, where ϑ is the elevation angle varying from $0°$ to $180°$, and also the steered angle of the OAM beam, which is the main topic of this chapter. An

[1] This study is already published in [73]

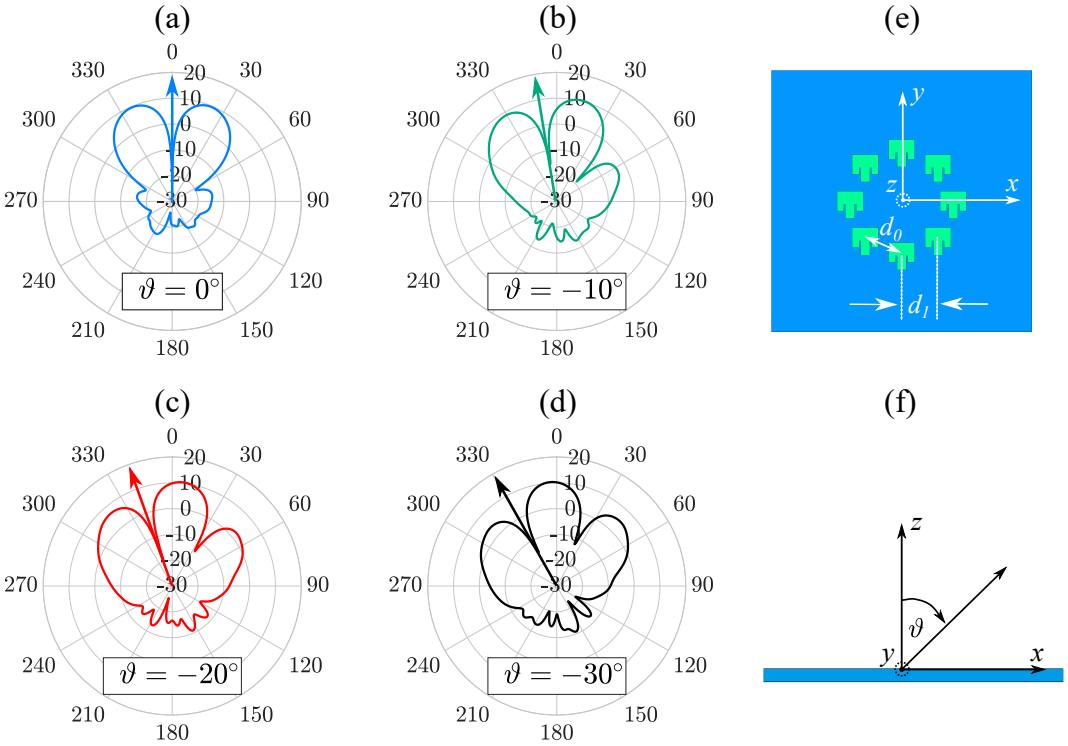

Figure 4.1: The radiation pattern (dBi) in 2D at $\varphi = 0°$ of the steered OAM beam of the UCA with 8 antenna elements for the angles $\vartheta = 0°$ (a), $-10°$ (b), $-20°$ (c) and $-30°$ (d), and the illustration of the top (e) and the side view (f) of the UCA with 8 antenna elements.

additional phase shift φ_2 is necessary for steering the OAM beam in the required beam direction (ϑ), where the two phase shifts φ_1 and φ_2 will be superimposed

$$\varphi_2 = \frac{360 d_1 \sin(\vartheta)}{\lambda}, \tag{4.1}$$

where d_1 is the distance between the two adjacent antenna elements on the x-axis, λ is the wavelength in the free space, and ϑ is the desired steered angle. In order to evaluate the OAM beam steerability, a cross-sectional image of the doughnut-shaped OAM radiation pattern is chosen, which is supposed to be the direction of steerability, namely the xz-plane for our case, cf. 2.2. Two lobe-like curves are recognized on the cross-sectional image, where the $3\,\mathrm{dB}$ gain difference between the maximum gain of each lobe-like curves will be the criterion to evaluate the steering. That means, as long as the gain difference between these lobe-like curves is less than $3\,\mathrm{dB}$, the steeribility is acceptable. This criterion is inspired from the principle of the half power beam width (HPBW). In this section, the OAM beam is steered from $\vartheta = 0°$ till $\vartheta = -30°$, where Fig. 4.1 reveals that the OAM beam steering operates well till $\vartheta = -20°$. In Fig. 4.2, the top and the side view of the radiation pattern of the non-steered (a, and b) and the steered OAM

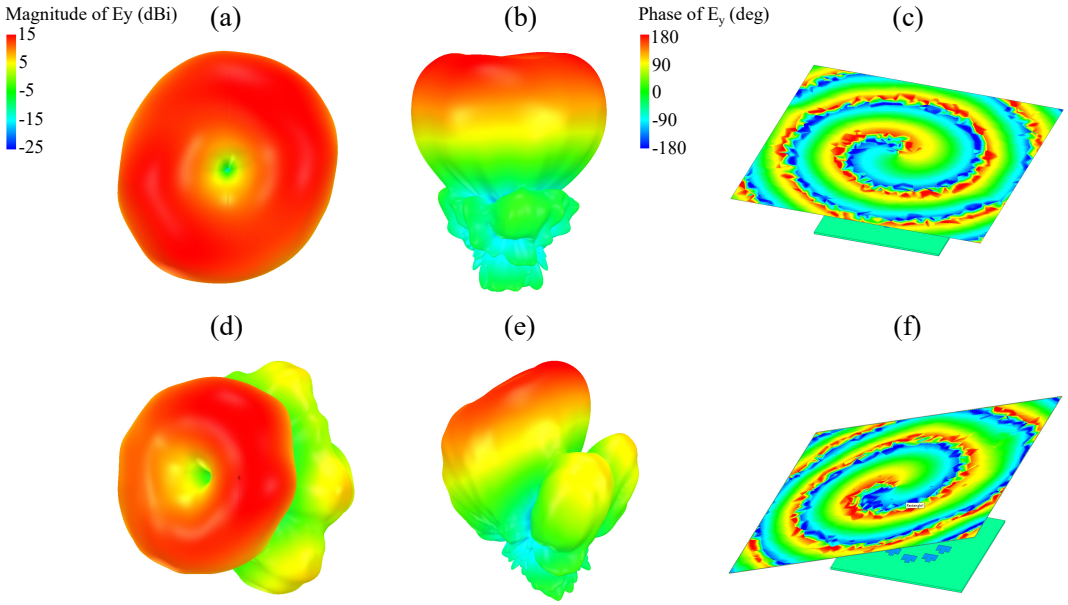

Figure 4.2: The top and the side view of the radiation pattern (dBi) in 3D of the non-steered (a, and b) and the steered OAM beam of the UCA with 8 antenna elements (d, and e), and the phase distribution of the non-steered (c) and the steered OAM beam of the UCA with 8 antenna elements ($\vartheta = -20°$) (f).

beam at $\vartheta = -20°$ (d, and e) are depicted. Meanwhile, the helical phase front excluding (c) and including steering (f) are illustrated.

4.2 OAM Beam Steering by Using UCA with Subarrays

Similarly, the single patch antenna is extended to build a circular patch array composed of 4 elements rather than 8 elements separated by $d_0 = 3\lambda/2$ thus having sufficient space to replace the individual patch antennas with 3 different subarrays. Therefore, the dimension of the underlying PCB board becomes now $140\,\mathrm{mm} \times 140\,\mathrm{mm}$. The individual patch antennas are replaced by different arrangements, namely linear, rectangular and circular subarrays (c.f. Fig. 4.3). The approach with 8 antenna elements is illustrated in Fig. 4.3 (a) to simplify the understanding of the new four scenarios. Unfortunately, the increasing of d_0 leads to more side lobes, which causes some distortions and gain reduction in the broadside direction. Regarding the case of the UCA with 4 antenna elements, the maximum gain (Fig. 4.4 (a)) amounts to $6.4\,\mathrm{dBi}$ for the OAM mode order $m = -1$. The lower gain is due to the decline of the number of the antenna elements N and also due to the large separation between the antenna elements $d_0 = 3\lambda/2$. Here, the two phase shifts in (3.1) and (4.1) are still in use. As well as, the use of the

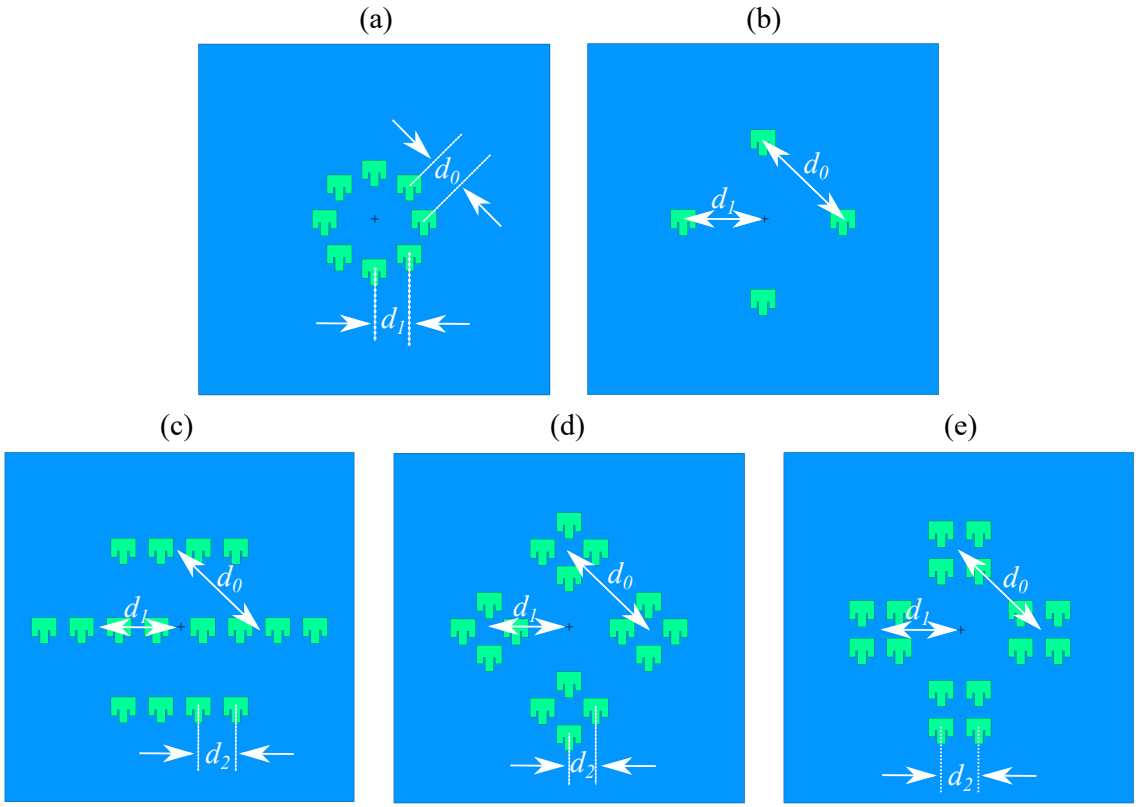

Figure 4.3: The illustration of the UCA with 8 antenna elements $d_0 = \lambda/2$ (a), with 4 antenna elements $d_0 = 3\lambda/2$ (b), with linear subarray (c), with circular subarray (d), and with rectangular subarray (e).

subarray requires a third phase shift φ_3. This is related to the subarray, which can be called local subarray phasing indicating the phase difference between the antenna elements in the subarray. φ_3 is defined by

$$\varphi_3 = \frac{360 d_2 \sin(\vartheta)}{\lambda}, \tag{4.2}$$

where d_2 is the distance between the two adjacent antenna elements in the subarray on the x-direction, ϑ is the desired steered angle, and λ is wavelength in the free space. The beam steering works well up to $\vartheta = -20°$. The same criterion (3 dB gain deviation between the two lobes) already used in the previous section is used here and is also used with the next three cases. In Fig. 4.5, the two dimensional radiation pattern at $\varphi = 0°$ for the approach using 4 antenna elements for OAM mode order $m = -1$ is presented. In the three cases with subarrays, the beam is steered from $\vartheta = 0°$ till $\vartheta = -50°$. In case of linear subarray, the steering operates well from $\vartheta = -20°$ to $\vartheta = -40°$, where the average gain is about 7.2 dBi, 0.8 dB more than the case of 4 antenna elements without subarray (c.f. Fig. 4.5). However, this abnormal reaction of the

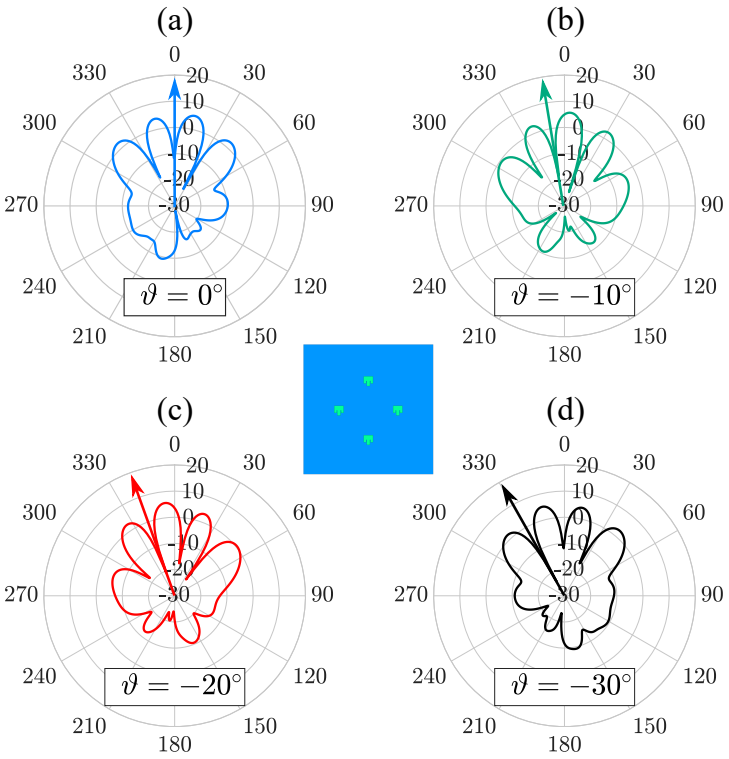

Figure 4.4: The radiation pattern (dBi) in 2D at $\varphi = 0°$ of the steered OAM beam with 4 antenna elements for the angles $\vartheta = 0°$ (a), $-10°$ (b), $-20°$ (c) and $-30°$ (d).

linear subarray is influenced by the asymmetrical deformation of the radiation pattern of one single patch antenna element, i.e. the radiation pattern in 2D at $\varphi = 0°$ and $\varphi = 90°$ of a linear patch antenna array is non-symmetrical. In addition, a linear subarray can not be applied to steer the OAM beam in all directions in contrast to the other approaches. Fig. 4.6 depicts the beam steering of the circular subarray case, whose steering works fine from $\vartheta = 0°$ till $\vartheta = -20°$, and its gain changes between $11.2\,\mathrm{dBi}$ and $8.2\,\mathrm{dBi}$. While, the rectangular subarray functions well from $\vartheta = 0°$ till $\vartheta = -30°$, and shows a gain between $11.5\,\mathrm{dBi}$ and $9\,\mathrm{dBi}$ (c.f. Fig. 4.7). As a summary, the rectangular OAM array is the best option, providing a beam steering up to $\vartheta = -30°$, an increase in gain from $6.4\,\mathrm{dBi}$ (4 antenna elements with d_0 of $3\lambda/2$) to about $11.5\,\mathrm{dBi}$, and a decrease in the vortex beam divergence from the angle $\vartheta = 23°$ (8 antenna elements with d_0 of $\lambda/2$) to $\vartheta = 13°$. Unfortunately, this case suffers from the side lobes due to the wider separation between the antennas, unlike the case of the ordinary 8 antenna elements, where the distance between the antennas is only $\lambda/2$ rather than $3\lambda/2$. In Fig. 4.8, the top and the side view of the radiation pattern of the non-steered (a, and c) and the steered OAM beam with rectangular subarray at $\vartheta = -20°$ (b, and d) are depicted. Moreover, the helical phase front without (e) and with steering (f) are illustrated.

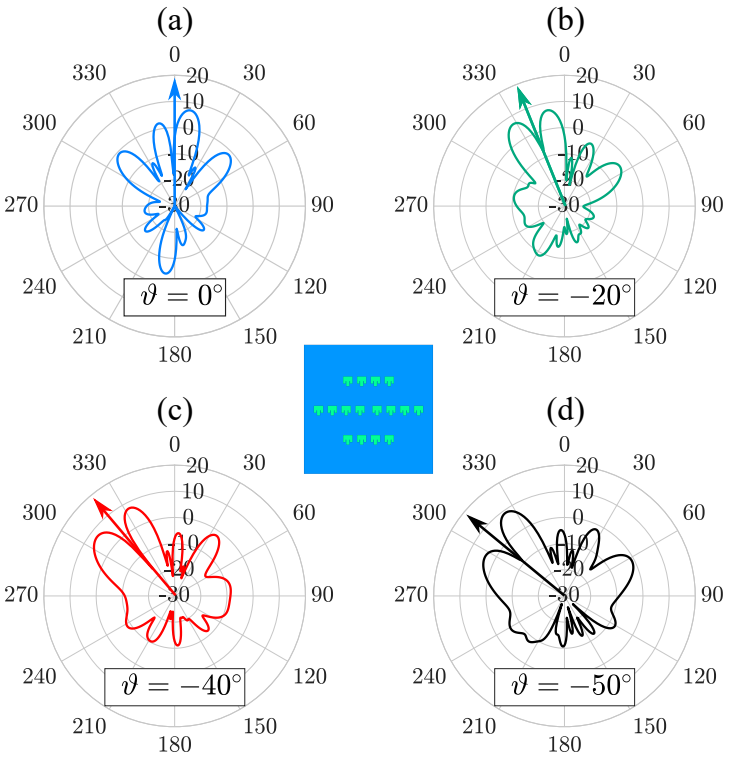

Figure 4.5: The radiation pattern (dBi) in 2D at $\varphi = 0°$ of the steered OAM beam with linear subarray for the angles $\vartheta = 0°$ (a), $-20°$ (b), $-40°$ (c) and $-50°$ (d).

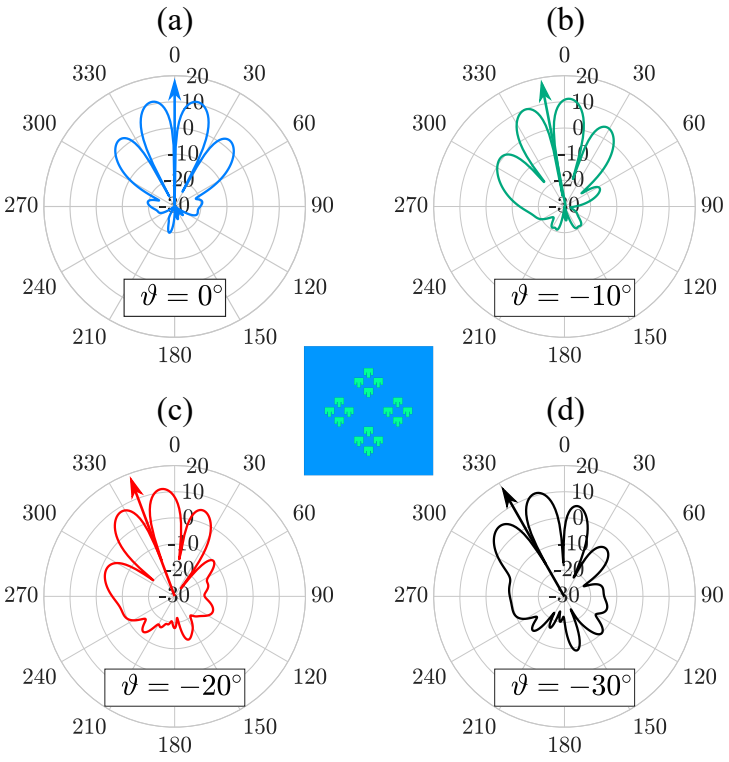

Figure 4.6: The radiation pattern (dBi) in 2D at $\varphi = 0°$ of the steered OAM beam with circular subarray for the angles $\vartheta = 0°$ (a), $-10°$ (b), $-20°$ (c) and $-30°$ (d).

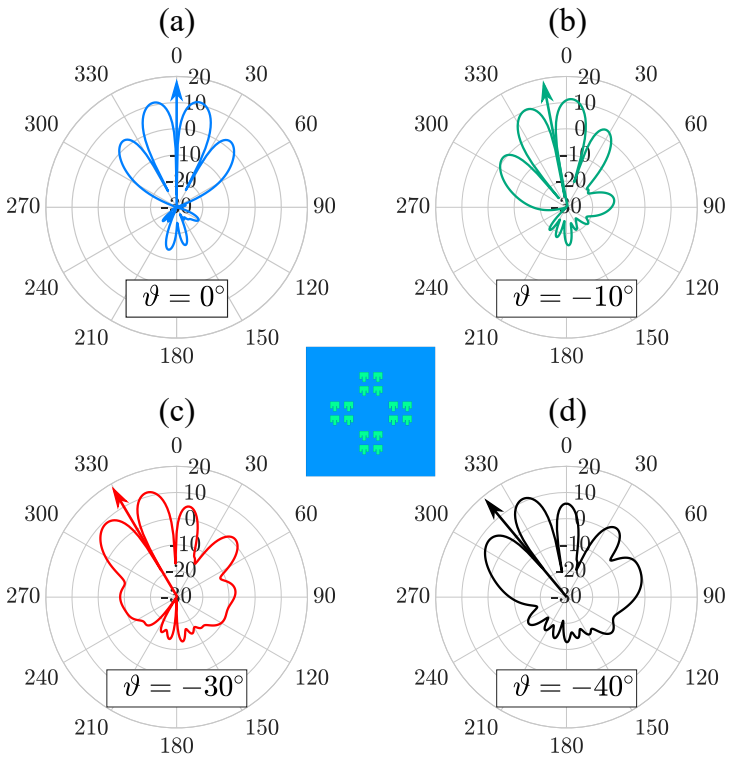

Figure 4.7: The radiation pattern (dBi) in 2D at $\varphi = 0°$ of the steered OAM beam with rectangular subarray for the angles $\vartheta = 0°$ (a), $-10°$ (b), $-30°$ (c) and $-40°$ (d).

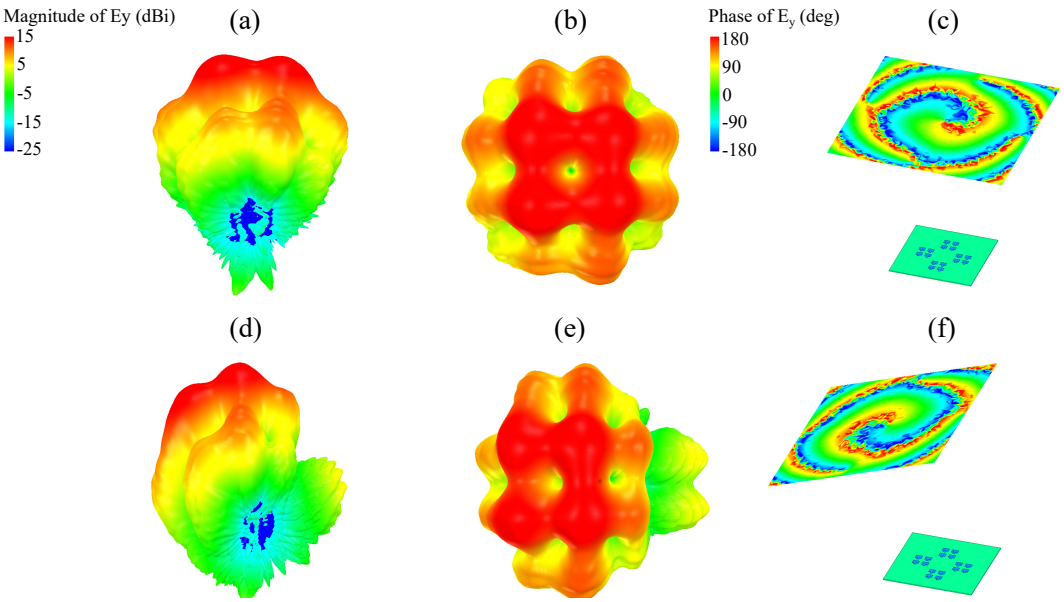

Figure 4.8: The top (a, and b) and the side view (c, and d) of the radiation pattern (dBi) in 3D of the non steered (a, and c) and the steered OAM beam with rectangular subarray (b, and d), and the phase distribution of non steered (a) and the steered OAM beam with rectangular subarray ($\vartheta = -20°$) (b).

4.3 Conclusion

This chapter has demonstrated that the OAM beam can be steered similarly to the directional beam of a phased array antenna. This is achieved by changing the phase shift between each pair of adjacent antennas. Several approaches are simulated and evaluated. The UCA approach with 8 antenna elements has the advantage of lower side lobe level due to separation of the antennas d_0 of $\lambda/2$, while the UCA with rectangular subarrays has a wider steering angle compared to the linear and the circular one. Furthermore, the methods with subarray have also the ability to decrease of the OAM beam divergence.

Chapter 5

Vortex Beam Divergence Reduction

The preceding chapter has highlighted the OAM beam steerability which is beneficial for the alignment between an OAM transmitter and an OAM receiver. Hence, it enables communication via vortex waves. Not only does this issue occur, but the large OAM beam divergence[1] is also a critical point that has to be solved for many applications such as the target localization by means of vortex waves where higher OAM mode orders are required. Therefore, the problem concerning the divergence is the headline of this chapter, where a tailored lens and reflector are implemented to reduce the divergence and solve this problem. First, a conventional and a tailored lens are designed and simulated to be compared to each other and are also verified experimentally. Secondly, a comparison between a conventional and tailored reflector is carried out with OAM impressed field source and with realistic feeding antenna structure, which can affect the radiation of the reflector. Moreover, the two reflectors are fabricated and measured. Finally, the last section discusses and concludes the two approaches.

5.1 Divergence Reduction with Conventional and Tailored Lens

5.1.1 Design and Evalutaion of the two Lenses

At first, a lens is used to be mounted on the UCA approach in order to reduce the beam divergence. Hence, in this section the conventional and the tailored lens are selected for comparison, which are made of polypropylene (PP) with a 2.2 relative permittivity. However, the dielectric loading induces a change in the effective permittivity of the patch antenna, therefore the antennas have to

[1] Parts of this chapter have been published in [74], and [75]

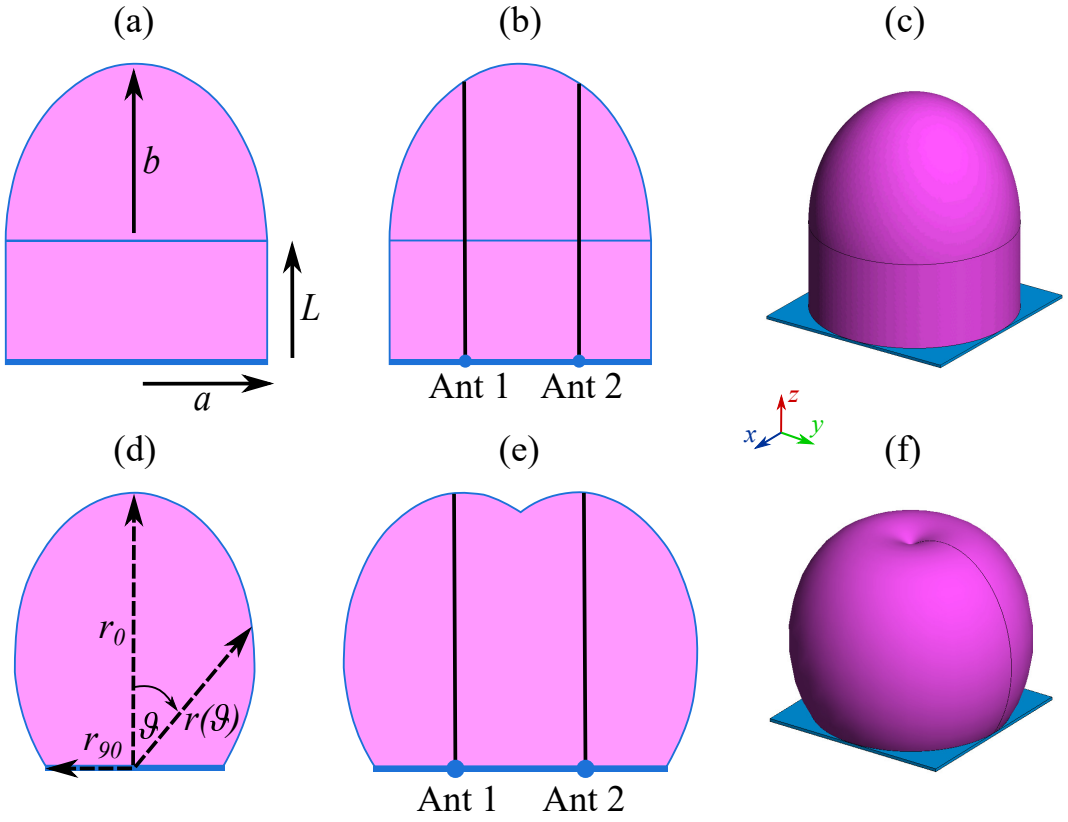

Figure 5.1: The conventional lens (a, b, and c), and tailored lens (d, e, and f).

be redesigned accordingly. Thus, the modified length and width of the patch antenna element are $7.25\,\mathrm{mm}$ and $10.2\,\mathrm{mm}$, respectively. In addition, the new reflection coefficient S_{11} for the redesigned patch antenna element is $-37.6\,\mathrm{dB}$ at $10\,\mathrm{GHz}$. As shown in Fig. 5.1 (a, b, and c), the conventional lens consists of two elements, namely the cylindrical dielectric part and the ellipsoidal part. The cylindrical dielectric part moves the focal point to the UCA center, whereas the ellipsoidal part transforms the divergent spherical waves into a narrower plane wave beam. Therefore, the gain of the UCA is expected to be increased, while the divergence would correspondingly be decreased. The design of the conventional lens is based on the following equations [76]

$$b = \frac{a}{\sqrt{1 - \frac{1}{\mathcal{R}e(\varepsilon_r)}}}, \tag{5.1}$$

$$L = \frac{b}{\sqrt{\mathcal{R}e(\varepsilon_r)}}, \tag{5.2}$$

$$D[\mathrm{dB}] = 20\log_{10}\left(\frac{2\pi a}{\lambda}\right), \tag{5.3}$$

where a denotes the semi-minor axis of the ellipsoidal part along the z-axis, which depends on the target directivity in [dB]. b represents the semi-major axis. L is considered as the length of the extension part, and λ is the operating wavelength which happens to be $30\,\mathrm{mm}$ at $10\,\mathrm{GHz}$. The equation (5.3) seems to assume an aperture efficiency of $100\,\%$ which according to OAM antennas is most likely different. To simplify the assembling and the centering between the PCB board with UCA and the lens, a is chosen to be $50\,\mathrm{mm}$, while the separation d_0 is $15\,\mathrm{mm}$ ($\lambda/2$). Therefore, L and b are $45.6\,\mathrm{mm}$, and $67.7\,\mathrm{mm}$, respectively. Nevertheless, the principle of Fermat allows to design a lens for a single patch antenna [43]

$$r(\vartheta) = \left(\frac{r_0(n_1 - n_0)}{n_1 - n_0\cos(\vartheta)}\right), \tag{5.4}$$

where n_1 represents the refractive index of the lens with the value of 1.483 , whereas n_0 denotes the refractive index of the air with values of 1 . The radius of the lens $r(\vartheta)$ depends on the polar angle ϑ, so r_0 is the radius at the polar angle $\vartheta = 0°$. As shown in Fig. 5.1 (d, e, and f), the shape function (5.4) designs the tailored lens by means of sweeping this function which is moved to be aligned with the center of the patch antenna around the z-axis (body of revolution approach). Just like the conventional lens, the whole PCB board is covered to facilitate the assembling of the lens with the UCA. Therefore, the radius at the polar angle $\vartheta = 0°$ and $\vartheta = 90°$ are about $93\,\mathrm{mm}$ and $30.4\,\mathrm{mm}$, respectively. When r_0 increases, the gain of the antenna increases inversely to the divergence which decreases accordingly. The gain of the UCA for the OAM mode order -1 with the conventional lens rises from about $9.5\,\mathrm{dBi}$ to $11.3\,\mathrm{dBi}$ as shown in Fig. 5.2 (b). Similarly, the number of the side lobes increases leading automatically to the reduction of the gain and the beam divergence. In opposite, the tailored lens (cf. Fig. 5.2 (b)) reveals a significant decrease in the beam divergence with a maximum gain that has a value of $15.3\,\mathrm{dBi}$. Moreover, the number of side lobes is less than with the conventional lens. The aperture of the two lenses are not identical, where the effective aperture A_e, and the physical aperture A_{phys} are specified with [1]

$$A_e = \frac{\lambda^2 G}{4\pi}, \tag{5.5}$$

$$A_{phys} = \pi r_{max}^2, \tag{5.6}$$

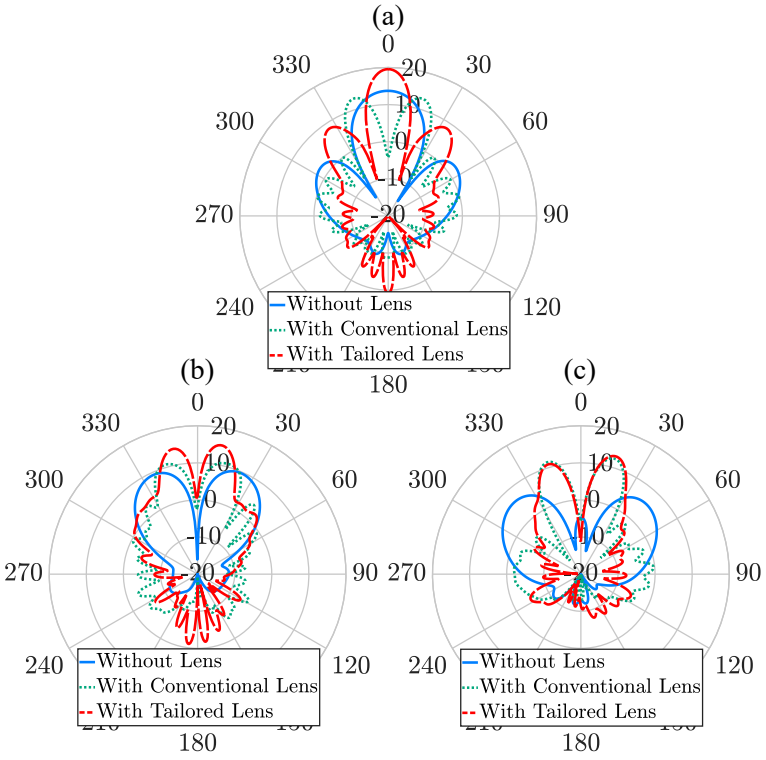

Figure 5.2: The simulated radiation pattern (dBi) of UCA at $\varphi = 0°$ (H-plane) for the cases of without lens, with conventional lens and with tailored lens for the OAM mode order 0 (a), -1 (b), and -2 (c).

$$e_a = \frac{A_e}{A_{phys}}, \tag{5.7}$$

where λ denotes the wavelength in the free space, whereas G signifies the gain of the antenna. r_{max} is indicated by a for the conventional lens (cf. Fig 5.1 (a)), whereas it regards the maximum of $r(\vartheta)\sin(\vartheta)$ for the case of tailored lens (cf. Fig 5.1 (d). The relationship between the effective aperture and the physical one defines how effectively an antenna can be upon receiving the electromagnetic waves. This relationship is termed the aperture efficiency e_a of a range value between 0 and 1. Taking into account the conventional lens, its aperture efficiency is 0.12 as opposed to the tailored lens which has 0.21 value. Thus, the tailored lens is superior over the conventional. In Fig. 5.2 (a), the mode order 0 is shown, but it is deformed by the conventional lens, meanwhile the tailored lens improves the gain from $13.7\,\mathrm{dBi}$ to $19.5\,\mathrm{dBi}$. This beam deformation of the zeroth mode order with the conventional lens occurs due to the shift of the antennas from the focal point of the lens yielding a refraction of the waves in an undesired direction. By increasing the aperture size of the lens, the displacement error decreases, and the issue would be minimized. This abnormal behavior of the conventional lens with the zeroth

mode gives priority to the tailored lens over the conventional one, in particular when applied in the OAM target localization, where several OAM mode orders are essential to locate the target. In Fig. 5.2 (c), when the mode -2 is chosen, the two lenses yield similar gain improvements, but with higher side lobe suppression levels with the tailored lens. Note that the maximum gain with the second mode order can be reached by using a distance d_0 of about λ between the adjacent antenna elements (cf. Fig. 3.2 (a)). Therefore, the difference in size between the conventional and the tailored lens will be very far-reaching giving additional advantage for the tailored lens. Figs. 5.3 and 5.4 represents the instantaneous electric field and the phase distribution of the OAM mode order -1 of the cases without lens (a), with conventional lens (b) and with tailored lens (c).

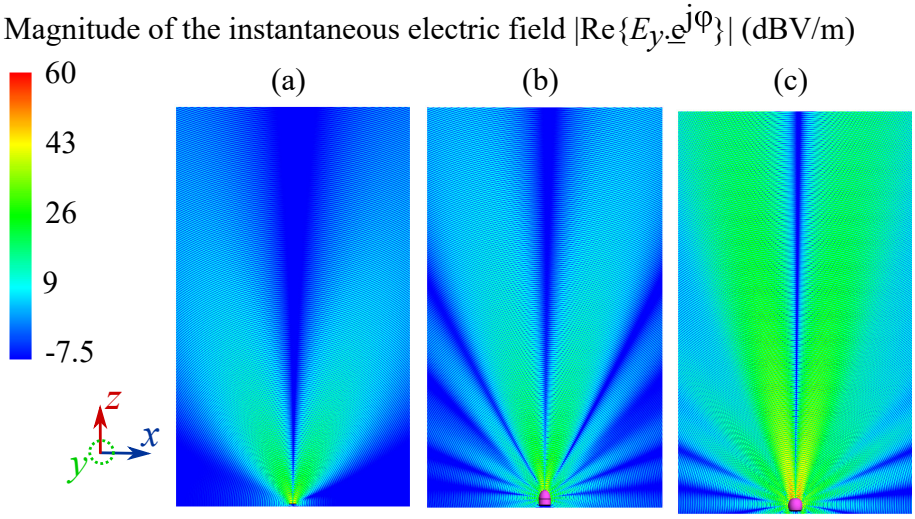

Figure 5.3: The simulated magnitude of the instantaneous electric field for the OAM mode order -1 of the cases without lens (a), with conventional lens (b), and with tailored lens (c).

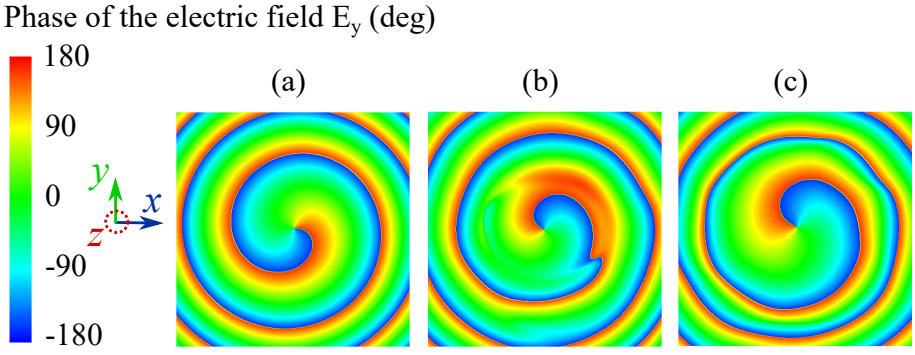

Figure 5.4: The simulated phase distribution for the OAM mode order -1 of the cases without lens (a), with conventional lens (b), and with tailored lens (c).

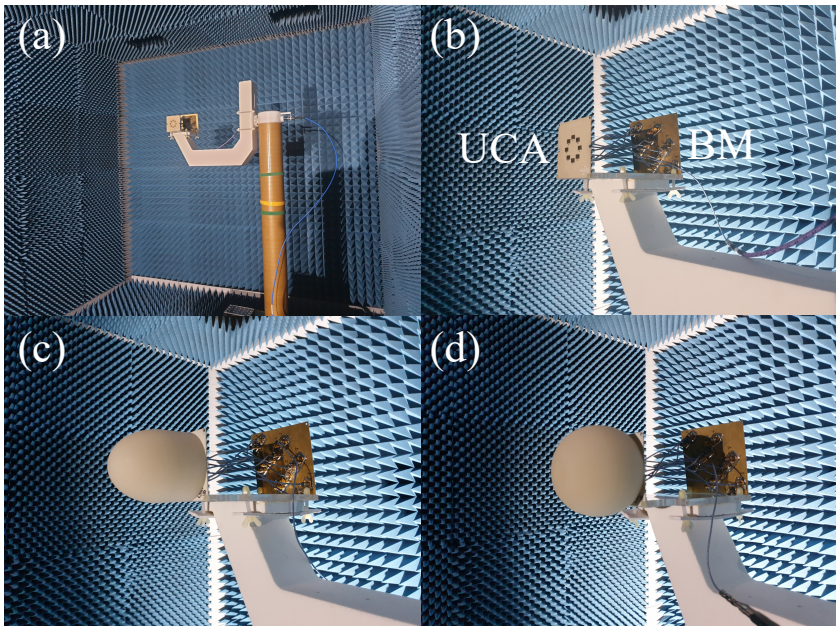

Figure 5.5: The rotary table in the anechoic chamber (a), the manufactured UCA with Butler matrix (BM) (b), the conventional lens on the UCA (c), and the tailored lens on the UCA (d).

5.1.2 Experimental Verification

After the satisfactory results in the ideal simulation part, where the environment is very ideal, the designed conventional and tailored lens in the previous section have been produced by an external company with the aid of a 3D printing machine to be evaluated in the real physical environment. The measurement is carried out by a vector network analyzer (VNA) ZVA 40 from Rohde & Schwarz in an anechoic chamber thus avoiding undesired distortions and reflections. The lens mounted on the UCA in addition to the Butler matrix (BM) are employed as a receiver, while a standard gain horn antenna is employed as a transmitter. The BM is responsible for the delivery of the various OAM mode orders. The distance between the transmitter and the receiver is about $5\,\mathrm{m}$ where the lens, together with the UCA and the BM, are installed on a rotary table which rotates at the elevation angle ϑ from $45°$ till $135°$, and in the azimuth angle φ from $0°$ to $180°$. The OAM mode order $m = 1$ is provided by the $8{\times}8$ BM which is connected to the UCA by eight coaxial cables with the same length of $200\,\mathrm{mm}$ (cf. Fig. 5.5). In addition, the two lenses are separately mounted on the UCA (cf. Fig. 5.5 (c, and d)) to be validated. The gain without lens, with conventional lens and with tailored lens are shown in Fig. 5.6 (a, b, and c), respectively. In comparison to the others, the tailored lens achieved a further superior performance by decreasing the beam divergence more. In addition, the gain is enhanced by $1.7\,\mathrm{dBi}$ to reach $9.7\,\mathrm{dBi}$ level with respect to the conventional lens and by $4.8\,\mathrm{dBi}$ reaching $12.8\,\mathrm{dBi}$ in the case of the tailored

lens. Meanwhile, in Fig. 5.6 (d, e, and f) the radiation exhibits a helical phase distribution of one helix which declares the maintenance of the first OAM mode order. An OAM mode of order m is denoted by the number of helices m in the phase front with a phase distribution of $\alpha(\varphi) = m\varphi$ noting that φ varies between 0 and 2π. The sign of the OAM mode orders is performed by the right-handed thread in which the vortex waves undergo clockwise rotation in contrary to the negative modes rotating in a counter-clockwise direction. Fig. 5.7 illustrates the measured gain in 2D (H-plane) of the three cases for the first (a) and second (b) OAM mode order. Contrary to the ideal case, it is remarkable that the gain in the center of the radiation pattern is not 0 (linear). Several reasons exist for this, including the reflections in the BM and the misalignment between the transmitter and the receiver. And with even more observation, higher divergence is noted when the OAM mode orders are executed.

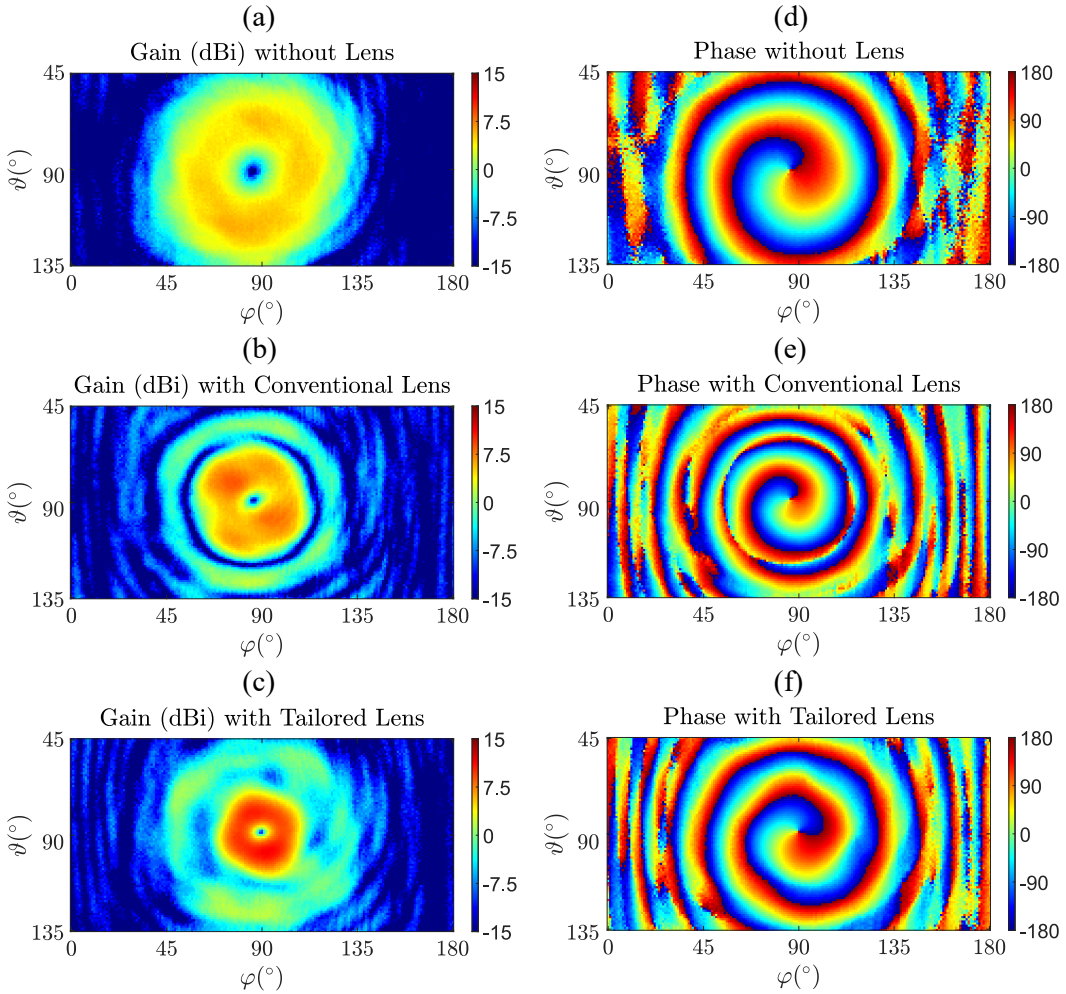

Figure 5.6: The measured gain and phase distribution for the OAM mode order 1 of UCA without lens (a, and d), with conventional lens (b, and e), and with tailored lens (c, and f).

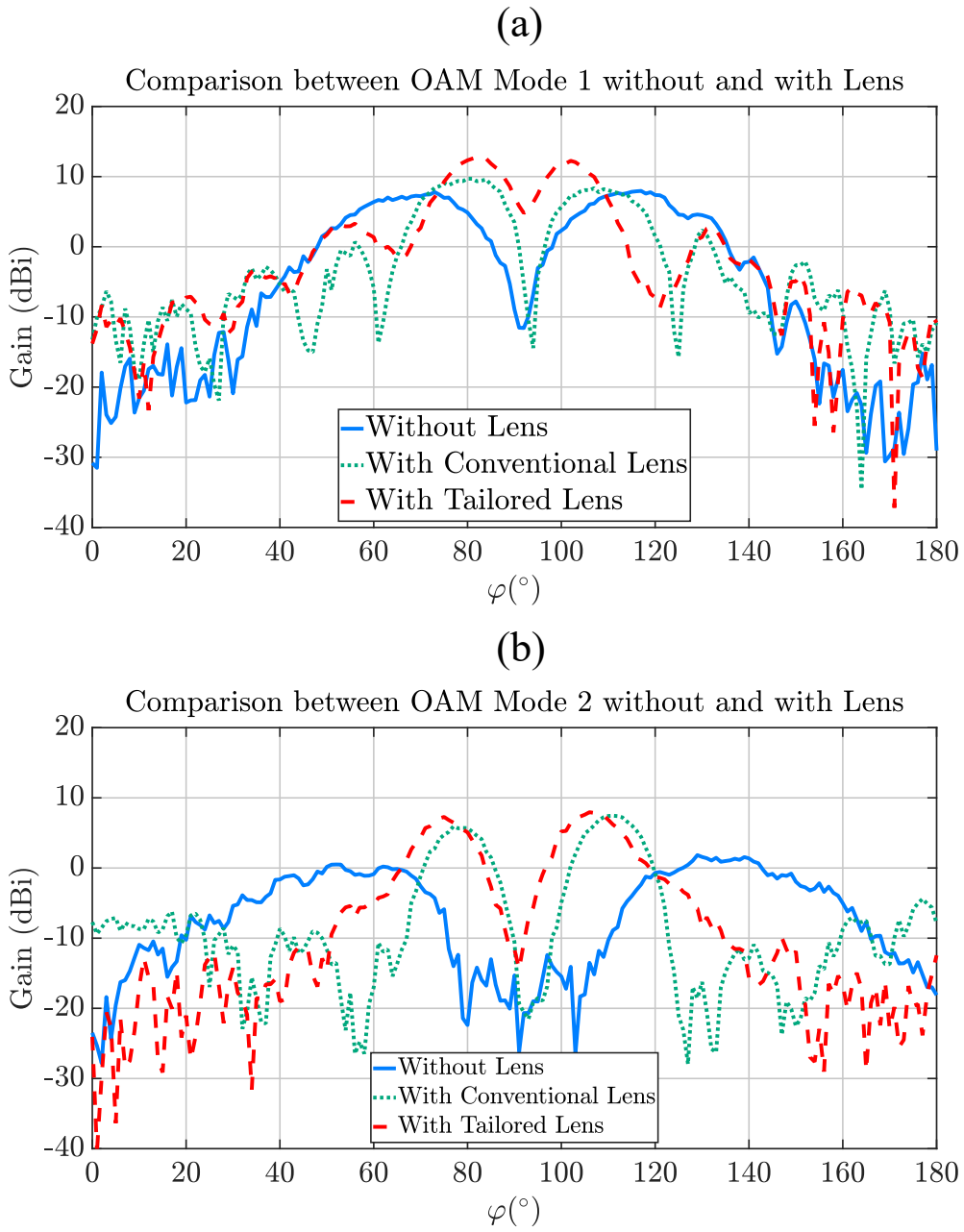

Figure 5.7: Comparison between the measured gain of the UCA at $\vartheta = 0°$ (H-plane) without lens, with conventional lens, and with tailored lens for the OAM mode order 1 (a), and 2 (b).

5.2 Divergence Reduction with Conventional and Tailored Reflector

After the successful application of the tailored lens concept (simulation and measurement), it is now the time to move on to the same idea but concerning the reflector. Where it shows an advantage of lower weight and can be produced with very large shapes.

5.2.1 Reflector Evaluation Including OAM Impressed Field Source

Just like the lens, the Fermat principle allows a conventional reflector to be configured for a point source identified by $r(\vartheta)$ as a function of n_1 and r_0. $r(\vartheta)$ refers to the radius of the reflector suspended on the polar angle ϑ. On the other hand, r_0 is the radius at $\vartheta = 0°$, while the refractive index of the air n_1 denotes the value of 1.

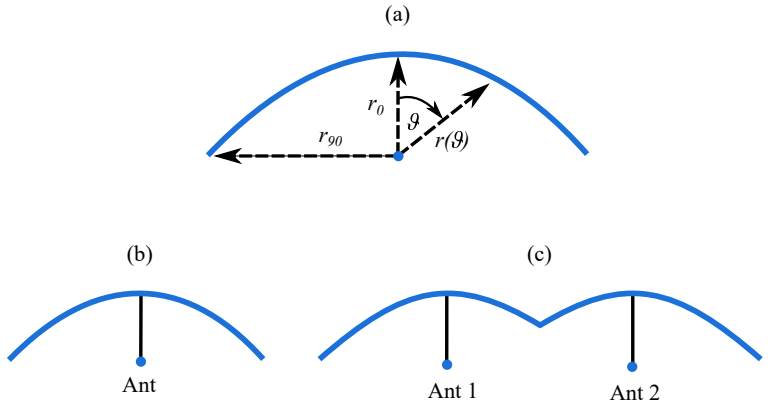

Figure 5.8: Reflector for a point source (a), extension to conventional reflector (b), and extension to tailored reflector (c).

$$r(\vartheta) = \left(\frac{2r_0}{n_1(1 + \cos(\vartheta))} \right). \tag{5.8}$$

The tailored reflector is designed by sweeping the shape function which has been shifted to align the center of the patch antenna around the z-axis (5.8), as displayed in Fig. 5.8 (a, and c). The two reflectors hang on two parameters, namely the angle ϑ and the radius r. To be more precise, when the r and ϑ (from $-90°$ till $90°$) become higher, the gain increases. As a consequence, the divergence of the vortex waves decreases due to the increased focusing of the radiation pattern. The tailored reflector is compared to the UCA without reflector and with conventional one. The gain of the two reflectors is illustrated in Fig. 5.9 (a) announcing that superior performance

Table 5.1: The opening angle for the maximum simulated gain of each reflectors ($\lambda_0 = 30mm$ at 10 GHz) for the OAM mode order -1.

r_0 (mm)	Opening angle (°) (Conventional reflector)	Opening angle (°) (Tailored reflector)
30	155	168
32	156	169
34	157	170
42	161	171
50	164	172
59	166	173
72	169	174
100	172	175
113	173	176

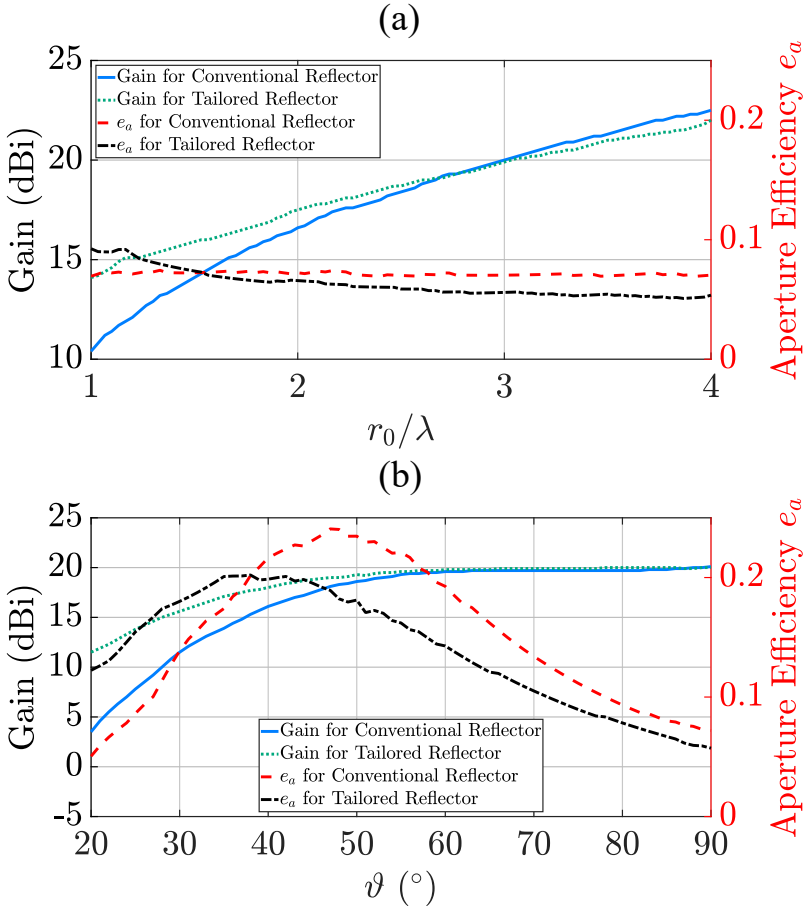

Figure 5.9: The simulated gain (dBi) for the OAM mode order -1 depending on the height r_0 of the reflector (a), and on the angle ϑ (b) with a fixed height r_0 of 90 mm using an OAM impressed field source with conventional reflector and with tailored reflector, and the aperture efficiency e_a of the two reflectors.

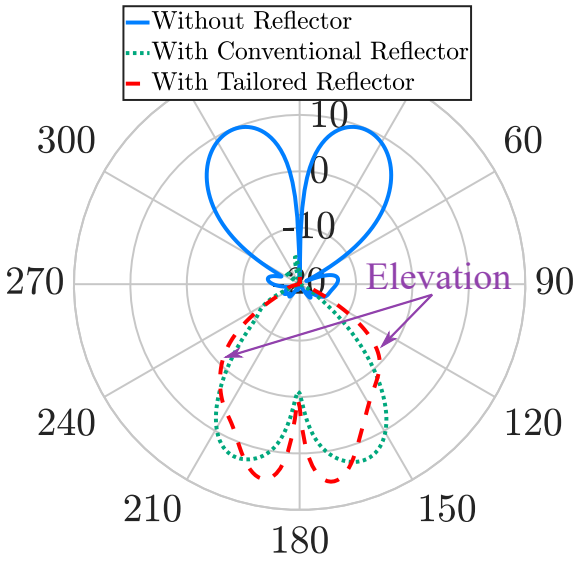

Figure 5.10: The simulated radiation pattern (dBi) using an OAM impressed field source for the OAM mode order -1 with r_0 of $40\,\mathrm{mm}$ and with an angle ϑ from $-90°$ till $90°$ without reflector, with conventional reflector and with tailored reflector.

is achieved by the tailored reflector instead of the conventional reflector in particular with the height of 1.5λ. Nevertheless, there is not a large difference between the two reflectors beyond 1.5λ, in which the tailored reflector still provides a higher reduction in the divergence because the maximum gain is much closer to the broadside radiation (cf. table 5.1). Therefore, these gain results are obtained without the effects of the ground plane which causes some reflections and diffractions of the reflector radiation thus resulting slight deviations in the comparison between the two reflectors. In Fig. 5.9 (b), the two reflectors are compared as a function of angle ϑ, where the tailored reflector shows better performance until the angle reaches $\vartheta = 38°$ is achieved. In Fig. 5.10, by the use of an OAM impressed field source the simulated radiation pattern at $\varphi = 0°$ (H-plane) without reflector, with conventional reflector and with tailored reflector are displayed separately for a height of $40\,\mathrm{mm}$ and an angle ϑ from $-90°$ to $90°$. The divergence of the two reflectors is minimized from about $9.5\,\mathrm{dBi}$ at angle $336°$ to $13.2\,\mathrm{dBi}$ at angle $160°$ (conventional) and to $15.4\,\mathrm{dBi}$ at angle $170°$ (tailored). Regretfully, due to the cut of the reflector in the middle a specific elevation of pattern for the case of tailored reflector is created, which causes some rays to propagate into the second section of the reflector whereby unwanted reflections can appear. Whenever the height of the UCA r_0 is lower or the radius is larger, a decrease in this broadening is allowed. The instantaneous electric field and the helical phase front of the three cases are illustrated in Figs. 5.11 and 5.12. Generally, after the reflection with the reflectors the order of the OAM mode is reverted, namely $+1$ instead of -1.

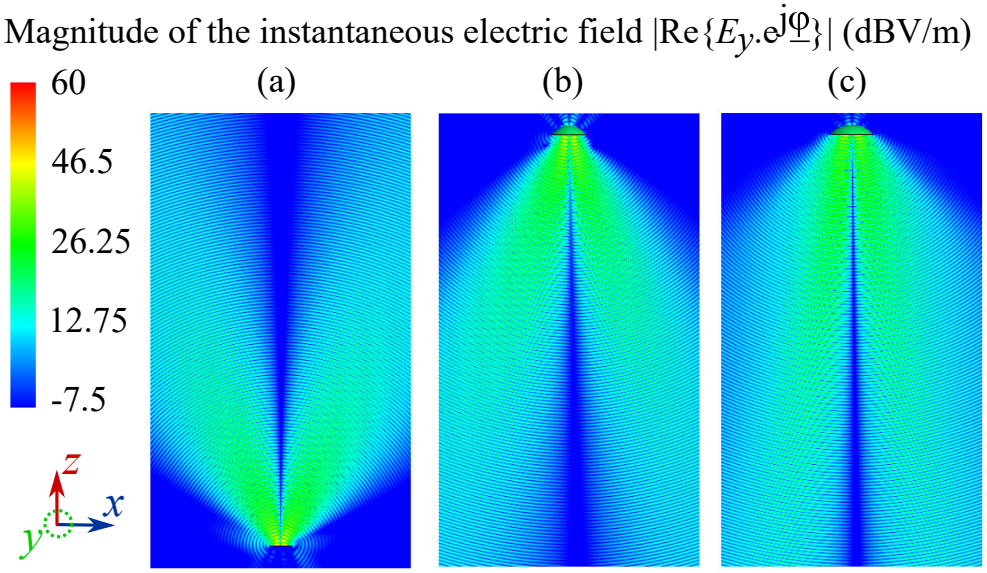

Figure 5.11: The simulated magnitude of the instantaneous electric field using an OAM impressed field source for the OAM mode order -1 with r_0 of $40\,\mathrm{mm}$ and with an angle ϑ from $-90°$ till $90°$ without reflector (a), with conventional reflector (b) and with tailored reflector (c).

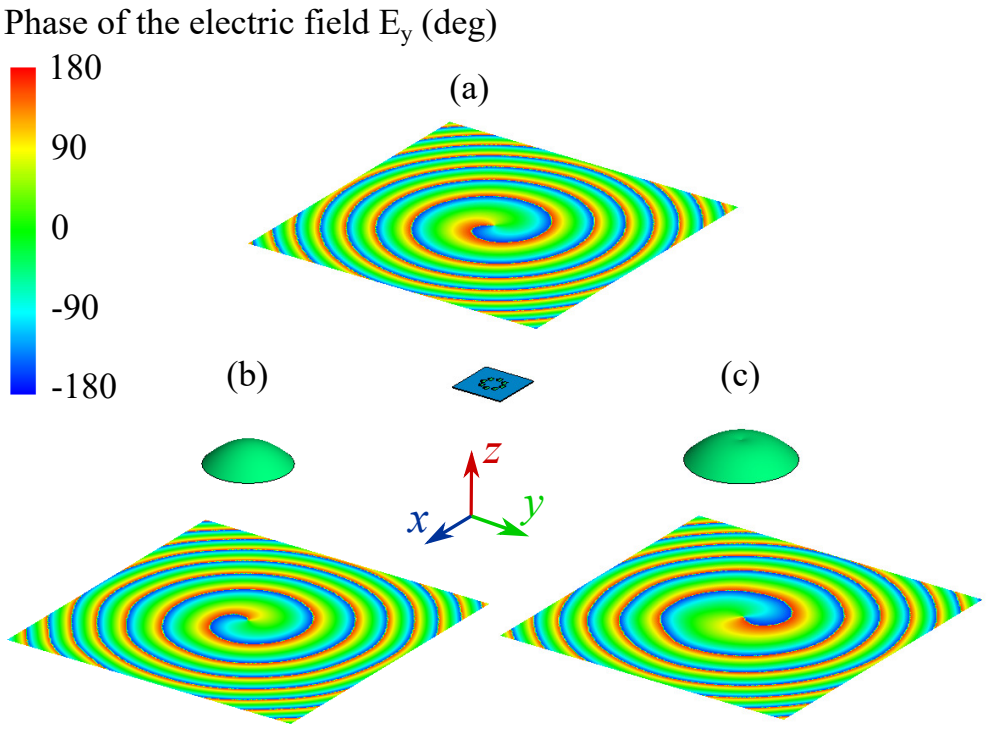

Figure 5.12: The simulated phase distribution of E_y using an OAM impressed field source for the OAM mode order -1 (from $x = -300$ till $300\,\mathrm{mm}$, from $y = -300$ till $300\,\mathrm{mm}$, $z = 300\,\mathrm{mm}$ for (a) and $z = -300\,\mathrm{mm}$ for (b, and c)) indicating the phase distribution of OAM impressed field source with r_0 of $40\,\mathrm{mm}$ and with an angle ϑ from $-90°$ till $90°$ without reflector (a), with conventional reflector (b) and with tailored reflector (c).

5.2.2 Reflector Evaluation Including Realistic Feeding Antenna Structure

To facilitate the interpretation of the reflector's behavior, the previous section presents the three scenarios using an OAM impressed field source. Whereas in this section, the reflectors are simulated with a realistic UCA assembled on three differently shaped ground planes. The first shape is a circular PCB having a diameter of $60\,\mathrm{mm}$, while the second and the third shapes composed of a rectangular PCB with a footprint of $60\,\mathrm{mm} \times 60\,\mathrm{mm}$ and $100\,\mathrm{mm} \times 100\,\mathrm{mm}$, respectively. The gain according to the height r_0 in an angle ϑ varying from $-90°$ till $90°$ is determined in Fig. 5.13 (a, b, and c), where the gain oscillation is effected by the ground plane as a consequence of the standing waves between the UCA and the reflector. The gain of the conventional reflector is manipulated through the three differently shaped ground planes more

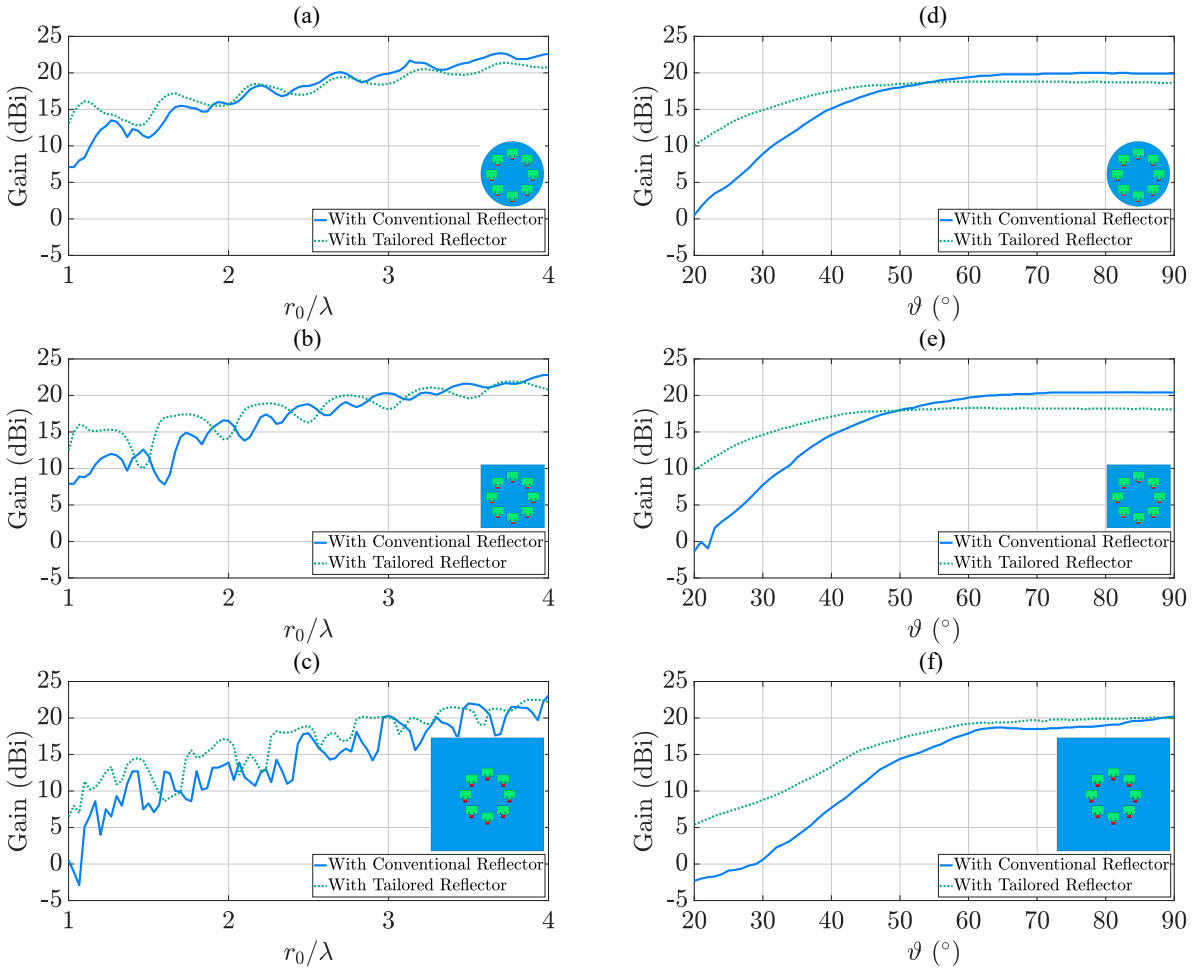

Figure 5.13: The simulated gain (dBi) of the realistic UCA for the OAM mode order -1 depending on the height r_0 (a, b, and c) and the angle ϑ (d, e, and f) of the reflector in a $60\,\mathrm{mm}$ diameter circular ground plane (a, and d), in a $60\,\mathrm{mm} \times 60\,\mathrm{mm}$ rectangular ground plane (b, and e) and in a $100\,\mathrm{mm} \times 100\,\mathrm{mm}$ rectangular ground plane (c, and f).

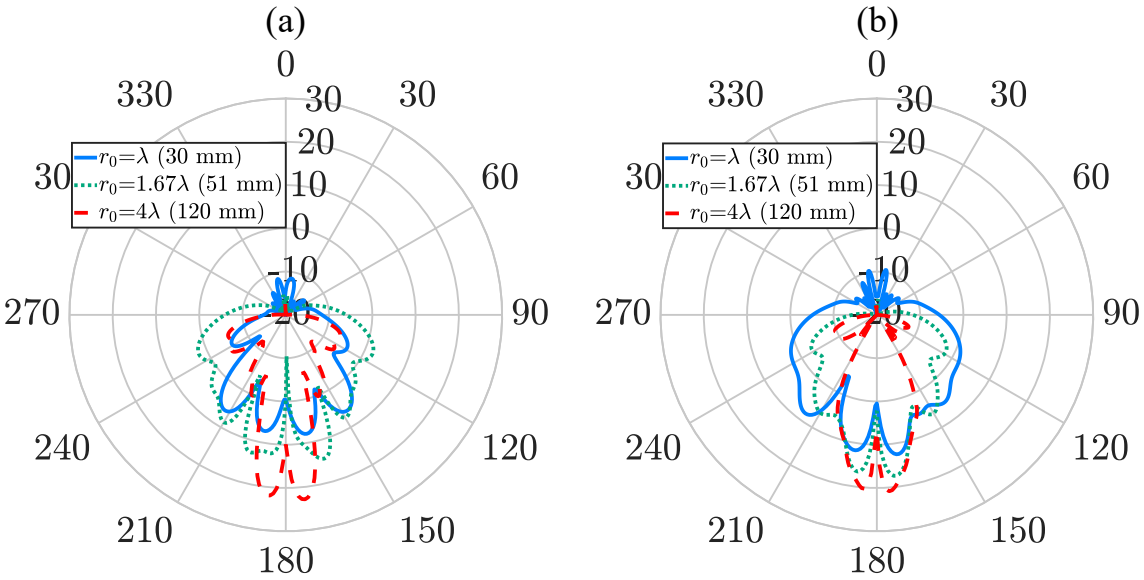

Figure 5.14: The simulated radiation pattern (dBi) with realistic UCA for the OAM mode order -1 of conventional (a) and tailored reflector (b) of UCA with a rectangular shaped PCB $60\,\mathrm{mm} \times 60\,\mathrm{mm}$ for several height r_0 of $30\,\mathrm{mm}$, $51\,\mathrm{mm}$, and $120\,\mathrm{mm}$.

than the tailored one. The gain depending on the angle ϑ with a height r_0 of $90\,\mathrm{mm}$ is displayed in Fig. 5.13 (d, e, and f). The circular ground plane shape has minimal impact on the gain of the reflectors, which gives it priority for the reflectors. The radiation pattern for the OAM mode order -1 of the two reflectors in 2D at $\varphi = 0°$ (H-plane) for heights r_0 of $30\,\mathrm{mm}$, $51\,\mathrm{mm}$, and $120\,\mathrm{mm}$ is shown in Figs. 5.14 (a) and 5.14 (b). As illustrated, in contrast to the conventional reflector the tailored reflector executes well from the height r_0 of λ, which shows a nice OAM beam from the height r_0 of 1.67λ. The instantaneous electric field and the phase distribution of the $(60\,\mathrm{mm} \times 60\,\mathrm{mm})$ rectangular shaped UCA for the OAM mode order -1 with $40\,\mathrm{mm}$ height r_0 and with an angle ϑ from $-90°$ till $90°$ are presented in Figs. 5.15 and 5.16. The helicity of the phase front is preserved, however with switched OAM mode order's sign, namely from the mode -1 to the mode 1, and with increased distortion for the conventional reflector. With a height of $90\,\mathrm{mm}$ and an angle ϑ of $45°$, the radiation pattern of the OAM mode orders 0, -1 and -2 is demonstrated in Fig. 5.17. The tailored reflector enhances the gain for the zeroth mode order from $13.9\,\mathrm{dBi}$ to $19.6\,\mathrm{dBi}$ contrary to the conventional reflector which reduces the gain till $10.3\,\mathrm{dBi}$. In comparison to the tailored lens, this is considered to be a similar behavior to that of the conventional lens. The gain of the conventional and tailored reflector is raised from about $9.5\,\mathrm{dBi}$ till $16.5\,\mathrm{dBi}$ and $17.8\,\mathrm{dBi}$ with regard to the first OAM mode order, respectively. The tailored reflector provides $1.3\,\mathrm{dBi}$ further than the conventional reflector. Whereas, the gain of the conventional and the tailored reflector for the second OAM mode order is enhanced from

6.3 dBi till 10.4 dBi and 13.9 dBi, respectively. By increasing the order of the mode, the gain decreases as a result of the raised divergence. The tailored reflector provides an advantage of reduction of material consumption similar to the tailored lens, particularly with larger UCA radii where additional antenna elements are utilized. Due to the limitation of production and equipment, a reflector with a height of 90 mm and an angle of 45° are manufactured.

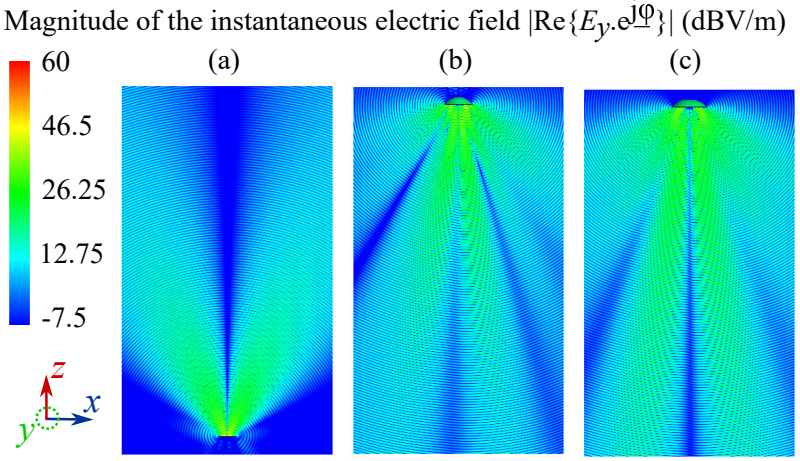

Figure 5.15: The simulated magnitude of the instantaneous electric field with realistic UCA for the OAM mode order -1 of the circular antenna array with rectangular shaped PCB 60 mm × 60 mm without reflector (a), with conventional reflector (b), and with tailored reflector (c).

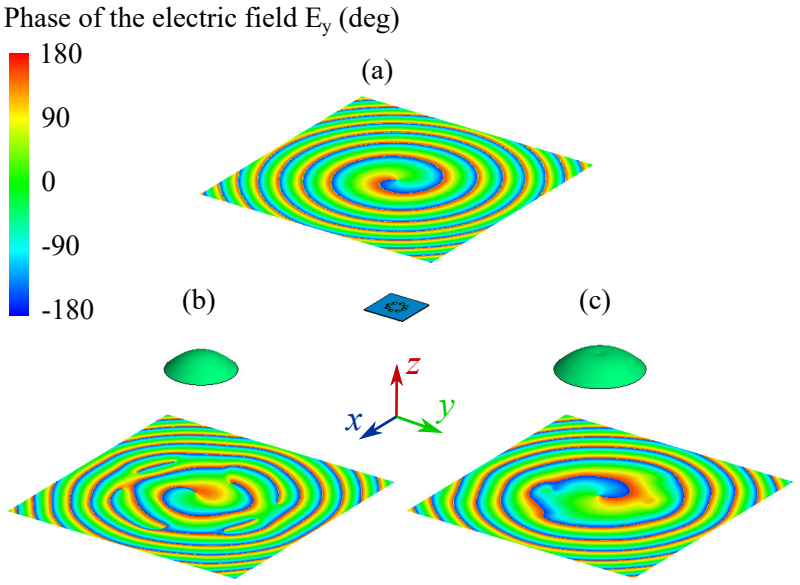

Figure 5.16: The simulated phase distribution of E_y with realistic UCA for the OAM mode order -1 with rectangular shaped PCB 60 mm × 60 mm (from $x = -300$ till 300 mm, from $y = -300$ till 300 mm, $z = 300$ mm for (a) and $z = -300$ mm for (b, and c)) indicating the helical phase distribution of circular antenna array without and with reflector.

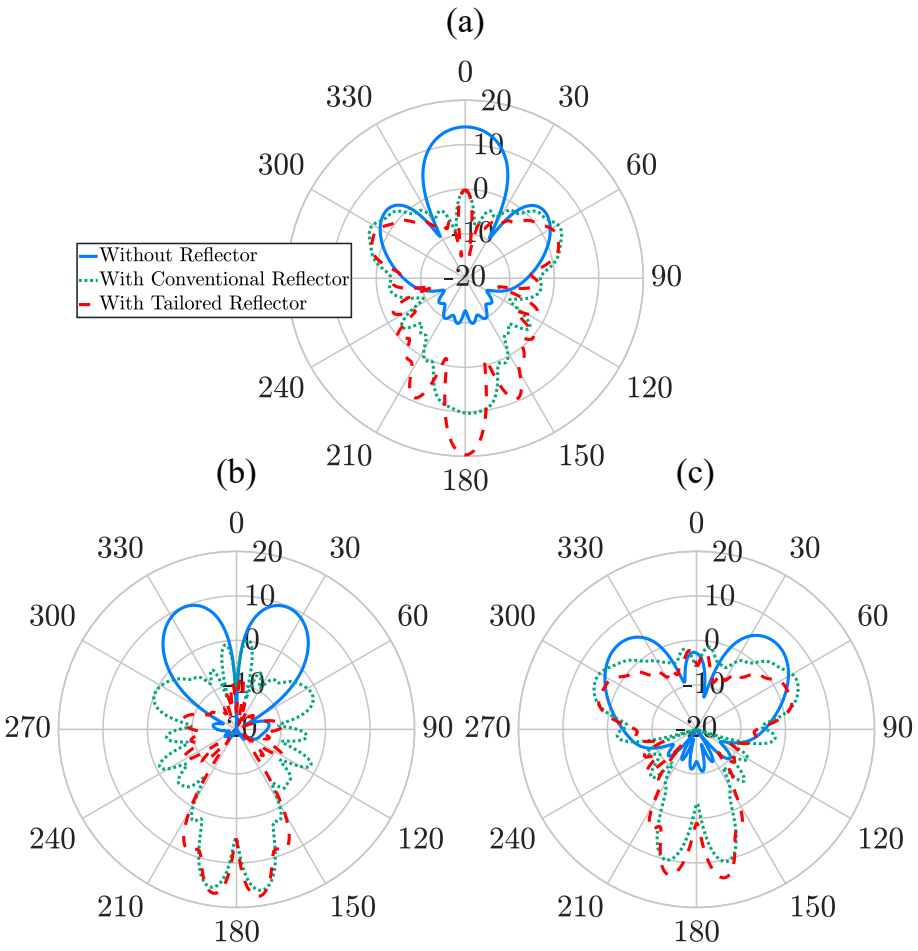

Figure 5.17: The simulated radiation pattern (dBi) with realistic UCA for the three cases for the OAM mode order 0 (a), -1 (b), and -2 (c) at $\varphi = 0°$ (H-plane) with a height of $90\,\mathrm{mm}$ and an angle of $45°$.

5.2.3 Experimental Verification

As well as the lens, in order to be measured in the anechoic chamber above a rotating stage a conventional reflector and a tailored reflector with a height of $90\,\mathrm{mm}$ and an opening angle ϑ of $45°$ are printed with a 3D printer machine. The reflectors are manufactured from polypropylene (PP) which have been covered with aluminium foil to act like a reflector. Fig. 5.18 shows the reflector assembled with the UCA and with the BM. The beam divergence of the OAM mode order 1 is clearly decreased in Fig. 5.19. The tailored reflector provides $12\,\mathrm{dB}$ as measured and $17.8\,\mathrm{dB}$ as simulated. While in Fig. 5.20 (a), $10.5\,\mathrm{dB}$ measured gain and $16.5\,\mathrm{dB}$ simulated one are published with the conventional one. As noted above, there is a difference between the simulated and measured values based on the proceeding mentioned issues. First of all, due to the 3D printing process the reflectors are not quite smooth. Secondly, the aluminium layers

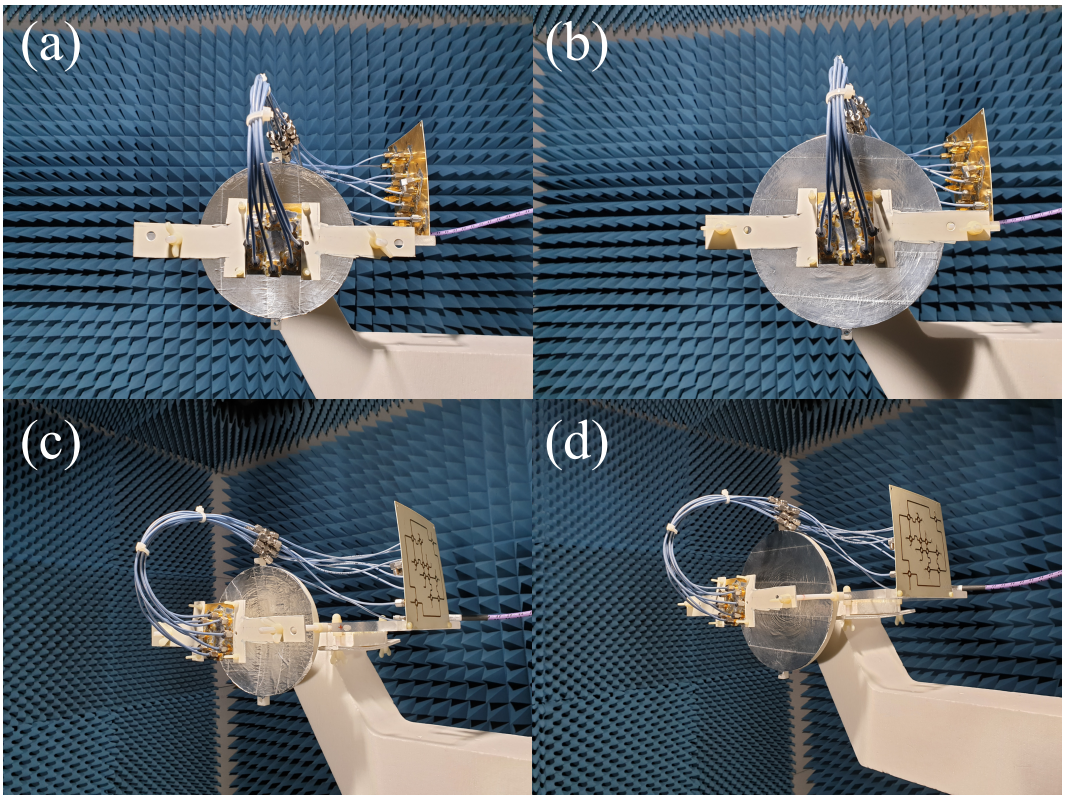

Figure 5.18: The manufactured conventional reflector (a, and c), and tailored reflector (b, and d).

are not perfectly bonded to the UCA, and the antennas are attached with a plastic patch that establishes a certain absorption and delay of the reflected vortex waves. Therefore, the UCA and the reflector are not perfectly aligned. Furthermore, the antennas are equipped with eight coaxial cables which can disturb the path of the vortex waves. To avoid such issues, the BM or the power divider (PD) [77] can be integrated into the ground plane, otherwise two reflectors (primary and secondary) such as the Cassegrain reflector can be used. The phase distribution of the three scenarios, which show a distinct helical phase distribution of the first OAM mode order are also depicted in the figure 5.19. Note that the purpose is the helical phase distribution in the doughnut radiation pattern and not outside. Fig. 5.20 reveals the gain for the OAM mode order 1 and 2 at $\varphi = 0°$ (H-plane). The measured gain of OAM mode order 2 ($7.7\,\mathrm{dBi}$) manages a gain enhancement of $4.5\,\mathrm{dB}$ and $3.1\,\mathrm{dB}$ in comparison to the UCA without reflector and with conventional reflector, respectively (cf. Fig. 5.20 (b)).

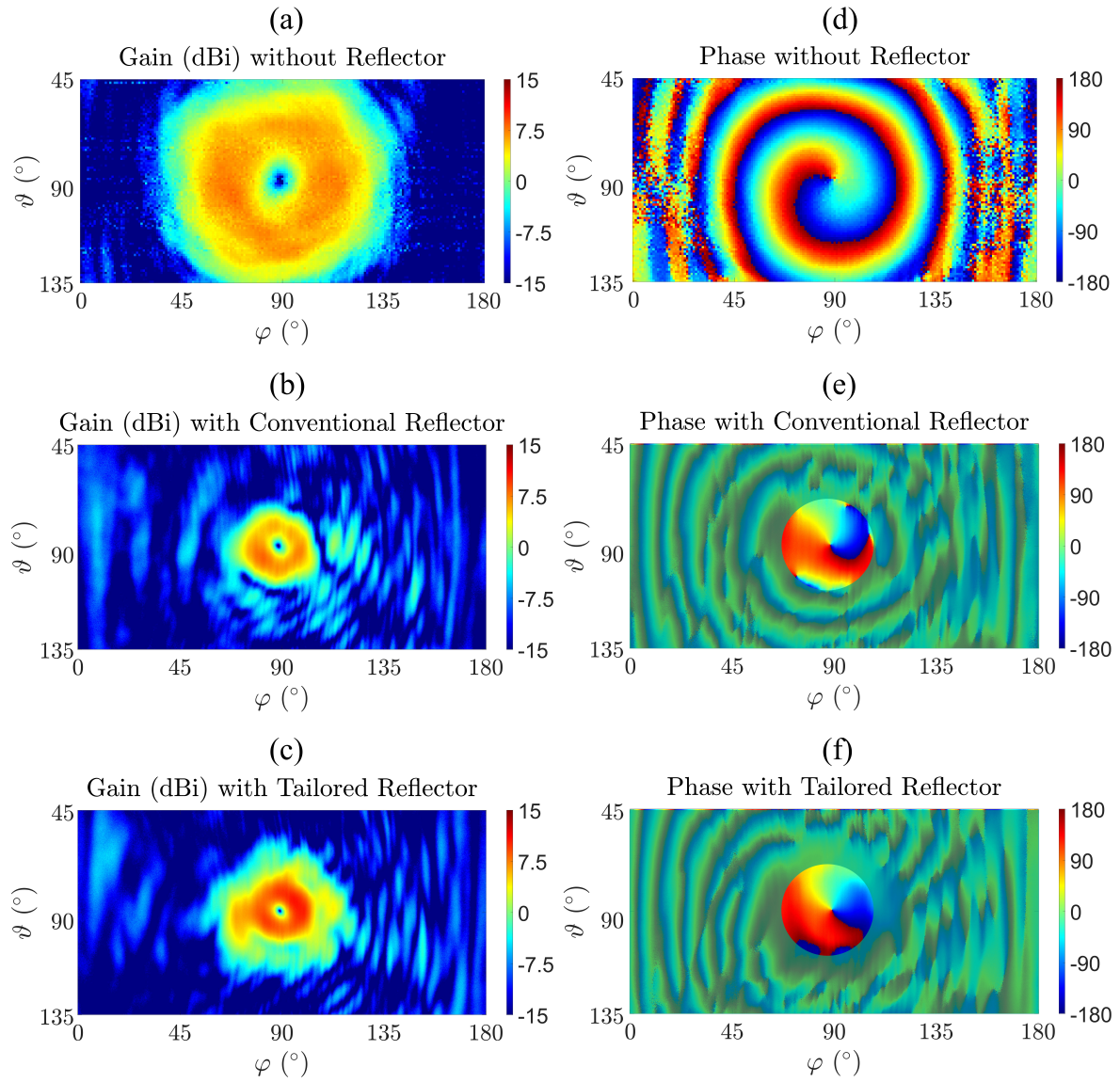

Figure 5.19: The measured gain (dBi) and the measured phase distribution of antennas for the OAM mode order 1 without reflector (a, and d), with conventional reflector (b, and e), and with tailored reflector (c, and f) with rectangular ground plane shape $60\,\mathrm{mm} \times 60\,\mathrm{mm}$ (height of $90\,\mathrm{mm}$ and angle of $45°$).

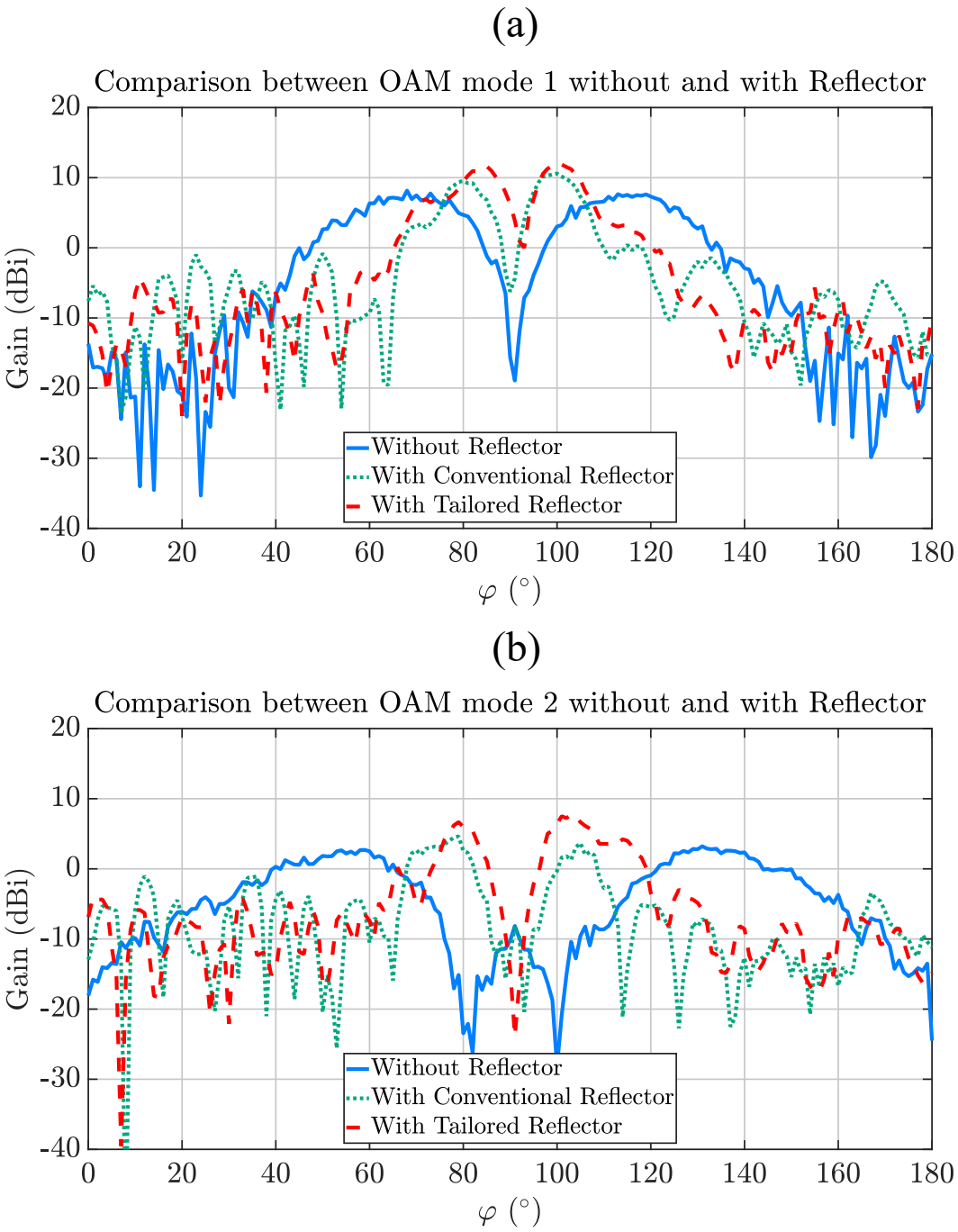

Figure 5.20: The measured gain comparison between UCA without reflector, with conventional reflector, and with tailored reflector with rectangular ground plane shape $60\,\mathrm{mm} \times 60\,\mathrm{mm}$ (height of $90\,\mathrm{mm}$ and angle of $45°$) at $\varphi = 0°$ (H-plane) for the OAM mode order 1 (a), and 2 (b).

5.3 Conclusion

This chapter deals with the reduction of the large beam divergence inherent to vortex waves. So, a new type of lens and reflector are modeled to solve this issue which is critical for some OAM applications. The tailored lens is evaluated and compared with the cases including and excluding conventional lens, where the tailored lens exhibits better performance. Similarly, the tailored reflector demonstrates the same behavior when compared to the cases incorporating and omitting conventional reflector. Furthermore, the two tailored components have a particular superior advantage over the others by saving on material consumption if higher OAM mode order are applied, where the radius of the antenna array have to be increased. To conclude, this chapter demonstrates that the vortex waves require a special lens or a special reflector to reduce the beam divergence effectively as a function of all OAM mode orders.

Chapter 6

Mode Order Conversion and Clutter Rejection with OAM

In the earlier chapter, the issue concerning the OAM beam divergence inherent to OAM waves is discussed and solved seperately with the aid of two approahces, namely with the help of a tailored lens and a tailored reflector. Both reveal a better achievement when compared to the conventional ones. Once the problem of the misalignment and the divergence of the OAM beam has been solved, this chapter covers the RFID application which uses dielectric resonators. The RFID application struggles with the limited number of coded tags and with the clutter, which has negative impact. The vortex waves therefore offer a solution to these issues. At first, a cylindrical dielectric resonator is designed and extended to form a helically arranged cylindrical dielectric resonator array to radiate OAM waves and to convert the incident OAM mode order[1]. Secondly, several helical arrangements are joined together to increase the RFID codes. After that, a simulation and experimental verification exhibit the rejection of clutter provided from the environment. Finally, the last section concludes this chapter.

6.1 Modeling of Dielectric Resonator (DR)

With the aid of the MoM-solver FEKO, a cylindrical dielectric resonator reacts and resonates when it is illuminated by incident plane waves. Three groups of modes (Transverse Electric (TE), Transverse Magnetic (TM) and hybrid modes (HE)) are supported by this DR, whose corresponding quality factor and operation frequency depend mainly on the size, on the ori-

[1] Parts of this chapter have been published in [78], and [79]

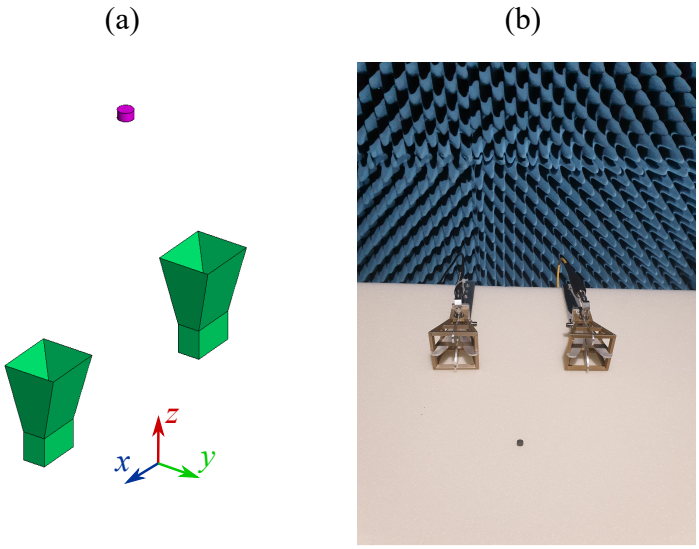

Figure 6.1: The simulation setup of the cylindrical DR (a), the measurement setup of the cylindrical DR in an anechoic chamber (b).

entation, on the relative permittivity ε_r, and on the loss tangent (tanδ) of the DR. To be more precise, with a $3.2\,\mathrm{mm}$ radius, a $3\,\mathrm{mm}$ height and a relative permittivity $\varepsilon_r = 37$ (ceramic), the $10\,\mathrm{GHz}$ operated DR radiates with the mode HE_{11}. In Fig. 6.1 (a, and b), the simulated and measured setups are illustrated, whereby the two horn antennas are separated from each other by about $100\,\mathrm{mm}$ and are equidistant from the dielectric resonator. In Fig. 6.2, within $9.6\,\mathrm{GHz}$ and $10.4\,\mathrm{GHz}$, the simulated and the measured insertion loss S_{21} of the two horn antennas are presented with and without the DR. Consequently, an increased S_{21} of about $5\,\mathrm{dB}$ occurs in particular between $10\,\mathrm{GHz}$ and $10.3\,\mathrm{GHz}$ indicating the attendance of the DR. The measured S_{21} reveals a very good agreement with the full-wave MoM simulation calculated by Feko.

6.2 OAM Mode Order Conversion

A helically arranged cylindrical dielectric resonator array is formed to radiate vortex waves once it is illuminated by an antenna. These helically arrangement is able to radiate in two opposite directions (forward and backward) due to the asymmetric doughnut-shape radiation pattern of each DR. The transmitted OAM mode order from the source towards the helically arrangement m_{in} (incident mode) has the same OAM mode order of the forwarded transmitted OAM mode from the arrangement. Whereas, the backward reflected OAM mode order towards the source m_{out} has a different OAM mode order than the incident one, which depends on the incident OAM mode order m_{in}, the DR quantity and the OAM mode order m_{DR} of the helically arrangement.

In order to radiate the OAM waves, the essential phase shift between each pair of the azimuthally adjacent DRs in order to radiate the OAM waves is defined by the following equation:

$$\Delta\varphi = \frac{2\pi m}{N}, \tag{6.1}$$

where N denotes the number of the DRs, and m is the order of the vortex waves. Hence, the height h between each azimuthally adjacent DR is determined by

$$h = \frac{m\lambda}{2N}, \tag{6.2}$$

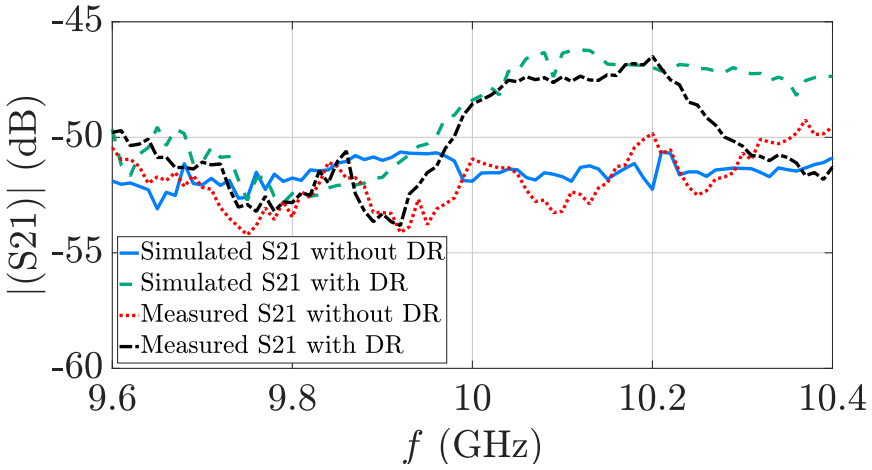

Figure 6.2: The simulated and measured S_{21} (dB) of two standard gain horn antennas without and with DR from 9.6 GHz till 10.4 GHz.

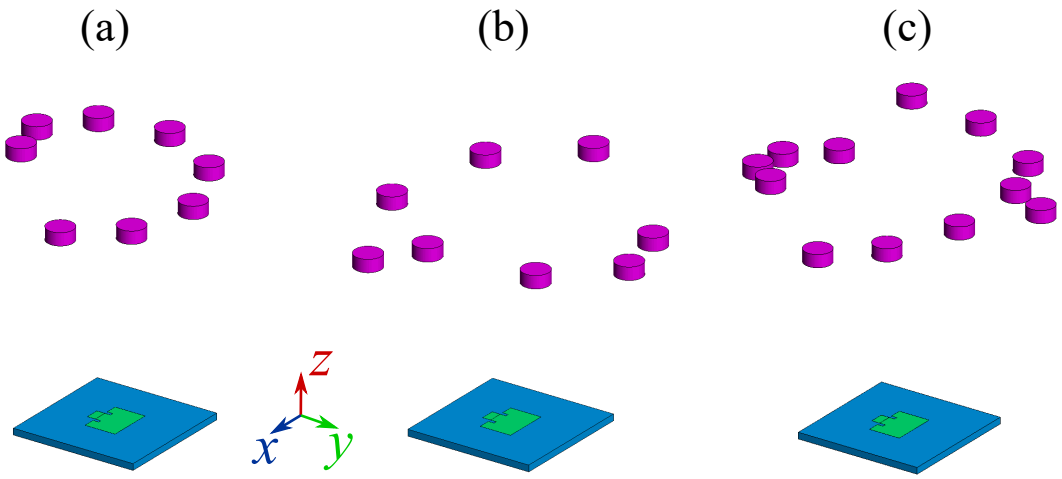

Figure 6.3: The illustration of the helically arranged DRs array for the OAM mode orders -1 (a), $+2$ (b) and -3 (c).

where λ is the wavelength in the free space. The number 2 in (6.2) belongs to the twofold path length of the electromagnetic waves. When the DRs cross the phase shift of 2π, the total height between the lowest and the highest DR (pitch p), can be shifted vertically downwards by $\lambda/2$ along the propagation-axis. Three helically arranged cylindrical DRs array with the OAM mode orders -1, $+2$, and -3 are illuminated within the zeroth OAM mode order by a rectangular patch antenna operating at $10\,\mathrm{GHz}$ (c.f. Fig. 6.3 (a, b, and c)). Concerning the equation (6.2), the height h between the adjacent DRs for the OAM mode orders -1, $+2$, and -3 are $1.875\,\mathrm{mm}$, $3.75\,\mathrm{mm}$, and $5.625\,\mathrm{mm}$, respectively. Hence, the highest gain of the arrangement in the backscattered direction regarding the modes -1, $+2$ and -3 (cf. Fig. 6.4 (a)) are $-17\,\mathrm{dBi}$, $-15.2\,\mathrm{dBi}$ and $-14.3\,\mathrm{dBi}$ at $154°$, $154°$ and $219°$, respectively. The depicted radiation pattern in Fig. 6.4 (a) between the angle $90°$ and $270°$ belongs to the backward reflected OAM mode order unlike the conventional side lobes. Fig. 6.4 (b, c, and d) presents the phase front of the converted zeroth OAM mode order into the OAM mode orders of -1, 2, and -3 showing a phase distribution of one helix, two helices and three helices, respectively. Not only can the zeroth mode order be converted, but the other mode orders can be too. The conversion of vortex

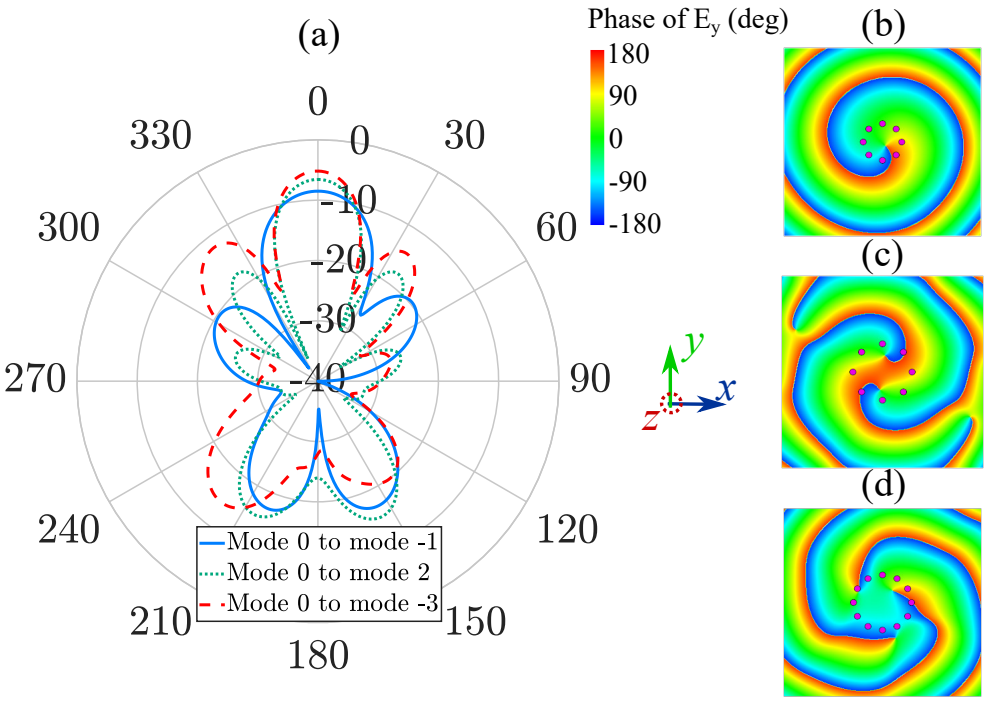

Figure 6.4: the simulated radiation pattern (dBi) in 2D at $\varphi = 0°$ (H-plane) for the OAM mode orders -1, $+2$ and -3 for $10\,\mathrm{GHz}$ (a), and the simulated phase distribution ($x = -100$ till $100\,\mathrm{mm}$, $y = -100$ till $100\,\mathrm{mm}$, $z = 200\,\mathrm{mm}$) at $10\,\mathrm{GHz}$ for the OAM mode orders -1 (b), $+2$ (c), and -3 (d).

beams from different OAM mode orders [0 (a), $+1$ (b), -1 (c), $+2$ (d), and -2 (e)] is illustrated (c.f. Fig. 6.5). A lensed patch antenna array radiates towards the structured arrangement that is constructed according to the OAM mode order $+1$. Due to the large beam divergence, a tailored lens is applied to reduce it in order to perform OAM mode conversion well. In the first case (a), the OAM mode order 0 is transmitted and converted into OAM mode -1. Whereas, the cases (b) and (c) yield an OAM mode order conversion $+1$ into the mode order -2 and -1 into 0. As well as, the cases (d) and (e) characterized by the OAM modes orders $+2$ and -2 are transmitted to be converted into the OAM mode orders -3 and $+1$, respectively. Consequently, the converted mode order m_{out} is equal to the opposite sign of the sum of the incident OAM mode order m_{in} and the OAM mode order of the helically arrangement m_{DR}.

$$m_{out} = -(m_{in} + m_{DR}). \tag{6.3}$$

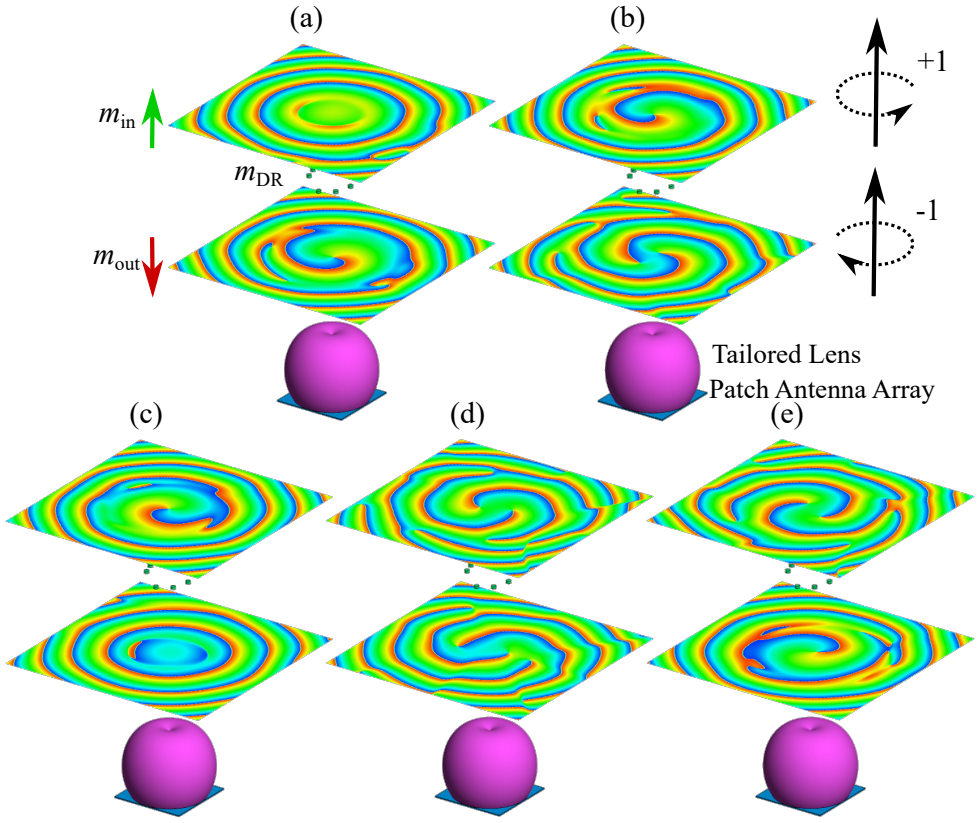

Figure 6.5: The different simulated scenarios for the OAM mode order conversion at an OAM coded tag with $m_{DR} = +1$ from the incident OAM mode order m_{in} to the reflected OAM mode order m_{out} showing reflected and transmitted beams only: 0 to -1 (a), $+1$ to -2 (b), -1 to 0 (c), $+2$ to -3 (d), and -2 to $+1$ (distorted) (e).

6.3 RFID Codes Enhancement with OAM

The OAM mode order conversion provides a new area of development in terms of the RFID application. The concept of the conventional RFID application is structured on the DR illumination within plane waves where the backscattered signal contains information as a sensed value or frequency identification. The absence and the presence of the DR guides to understand the value of 0 and 1, respectively. Through the usage of N different DR elements assembled in one RFID-tag, the codes number increases to 2^N where every DR has a different frequency. Nevertheless, due to the high request of tagged items which are greater than the limited capacity of the codes number, the researchers are motivated to find out some new improved methods so that the codes/tags number are enhanced. Indeed, the vortex waves can be one of these methods through increasing the codes number using the new degree of freedom m. Two various cylindrical DRs with two radii are separately simulated at $10\,\mathrm{GHz}$, and $11\,\mathrm{GHz}$ separately. The first one is specified with radius and height of $3.2\,\mathrm{mm}/3\,\mathrm{mm}$, whereas the second one has $2.9\,\mathrm{mm}/2.72\,\mathrm{mm}$. In Fig. 6.6, the radar cross section (RCS) of the both DRs is depicted from $9\,\mathrm{GHz}$ to $12\,\mathrm{GHz}$ yielding a maximum RCS of about $-32\,\mathrm{dBm}^2$. Besides, the coupling between the two different DRs is about $20\,\mathrm{dB}$ sufficient to minimize the interference between them. In the same way of the previous section, each DR is extended and assembled in a way to configure two helically DR arrangements establishing 2-digits OAM coded tag. The coupling and the isolation between the

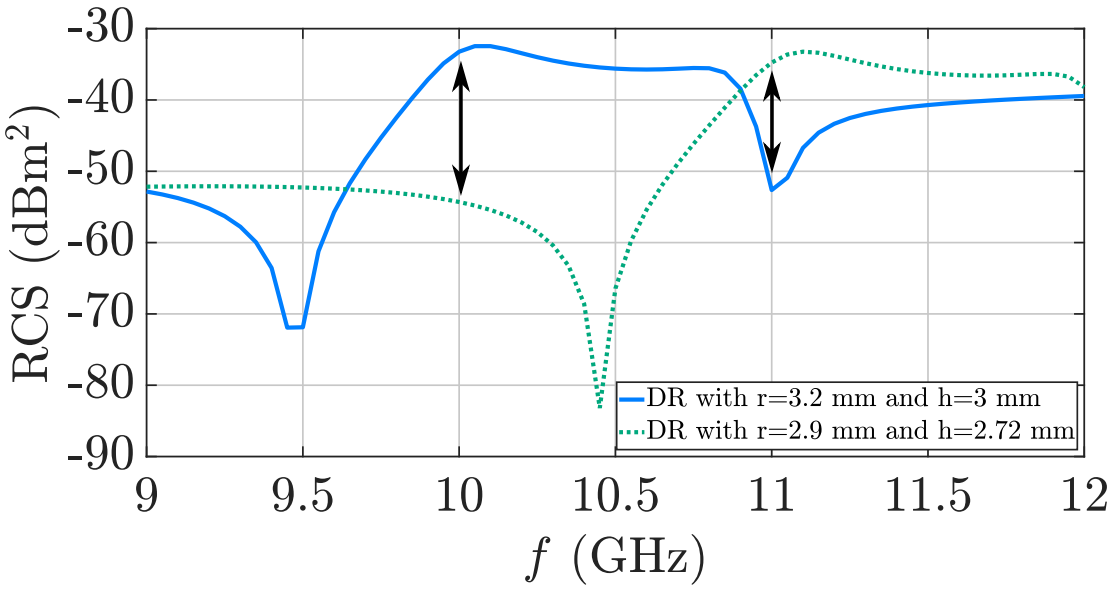

Figure 6.6: The simulated radar cross section (RCS) (dBm^2) for two different DRs with two different radii and heights from $9\,\mathrm{GHz}$ to $12\,\mathrm{GHz}$.

two arrangements can be adjusted by the help of two various radii for every helix. To be more precise, $20\,\mathrm{mm}$ and $30\,\mathrm{mm}$ radii are used for $11\,\mathrm{GHz}$, and $10\,\mathrm{GHz}$, respectively. In addition, upon using the same or closer frequencies, the concept will be disturbed where the receiver would be unable to distinguish between the codes (e.g. 12 or 21), that means that the code sequence is missing. Thus the code sequence becomes altered due to many absent codes. The maximum possible number of values per digit D (per one helically arrangement) depends on the number of the DRs N, which refers to the number of the possible mode orders. This is determined by

$$D = 2 \cdot \lfloor (\frac{N-1}{2}) \rfloor + 1. \tag{6.4}$$

Therefore, a helically arranged DR array consisting of 8 elements can offer $D = 7$ values per digit $(-3, -2, -1, 0, 1, 2, 3)$. As a consequence, the equation (6.4) gives $D^k = 49$ OAM codes with the presence of $k = 2$ and $D = 7$, where k is the number of DR helically arrangement. Whereas for a $k = 3$ and $D = 7$, the codes number will be enhanced to 343 codes, hence it is preferable to use a spherical DR because of the more equidistant resonance frequencies. The $+1$ in (6.4) takes into account the zeroth mode order, which can be achieved if the pitch is zero. The simulated radiation pattern of the 2-digits OAM coded tags {-1,1} and {-2,0} are illustrated in Figs. 6.7 (a) and 6.8 (a). While, in Figs. 6.7 (b, and c) and 6.8 (b, and c) the simulated phase distribution is presented at two different frequencies. The digit 0 refers to the zeroth OAM mode order exhibiting a constant phase distribution identical to the digit 1 in the conventional RFID tags. These two examples emphasize the RFID codes enhancement.

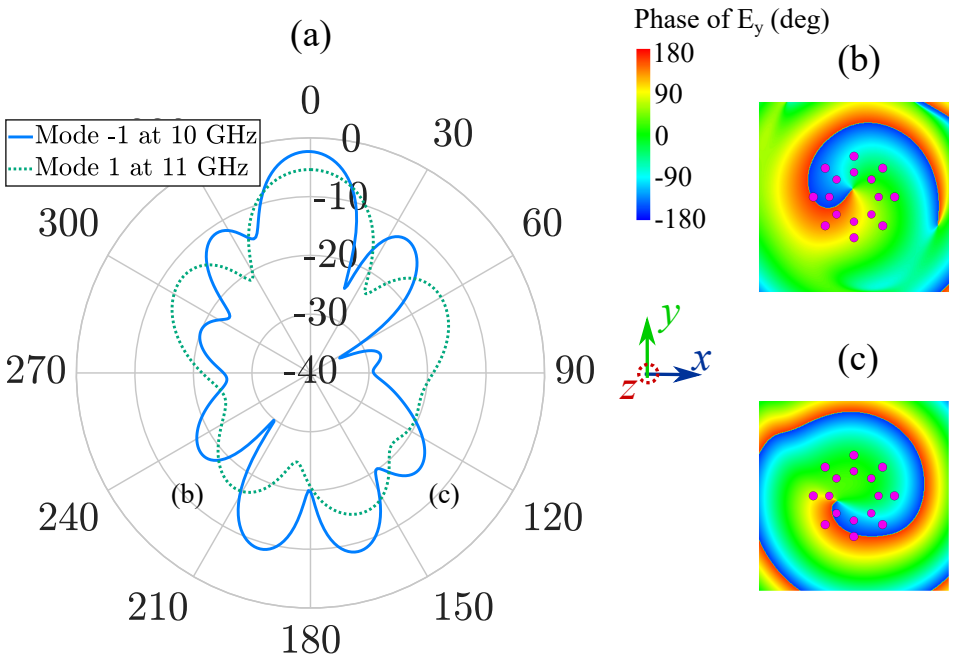

Figure 6.7: The simulated radiation pattern (dBi) in 2D at $\varphi = 0°$ (H-plane) for the 2-digits OAM coded tag {-1,1} at 10 GHz, and 11 GHz (a), and the simulated phase distribution ($x = -100$ till 100 mm, $y = -100$ till 100 mm, $z = 200$ mm) at 10 GHz for $m = -1$ (b), and 11 GHz for $m = 1$ (c).

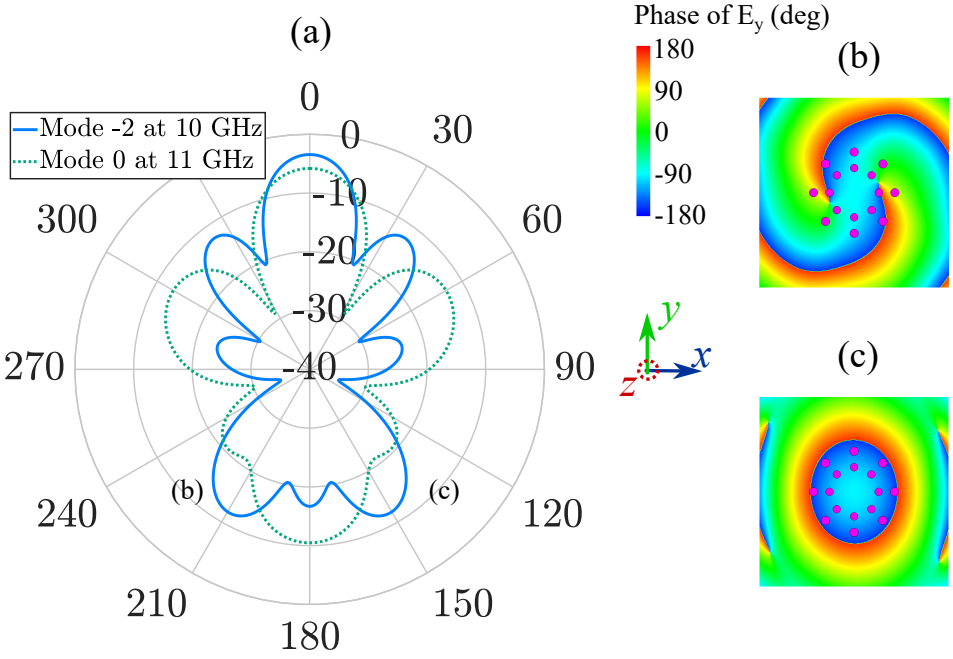

Figure 6.8: The simulated radiation pattern (dBi) in 2D at $\varphi = 0°$ (H-plane) for the 2-digits OAM coded tag {-2,0} at 10 GHz, and 11 GHz (a), and the simulated phase distribution ($x = -100$ till 100 mm, $y = -100$ till 100 mm, $z = 200$ mm) at 10 GHz for $m = -2$ (b), and 11 GHz for $m = 0$ (c).

6.4 Evaluation and Measurement of Clutter Rejection through OAM

To verify the simulation, a measurement is carried out by the aid of a vector network analyzer (VNA) ZVA 40 from Rohde & Schwarz in an anechoic chamber, where the undesirable reflections and distortions can be avoided. Before starting the measurement, the two feeding ports (coaxial cables) are calibrated between $9\,\mathrm{GHz}$ till $11\,\mathrm{GHz}$ with 201 points to obtain a characteristic impedance of $50\ \Omega$. A patch antenna (transmitter) is mounted in the middle of the UCA with a radius of about $40\,\mathrm{mm}$, which will receive the backscattered signal from the helically arranged DR array (cf. Figs. 6.9 and 6.10). The patch antenna can only transmit the zeroth OAM mode order, while the UCA (Receiver) has the ability to receive several OAM modes due to the 8×8 Butler matrix (BM) The BM operates at $10\,\mathrm{GHz}$ and is connected with the receiver by eight coaxial cables of identical length ($200\,\mathrm{mm}$). Furthermore, to prevent the undesirable distortions and side effects, the entire scheme is suspended on a large piece of Rohacell with a permittivity of almost 1 to prevent the undesirable distortions and side effects. Otherwise, the measurements would be distorted when the permittivity is higher. At first, Fig. 6.11 (a) depicts the simulated and measured S_{21} between the patch antenna and the UCA representing the mutual coupling, the reflections from the room, and the non-idealistic BM. These results are sets as reference for the next scenarios yielding a S_{21} of $-58.3\,\mathrm{dB}$ (simulation) and $-51.85\,\mathrm{dB}$ (measurement) at $10\,\mathrm{GHz}$. With the availability of the helically arranged DRs that are mounted on cylindrical Rohacell, the simulated and the measured S_{21} are depicted in Fig. 6.11 (b), where the distance between each pair of adjacent DRs is about $15\,\mathrm{mm}$ ($\lambda/2$) aiming to achieve the highest gain towards the UCA. The height h of the helically arranged DRs (8 DRs) is set according to equation

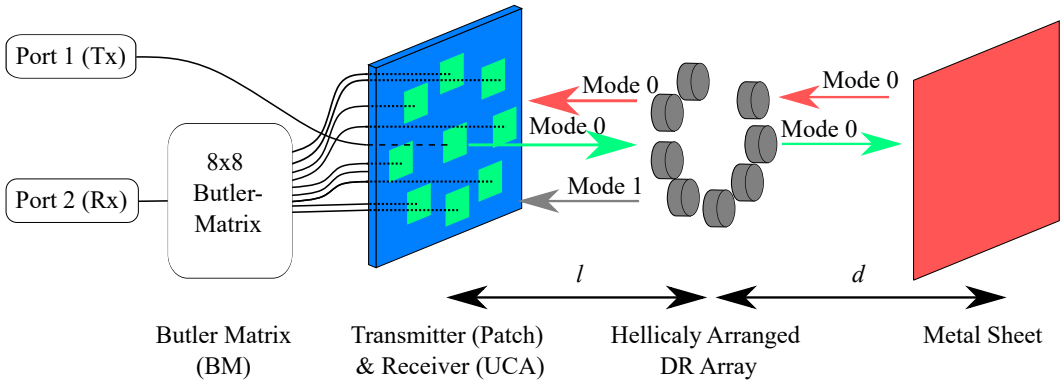

Figure 6.9: The schematic view of the measurement setup between a patch antenna, a helically arrangend DR array, and a metal sheet.

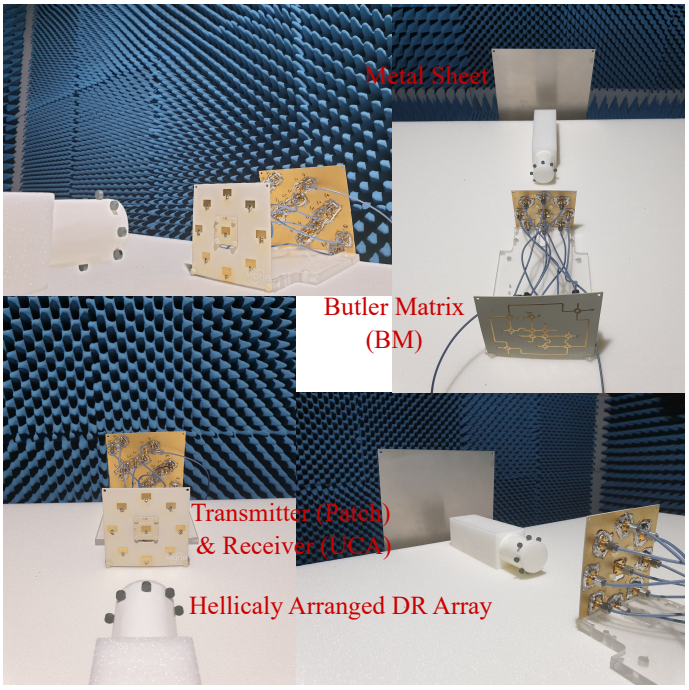

Figure 6.10: The measurement setup of patch antenna, UCA, BM and DRs in an anechoic chamber.

(6.2) in purpose to convert the zeroth OAM mode order into the first OAM mode order. As a consequence, the pitch is seven times the height h, thus its value becomes $13.125\,\mathrm{mm}$. Due to the high OAM beam divergence, the helically arrangement is separated shortly from the UCA by $l = 100\,\mathrm{mm}$. This issue concerning the beam divergence can be solved either by increasing the DRs number or through using a lens. The simulated and the measured S_{21} agree well, where a gain enhancement of about a $20\,\mathrm{dB}$ is noted by the presence of the helically arranged DR array. This gain enhancement begins from $9.6\,\mathrm{GHz}$ up to about $11\,\mathrm{GHz}$ due to the high radiation of the DRs within this bandwidth. Furthermore, a metal sheet is added to the same configuration for three different distances d of $300\,\mathrm{mm}$, $400\,\mathrm{mm}$, and $500\,\mathrm{mm}$ in order to reveal the impact as well as the distortion of that metal sheet on the transmission S_{21} (c.f. Fig. 6.11 (c, d, and e)). The S_{21} resulted at $10\,\mathrm{GHz}$ demonstrates that the metal sheet has almost no influence on the transmission with the presence of the helically arranged DRs thus announcing a new method for rejecting the clutter excluding of the zeroth mode order. Such clutter rejection appears due to the BM which makes destructive interference for the clutter, although it causes constructive interference for the DR-coded OAM-signal. The S_{21} at $10\,\mathrm{GHz}$ according to the five different scenarios are summarized in Table 6.1. Some notches in the measurement part can be noticed, particularly two fixed notches and other movable one. The two fixed notches in the measuring

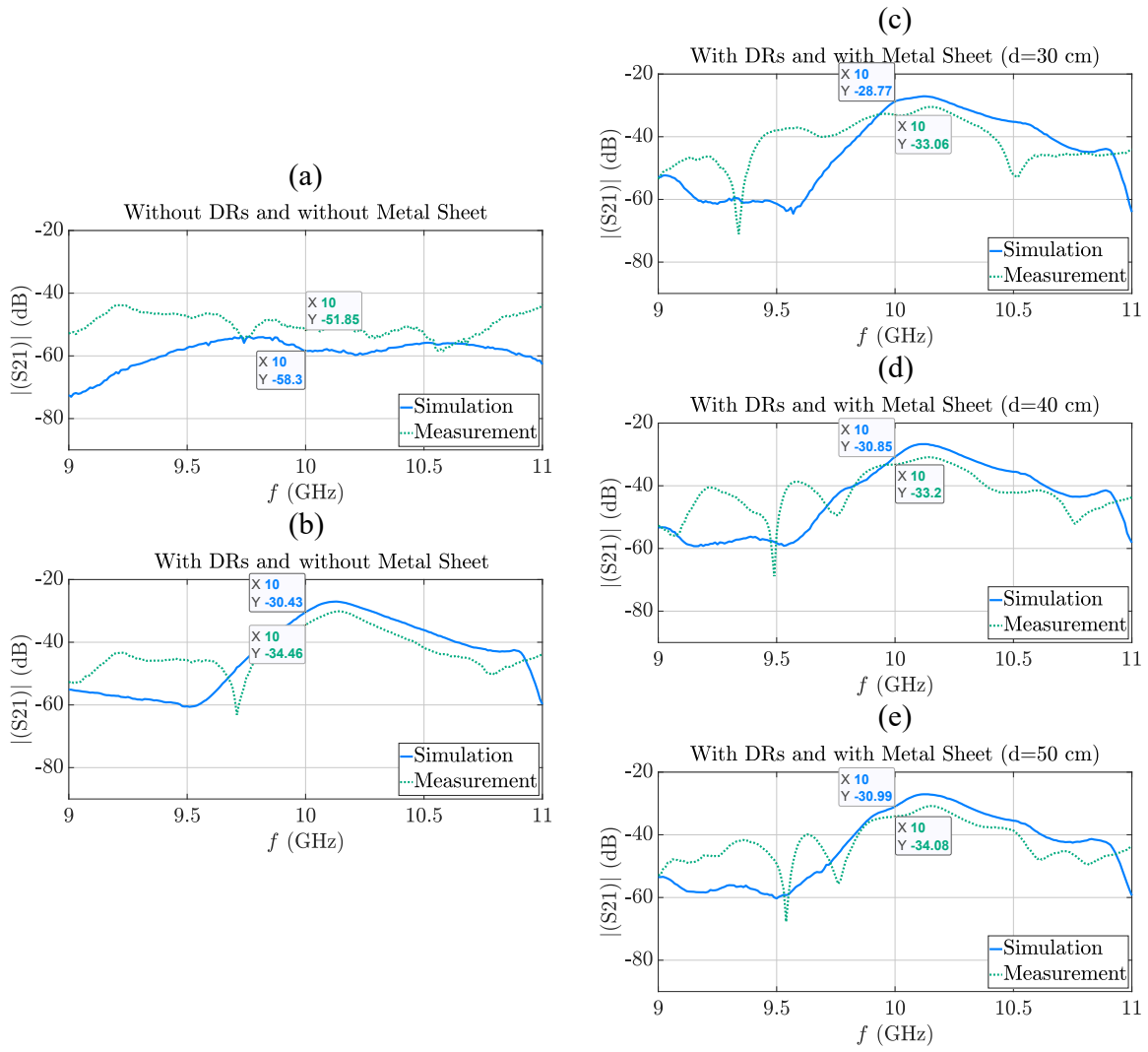

Figure 6.11: The simulated and measured S_{21} (dB) between the rectangular patch antenna and the UCA without DRs and without metal sheet (a), with DRs and without metal sheet (b), with DRs and with metal sheet for a distance d of $30\,\mathrm{cm}$ (c), $40\,\mathrm{cm}$ (d), and $50\,\mathrm{cm}$ (e).

part (about $9.7\,\mathrm{GHz}$, and $10.6\,\mathrm{GHz}$) occur due to the mutual coupling between the transmitter and the receiver (UCA). Whereas, the movable one arises as a result of the following issues. At first, the position of the patch antenna in the center of the UCA besides the height between the DRs are not very accurate. Secondly, the BM reveals a phase shift error of about $\pm 5°$. Moreover, the orientation and the distance between the DRs and the antennas have some mistakes. Finally, the metal sheet is not accurately parallel to the antennas. However, this measurement is well performed and agrees well with the simulation, resulting in the clutter rejection when the interfere is orthogonal to the direction of the main beam.

Table 6.1: The insertion loss S_{21} (dB) for the five scenarios for the first OAM mode order at 10 GHz.

		Transmission S21 (dB)	
		Sim.	Meas.
		Without DRs	
Without metal sheet		-58.3	-51.85
		With DRs	
Without metal sheet		-30.43	-34.46
With Metal Sheet	d =30 cm	-28.77	-33.06
	d =40 cm	-30.85	-33.2
	d =50 cm	-30.99	-34.08

6.5 Conclusion

In this chapter, a novel utilization of the vortex waves in the domain of RFID technology has been proposed to increase the number of RFID coded tags produced by helically arranged cylindrical dielectric resonator arrays. However, the RFID technology suffers from the distortion of the backscattered waves incoming from the environment, thus disturbing the whole RFID system, which is not the case in the presence of this helical arrangement. Moreover, the helical arrangement demonstrates the ability to convert the incident OAM mode order propagating towards the helical arrangement to a reflected OAM mode order. To summarize, this chapter has highlighted a way to develop the area of RFID through usage of the vortex waves.

Chapter 7

Conclusion and Outlook

7.1 Conclusion

The main subject of this thesis is the vortex waves where many contributions are proposed and studied to solve its issues (beam divergence and misalignment). Also, some new proposed techniques show advantages for many applications such as wireless communication, imaging, target localization. Chapter 2 focuses on the theory and the fundamentals of antennas, phased antenna arrays, lenses, reflectors, dielectric resonators, and vortex waves. Moving on to chapter 3, it includes a discussion about the generation of vortex waves, while chapter 4 examines the steerability of vortex waves. Then, chapter 5 deals with the reduction of the OAM beam divergence. After that, chapter 6 exhibits a new application in the technology of RFID.

In chapter 3, in order to generate OAM waves, three techniques are assigned for discussion and evaluation. The first two approaches deploy a uniform circular antenna array UCA and elliptical patch antenna, whereas the third one is a new approach that uses crossed 2λ-dipole antennas. The UCA approach is characterized by the ability to produce any OAM mode order with the help of a Butler matrix, in contrast to the crossed 2λ-dipole antennas which are only able to generate the first OAM mode order. In addition, the UCA is also distinguished by its capability to increase the gain through enhancing the number of antenna elements or changing the type of antenna to a highly directional antenna yielding a reduction in the OAM beam divergence. On the other side, the elliptical antenna approach is featured by the simple and low cost structure, but suffers from the difficulty of setting the feeding point. The new approach provides a simple system with the aid of 2λ-dipole antennas. However, due to the mismatching there is a necessity for an additional matching circuit to avoid reflections at the feeding point. As a conclusion, the

UCA approach is selected to be used in the following chapters.

In chapter 4, the steerability of the OAM beam has been demonstrated. Similar to the directional beam of a phased array antenna, by changing the phase shift between each pair of adjacent antennas the vortex beam can be steered solving the issue of misalignment between an OAM transmitter and the OAM receiver. Therefore, the UCA approach is simulated and evaluated with and without subarrays. At first, a UCA with 8 antenna elements has been studied and evaluated showing an advantage of lower side lobe level due to separation of the antennas d_0 of $\lambda/2$. Whereas the UCA with a rectangular subarray among two other subarray (linear and circular) exhibits a larger steering angle. Also, the scheme with subarray can reduce of the OAM beam divergence.

In chapter 5, the issue regarding the OAM beam divergence, which is critical for some OAM applications, has been discussed and solved by the aid of a tailored lens and reflector. The tailored lens shows better performance when compared to the other cases with and without conventional lens. Same as for the tailored reflector, it exhibits the same behavior when it is compared to the cases in the presence and absence of a conventional reflector. Moreover, when higher OAM mode order is employed and the radius of the antenna array set to be increased, the two tailored components prove to be particularly advantageous over the others due to their conservation in material consumption. These two tailored components demonstrate that the vortex waves require a special lens or a special reflector to reduce the beam divergence effectively depending on all OAM mode orders.

In chapter 6, the number of RFID coded tags has been increased by using helically arranged cylindrical dielectric resonator arrays declaring the unique use of the vortex waves in the field of RFID technology. Moreover, the backscattered waves arriving from the environment can interrupt the entire RFID system in opposition to the one in the presence of this helical arrangement which do not suffer from this issue announcing a clutter rejection. Also, the helical arrangement shows the ability to convert the incident OAM mode order propagating in the direction of the helical arrangement to reach a reflected OAM mode order. This chapter has pointed out a way to develop the area of RFID through usage of the vortex waves.

7.2 Future Work

In this section, some promising research topics are mentioned here for future work:

- **Multi mode crossed 2λ-dipole antennas with matching circuit**: The idea of the crossed 2λ-dipole antennas is very promising especially in emitting OAM waves which are characterized by a simple and cost-effective approach. Unfortunately, it can only radiate the first OAM mode order and requires some matching circuits. Therefore, the proposed solution for these issues is to build the crossed dipole antennas on a multi-layer PCB [80] with one feeding point for the entire system, followed by a power splitter [77] to divide the incident power into several desirable number of ports. Then, a balun [81] is required to change the balanced signal to unbalanced one to optimize the feeding of the dipole antennas. After that, an essential matching circuit like the stripline stub [82] or a butterfly stub [83] is applied to compensate the mismatching between the microstip line and the dipole antenna. Moreover, a transition is critical in order to convert the microstrip line into another type of feeding line such as coplanar waveguide [84] in which the mentioned microstrip line normally requires a ground plane. Finally, the feeding lines go through vertical interconnect access (VIA) into another layer to avoid the collision with the other feeding lines.

- **Highly OAM beam steerability with higher side lobe level**: In this work, the subject of the OAM beam steerability is evaluated in which valid results are obtained with the UCA in the rectangular subarray. However, better results can be achieved by using a very highly directional antenna elements with very low side lobes yielding a reduction in the beam divergence and providing more steerability.

- **Reduction of the size of the tailored lens and tailored reflector**: The tailored lens and tailored reflector have demonstrated superior results in comparison to the conventional ones. However, the big size of the lens and the reflector should be minimized to make the two tailored components much more effective, compact and cost-effective. Therefore, the concept of the Fresnel lens can be studied and investigated to reduce the sizes of the tailored lens and reflector.

- **OAM mode order conversion with metasurfaces**: The concept of the helically arranged dielectric resonator arrays has proposed a solution to increase the number of the RFID codes in addition to reducing the environmental distortion. Nevertheless, this concept has some weaknesses, such as the low RCS of the DR additionally on the difficult configuration of the helical arrangement in which the height h (6.2) and the pitch p are a critical point particularly if the DR is very small and the operating frequency is very high. The lower

RCS can be solved by enhancing the number of DRs oder by adding a lens. Furthermore, the metasurfaces can be a solution for the difficult configuration, where it is made on one layer.

List of Publications

Journal Papers

[1] M. Haj Hassan, B. Sievert, J. T. Svejda, A. Alhaj Abbas, A. Jiménez-Sáez, A. Mostafa Ahmed, M. Schüßler, A. Rennings, K. Solbach, T. Kaiser, R. Jakoby, A. Sezgin, and D. Erni, "OAM mode order conversion and clutter rejection with OAM-coded RFID tags", *IEEE Access*, vol. 8, pp. 218729-218738, 2020, doi: 10.1109/ACCESS.2020.3043053.

[2] M. Haj Hassan, B. Sievert, J. T. Svejda, A. Mostafa Ahmed, J. Barowski, A. Rennings, I. Rolfes, A. Sezgin, and D. Erni, "Beam divergence reduction of vortex waves with a tailored lens and a tailored reflector", *IEEE Access*, vol. 9, pp. 9800-9811, 2021, doi: 10.1109/ACCESS.2021.3050043.

[3] A. Alhaj Abbas, M. Haj Hassan, A. Abuelhaija, D. Erni, K. Solbach and T. Kaiser, "Retrodirective dielectric resonator tag with polarization twist signature for clutter suppression in self-localization system", *IEEE Trans. Microw. Theory Techn.*, vol. 69, no. 12, pp. 5291-5299, Dec. 2021, doi: 10.1109/TMTT.2021.3108151.

Conference Papers

[1] M. Haj Hassan, B. Sievert, A. Rennings and D. Erni, "Reducing the divergence of vortex waves with a lens tailored to the utilized circular antenna array", in *2019 2nd Int. Workshop Mob. Terahertz Syst. (IWMTS)*, Bad Neuenahr, Germany, 2019, pp. 1-4.

[2] M. Haj Hassan, M. Al-Mulla, B. Sievert, A. Rennings and D. Erni, "Evaluation of different phased array approaches for orbital angular momentum beam steering", in *2020 Ger.*

Microw. Conf. (GeMiC), Cottbus, Germany, 2020, pp. 44-47.

[3] M. Haj Hassan, A. Alhaj Abbas, A. Jiménez-Sáez, A. Mostafa Ahmed, B. Sievert, M. Schüßler, A. Rennings, K. Solbach, T. Kaiser, R. Jakoby, A. Sezgin, and D. Erni, "Passive orbital angular momentum RFID tag based on dielectric resonator arrays", in *2020 3rd Int. Workshop Mob. Terahertz Syst. (IWMTS)*, Essen, Germany, 2020, pp. 1-4.

[4] M. Haj Hassan, B. Sievert, A. Rennings and D. Erni, "Generation of vortex waves using crossed 2λ-dipole antennas", in *2021 15th Eur. Conf. Antennas Propag. EuCAP. (EuCAP)*, Düsseldorf, Germany, 2021, pp. 1-3.

Bibliography

[1] C. A. Balanis, *Antenna Theory: Analysis and Design*, John Wiley & Sons, 2005.

[2] N. Oshima, K. Hashimoto, S. Suzuki, and M. Asada, "Terahertz wireless data transmission with frequency and polarization division multiplexing using resonant-tunneling-diode oscillators," *IEEE Trans. THz Sci. Technol.*, vol. 7, no. 5, pp. 593–598, 2017.

[3] I. T. Haque and C. Assi, "Profiling-based indoor localization schemes," *IEEE Syst. J.*, vol. 9, no. 1, pp. 76–85, 2015.

[4] X. Chen, D. Feng, S. Takeda, K. Kagoshima, and M. Umehira, "Experimental validation of a new measurement metric for radio-frequency identification-based shock-sensor systems," *IEEE J. Radio Freq. Identif.*, vol. 2, no. 4, pp. 206–209, 2018.

[5] J. Kim, M. H. Jeon, Y. Cho, and A. Kim, "Dark synthetic vision: lightweight active vision to navigate in the dark," *IEEE Robot. Autom. Lett.*, vol. 6, no. 1, pp. 143–150, 2021.

[6] P. W. Son, S. G. Park, Y. Han, and K. Seo, "Eloran: resilient positioning, navigation, and timing infrastructure in maritime areas," *IEEE Access*, vol. 8, pp. 193708–193716, 2020.

[7] Y. Zhang, H. Mu, T. Xiao, Y. Jiang, and C. Ding, "SAR imaging of multiple maritime moving targets based on sparsity bayesian learning," *IET Radar, Sonar Navig.*, vol. 14, no. 11, pp. 1717–1725, 2020.

[8] D. Parveg, M. Varonen, A. Safaripour, P. Kangaslahti, M. Kantanen, T. Tikka, T. Gaier, K. A. I. Halonen, and A. Hajimiri, "An mm-wave CMOS I–Q subharmonic resistive mixer for wideband Zero-IF receivers," *IEEE Microw. Wireless Compon. Lett.*, vol. 30, no. 5, pp. 520–523, 2020.

[9] N. Zhang and L. Belostotski, "A demonstration of a voltage-controlled inductor in a D-band colpitts third-harmonic-extracted injection-locked oscillator," *IEEE Microw. Wireless Compon. Lett.*, vol. 30, no. 10, pp. 969–972, 2020.

[10] D. K. Panda, R. Singh, T. R. Lenka, T. T. Pham, R. T. Velpula, B. Jain, H. Q. T. Bui, and H. P. T. Nguyen, "Single and double-gate based AlGaN/GaN MOS-HEMTs for the design of low-noise amplifiers: a comparative study," *IET Circuits Devices Syst.*, vol. 14, no. 7, pp. 1018–1025, 2020.

[11] N. Ginzberg, D. Regev, and E. Cohen, "Digital evolution of the quadrature balanced power amplifier transceiver for full duplex wireless operation," *IEEE Solid-State Circuits Lett.*, vol. 3, pp. 434–437, 2020.

[12] H. Zhu, X. Zhu, Y. Yang, and Y. Sun, "Design of miniaturized on-chip bandpass filters using inverting-coupled inductors in (Bi)-CMOS technology," *IEEE Trans. Circuits Syst. I: Regular Papers*, vol. 67, no. 2, pp. 647–657, 2020.

[13] B. Cetinoneri, Y. A. Atesal, and G. M. Rebeiz, "An 8×8 butler matrix in 0.13-μm CMOS for 5–6-GHz multibeam applications," *IEEE Trans. Microw. Theory Techn.*, vol. 59, no. 2, pp. 295–301, 2011.

[14] M. Cho, I. Song, and J. D. Cressler, "A two-way wideband active SiGe BiCMOS power divider/combiner for reconfigurable phased arrays with controllable beam width," *IEEE Access*, vol. 8, pp. 2578–2589, 2020.

[15] N. Buadana, S. Jameson, and E. Socher, "A multiport chip-scale dielectric resonator antenna for CMOS THz transmitters," *IEEE Trans. Microw. Theory Techn.*, vol. 68, no. 9, pp. 3621–3632, 2020.

[16] L. Allen, M. W. Beijersbergen, R. J. C. Spreeuw, and J. P. Woerdman, "Orbital angular momentum of light and the transformation of Laguerre-Gaussian laser modes," *Phys. Rev. A*, vol. 45, no. 11, pp. 8185–8189, 1992.

[17] J. Yang, H. Liu, J. Wen, F. Pang, N. Chen, Z. Chen, and T. Wang, "Excitation and transmission of 12 OAM modes in 3.7-km-long ring fiber with high refractive index difference," in *2018 Asia Commun. and Photon. Conf. (ACP)*, Hangzhou, China, 2018, pp. 1–4.

[18] W. Zhang, S. Zheng, X. Hui, R. Dong, X. Jin, H. Chi, and X. Zhang, "Mode division multiplexing communication using microwave orbital angular momentum: An experimental study," *IEEE Antennas Wireless Propag. Lett.*, vol. 16, no. 2, pp. 1308–1318, 2017.

[19] W. Brullot, M. K. Vanbel, T. Swusten, and T. Verbiest, "Resolving enantiomers using the optical angular momentum of twisted light," *Sci. Adv.*, vol. 2, no. 3, 2016.

[20] G. Xie, H. Song, Z. Zhao, G. Milione, Y. Ren, C. Liu, R. Zhang, C. Bao, L. Li, Z. Wang, K. Pang, D. Starodubov, B. Lynn, M. Tur, and A. E. Willner, "Using a complex optical orbital-angular-momentum spectrum to measure object parameters," *Opt. Lett*, vol. 42, no. 21, pp. 4482–4485, Nov 2017.

[21] H. Okuda and H. Sasada, "Huge transverse deformation in nonspecular reflection of a light beam possessing orbital angular momentum near critical incidence," *Opt. Express*, vol. 14, no. 18, pp. 8393–8402, Sep 2006.

[22] K. Liu, Y. Cheng, Z. Yang, H. Wang, Y. Qin, and X. Li, "Orbital-angular-momentum-based electromagnetic vortex imaging," *IEEE Antennas Wireless Propag. Lett.*, vol. 14, pp. 711–714, 2015.

[23] K. Liu, Y. Cheng, Z. Yang, H. Wang, Y. Qin, and X. Li, "Orbital-angular-momentum-based electromagnetic vortex imaging," *IEEE Antennas Wireless Propag. Lett.*, vol. 14, pp. 711–714, 2015.

[24] M. P. J. Lavery, S. M. Barnett, F. C. Speirits, and M. J. Padgett, "Observation of the rotational doppler shift of a white-light, orbital-angular-momentum-carrying beam backscattered from a rotating body," *Optica*, vol. 1, no. 1, pp. 1–4, Jul 2014.

[25] K. Y. Bliokh and F. Nori, "Transverse and longitudinal angular momenta of light," *Phys. Rep.*, vol. 592, pp. 1–38, 2015, Transverse and longitudinal angular momenta of light.

[26] F. Qin, L. Li, Y. Liu, W. Cheng, and H. Zhang, "A four-mode OAM antenna array with equal divergence angle," *IEEE Antennas Wireless Propag. Lett.*, vol. 18, no. 9, pp. 1941–1945, 2019.

[27] M. Zahn, *Electromagnetic Field Theory: a Problem Solving Approach*, Wiley, 1979.

[28] H. Henke, *Elektromagnetische Felder: Theorie und Anwendung*, Springer-Verlag, 2015.

[29] D. M. Pozar, *Microwave Engineering*, John Wiley & Sons, 2012.

[30] A. D. Johnson, V. Manohar, S. B. Venkatakrishnan, and J. L. Volakis, "Low-cost S-band reconfigurable monopole/patch antenna for cubesats," *IEEE Open J. Antennas Propag.*, vol. 1, pp. 598–603, 2020.

[31] Z. He, H. Lin, and C. Liu, "Codesign of a Schottky diode's and loop antenna's impedances for dual-band wireless power transmission," *IEEE Antennas Wireless Propag. Lett.*, vol. 19, no. 10, pp. 1813–1817, 2020.

[32] Y. Cui, R. Li, and P. Wang, "A novel broadband planar antenna for 2G/3G/LTE base stations," *IEEE Trans. Antennas Propag.*, vol. 61, no. 5, pp. 2767–2774, 2013.

[33] Y. Rahmat-Samii, J. Huang, B. Lopez, M. Lou, E. Im, S. L. Durden, and K. Bahadori, "Advanced precipitation radar antenna: array-fed offset membrane cylindrical reflector antenna," *IEEE Trans. Antennas Propag.*, vol. 53, no. 8, pp. 2503–2515, 2005.

[34] M. Sonkki, D. Pfeil, V. Hovinen, and K. R. Dandekar, "Wideband planar four-element linear antenna array," *IEEE Antennas Wireless Propag. Lett.*, vol. 13, pp. 1663–1666, 2014.

[35] A. Rolland, N. T. Nguyen, R. Sauleau, C. Person, and L. Le Coq, "Smooth-walled lightweight Ka-band shaped horn antennas in metallized foam," *IEEE Trans. Antennas Propag.*, vol. 60, no. 3, pp. 1245–1251, 2012.

[36] W. Wiesbeck, A. Herschlein, D. Löffler, and C. Fischer, *Antennen und Antennensysteme*, Skriptum zur Vorlesung, Universität Karlsruhe, 2005.

[37] O. S. Ginting, Chairunnisa, and A. Munir, "Side lobe level suppression for L-band array antenna using binomial power distribution," in *2017 3rd Int. Conf. Wirel. Telemat. (ICWT)*, Palembang, Indonesia, 2017, pp. 7–10.

[38] A. Falahati, M. NaghshvarianJahromi, and R. M. Edwards, "Wideband fan-beam low-sidelobe array antenna using grounded reflector for dect, 3G, and ultra-wideband wireless applications," *IEEE Trans. Antennas Propag.*, vol. 61, no. 2, pp. 700–706, 2013.

[39] J. C. S. Chieh, E. Yeo, R. Farkouh, A. Castro, M. Kerber, R. B. Olsen, E. J. Merulla, and S. K. Sharma, "Development of flat panel active phased array antennas using 5G silicon rfics at Ku- and Ka-bands," *IEEE Access*, vol. 8, pp. 192669–192681, 2020.

[40] K. Petermann, *Hochfrequenztechnik I vorlesungsskript*, TU Berlin, 2013.

[41] P. L. E. Uslenghi, "Optical behavior of elliptical lenses made of DNG metamaterial," *IEEE Antennas Wireless Propag. Lett.*, vol. 9, pp. 566–567, 2010.

[42] A. V. Boriskin, A. Vorobyov, and R. Sauleau, "Two-shell radially symmetric dielectric lenses as low-cost analogs of the luneburg lens," *IEEE Trans. Antennas Propag.*, vol. 59, no. 8, pp. 3089–3093, 2011.

[43] J. Thornton and K.-C. Huang, *Modern Lens Antennas for Communications Engineering*, John Wiley & Sons, 2013.

[44] M. R. Dehghani Kodnoeih, Y. Letestu, R. Sauleau, E. Motta Cruz, and A. Doll, "Compact folded fresnel zone plate lens antenna for mm-wave communications," *IEEE Antennas Wireless Propag. Lett.*, vol. 17, no. 5, pp. 873–876, 2018.

[45] G. Mishra, S. K. Sharma, J. S. Chieh, and R. B. Olsen, "Ku-band dual linear-polarized 1-D beam steering antenna using parabolic-cylindrical reflector fed by a phased array antenna," *IEEE Open J. Antennas Propag.*, vol. 1, pp. 57–70, 2020.

[46] L. Periasamy and A. J. Gasiewski, "Antenna design and prelaunch performance of a low-cost 118.75 GHz temperature sounding cubesat radiometer with 3-D-printed corrugated feed and offset reflector optics," *IEEE Trans. Antennas Propag.*, vol. 68, no. 6, pp. 4881–4893, 2020.

[47] H. Li, C. Li, S. Zheng, H. Gao, and G. Fang, "Design of a multiple-beam Cassegrain antenna with quasi-optical isolator at 200 GHz for target tracking," *IEEE Antennas Wireless Propag. Lett.*, vol. 19, no. 10, pp. 1779–1783, 2020.

[48] A. Garcia-Pino, N. Llombart, B. Gonzalez-Valdes, and O. Rubinos-Lopez, "A bifocal ellipsoidal Gregorian reflector system for THz imaging applications," *IEEE Trans. Antennas Propag.*, vol. 60, no. 9, pp. 4119–4129, 2012.

[49] S. Li, Y. Wang, M. Yu, and A. Panariello, "Efficient modeling of Ku-band high power dielectric resonator filter with applications of neural networks," *IEEE Trans. Microw. Theory Techn.*, vol. 67, no. 8, pp. 3427–3435, 2019.

[50] Eilert Berglind and Gunnar Björk, "Humblet's decomposition of the electromagnetic angular moment in metallic waveguides," *IEEE Trans. Microw. Theory Techn.*, vol. 62, no. 4, pp. 779–788, 2014.

[51] S. M. Mohammadi, L. K. S. Daldorff, J. E. S. Bergman, R. L. Karlsson, B. Thide, K. Forozesh, T. D. Carozzi, and B. Isham, "Orbital angular momentum in radio—a system study," *IEEE Trans. Antennas Propag.*, vol. 58, no. 2, pp. 565–572, 2010.

[52] K. Liu, Y. Cheng, Y. Qin, X. Li, and Y. Jiang, "Study on the unusual features of OAM beams and vortex electromagnetic fields," in *2017 6th Asia-Pac. Conf. Antennas Propag. (APCAP)*, Xi'an, China, 2017, pp. 1–3.

[53] T. Yuan, H. Wang, Y. Qin, and Y. Cheng, "Electromagnetic vortex imaging using uniform concentric circular arrays," *IEEE Antennas Wireless Propag. Lett.*, vol. 15, pp. 1024–1027, 2016.

[54] S.N. Khonina, V.V. Kotlyar, M.V. Shinkaryev, V.A. Soifer, and G.V. Uspleniev, "The phase rotor filter," *J. Mod. Opt.*, vol. 39, no. 5, pp. 1147–1154, 1992.

[55] K. Sueda, G. Miyaji, N. Miyanaga, and M. Nakatsuka, "Laguerre-Gaussian beam generated with a multilevel spiral phase plate for high intensity laser pulses," in *2005 Quantum Electronics and Laser Sci. Conf.*, Baltimore, USA, 2005, vol. 3, pp. 1567–1569.

[56] E. Doumanis, D. Zelenchuk, V. Fusco, and G. Goussetis, "Conical horn antenna with spiral phase plate for difference pattern generation," in *2013 7th Eur. Conf. Antennas Propag. (EuCAP)*, Gothenburg, Sweden, 2013, pp. 1309–1312.

[57] M. Caño-García, X. Quintana, and J.M. Otón et al., "Dynamic multilevel spiral phase plate generator," *Sci. Rep. 8*, 2018.

[58] F. E. Mahmouli and S. D. Walker, "4-Gbps uncompressed video transmission over a 60-GHz orbital angular momentum wireless channel," *IEEE Wireless Commun. Lett.*, vol. 2, no. 2, pp. 223–226, 2013.

[59] N. Wei and H. F. Ma, "Microwave vortex beam generation using holographic artificial impedance surface," in *2018 Cross Strait Quad-Reg. Radio Sci. Wirel. Technol. Conf. (CSQRWC)*, Xuzhou, China, 2018, pp. 1–3.

[60] C. Kai, P. Huang, F. Shen, H. Zhou, and Z. Guo, "Orbital angular momentum shift keying based optical communication system," *IEEE Photon. J.*, vol. 9, no. 2, pp. 1–10, 2017.

[61] H. Xu, H. Liu, X. Ling, Y. Sun, and F. Yuan, "Broadband vortex beam generation using multimode Pancharatnam–Berry metasurface," *IEEE Trans. Antennas Propag.*, vol. 65, no. 12, pp. 7378–7382, 2017.

[62] K. Liu, W. Guo, G. Wang, H. Li, and G. Liu, "A novel broadband Bi-functional metasurface for vortex generation and simultaneous RCS reduction," *IEEE Access*, vol. 6, pp. 63999–64007, 2018.

[63] W. Luo, S. Sun, H.-X. Xu, Q.g He, and L. Zhou, "Transmissive ultrathin Pancharatnam-Berry metasurfaces with nearly 100% efficiency," *Phys. Rev. Appl.*, vol. 7, 04 2017.

[64] W.-J. Byun, Y.-S. Lee, B. S. Kim, K. S. Kim, M. S. Kang, and Y. H. Cho, "Simple generation of orbital angular momentum modes with azimuthally deformed Cassegrain subreflector," *Electron. Lett.*, vol. 51, no. 19, pp. 1480–1482, 2015.

[65] W. J. Byun and Y. Heui Cho, "Analysis of a 200-GHz OAM radio link using a generalized Friis transmission equation," in *2019 IEEE Int. Symp. Antennas Propag. USNC-URSI Radio Sci. Meet. APSURSI 2019 - Proc.*, Atlanta, USA, 2019, pp. 1051–1052.

[66] E. Mari, F. Spinello, M. Oldoni, R. A. Ravanelli, F. Romanato, and G. Parisi, "Near-field experimental verification of separation of OAM channels," *IEEE Antennas Wireless Propag. Lett.*, vol. 14, pp. 556–558, 2015.

[67] M. Barbuto, A. Toscano, and F. Bilotti, "Single patch antenna generating electromagnetic field with orbital angular momentum," in *2013 IEEE Antennas Propag. Soc. Int. Symp. (APSURSI)*, Orlando, USA, 2013, pp. 1866–1867.

[68] C. Guo, X. Zhao, C. Zhu, P. Xu, and Y. Zhang, "An OAM patch antenna design and its array for higher order OAM mode generation," *IEEE Antennas Wireless Propag. Lett.*, vol. 18, no. 5, pp. 816–820, 2019.

[69] M. Barbuto, M. Miri, A. Alù, F. Bilotti, and A. Toscano, "A topological design tool for the synthesis of antenna radiation patterns," *IEEE Trans. Antennas Propag.*, vol. 68, no. 3, pp. 1851–1859, 2020.

[70] T. Yuan, Y. Cheng, H. Wang, and Y. Qin, "Beam steering for electromagnetic vortex imaging using uniform circular arrays," *IEEE Antennas Wireless Propag. Lett.*, vol. 16, pp. 704–707, 2017.

[71] S. Gao, W. Cheng, H. Zhang, and Z. Li, "High-efficient beam-converging for UCA based radio vortex wireless communications," in *2017 IEEE/CIC Int. Conf. Commun. China (ICCC)*, Qingdao, China, 2017, pp. 1–6.

[72] M. Haj Hassan, B. Sievert, A. Rennings, and D. Erni, "Generation of vortex waves using crossed 2λ-dipole antennas," in *2021 15th Eur. Conf. Antennas Propag. (EuCAP)*, Düsseldorf, Germany, 2021, pp. 1–3.

[73] M. Haj Hassan, M. Al-Mulla, B. Sievert, A. Rennings, and D. Erni, "Evaluation of different phased array approaches for orbital angular momentum beam steering," in *2020 Ger. Microw. Conf. (GeMiC)*, Cottbus, Germany, 2020, IEEE, pp. 44–47.

[74] M. Haj Hassan, B. Sievert, A. Rennings, and D. Erni, "Reducing the divergence of vortex waves with a lens tailored to the utilized circular antenna array," in *2019 2nd Int. Workshop Mob. Terahertz Syst. (IWMTS)*, Bad Neuenahr, Germany, 2019, pp. 1–4.

[75] M. Haj Hassan, B. Sievert, J. T. Svejda, A. Mostafa Ahmed, J. Barowski, A. Rennings, I. Rolfes, A. Sezgin, and D. Erni, "Beam divergence reduction of vortex waves with a tailored lens and a tailored reflector," *IEEE Access*, vol. 9, pp. 9800–9811, 2021.

[76] A. Bisognin, N. Nachabe, C. Luxey, F. Gianesello, D. Gloria, J. R. Costa, C. A. Fernandes, Y. Alvarez, A. Arboleya-Arboleya, J. Laviada, F. Las-Heras, N. Dolatsha, B. Grave, M. Sawaby, and A. Arbabian, "Ball grid array module with integrated shaped lens for 5G backhaul/fronthaul communications in F-band," *IEEE Trans. Antennas Propag.*, vol. 65, no. 12, pp. 6380–6394, Dec 2017.

[77] L. Weisgerber and A. E. Popugaev, "Multibeam antenna array for RFID applications," *2013 Eur. Microw. Conf.*, pp. 84–87, 2013.

[78] M. Haj Hassan, A. Alhaj Abbas, A. Jiménez-Sáez, A. Mostafa Ahmed, B. Sievert, M. Schüßler, A. Rennings, K. Solbach, T. Kaiser, R. Jakoby, A. Sezgin, and D. Erni, "Passive orbital angular momentum RFID tag based on dielectric resonator arrays," in *2020 3rd Int. Workshop Mob. Terahertz Syst. (IWMTS)*, Essen, Germany, 2020, pp. 1–4.

[79] M. Haj Hassan, B. Sievert, J. T. Svejda, A. Alhaj Abbas, A. Jiménez-Sáez, A. Mostafa Ahmad, M. Schüßler, A. Rennings, K. Solbach, T. Kaiser, R. Jakoby, A. Sezgin, and D. Erni, "OAM mode order conversion and clutter rejection with OAM-coded RFID tags," *IEEE Access*, vol. 8, pp. 218729–218738, 2020.

[80] M. Mosalanejad, I. Ocket, C. Soens, and G. A. E. Vandenbosch, "Multi-layer PCB Bow-Tie antenna array for (77–81) GHz radar applications," *IEEE Trans. Antennas Propag.*, vol. 68, no. 3, pp. 2379–2386, 2020.

[81] W. Tang, S. W. Qu, and S. Yang, "Dual-polarized ultrawideband eleven antenna fed by modified passive balun," *IEEE Antennas Wireless Propag. Lett.*, vol. 19, no. 9, pp. 1600–1604, 2020.

[82] W.-H. Tu and K. Chang, "Wide-band microstrip-to-coplanar stripline/slotline transitions," *IEEE Trans. Microw. Theory Techn.*, vol. 54, no. 3, pp. 1084–1089, 2006.

[83] B. T. Tan, J. J. Yu, S. T. Chew, M. . Leong, and B.-L. Ooi, "A miniaturized dual-mode ring bandpass filter with a new perturbation," *IEEE Trans. Microw. Theory Techn.*, vol. 53, no. 1, pp. 343–348, 2005.

[84] T. B. Kumar, K. Ma, and K. S. Yeo, "A 60-GHz coplanar waveguide-based bidirectional LNA in SiGe BiCMOS," *IEEE Microw. Wireless Compon. Lett.*, vol. 27, no. 8, pp. 742–744, 2017.

[85] J. D. Jackson, *Classical Electrodynamics*, John Wiley & Sons, New York, 1962.

[86] K. Liu, X. Li, Y. Gao, H. Wang, and Y. Cheng, "Microwave imaging of spinning object using orbital angular momentum," *J. Appl. Phys.*, vol. 122, no. 12, pp. 124903, 2017.

[87] C. Zhang and L. Ma, "Millimetre wave with rotational orbital angular momentum," *Sci. Rep.*, vol. 6, pp. 1–8, 2016.

[88] T. Nguyen, R. Zenkyu, M. Hirabe, T. Maru, and E. Sasaki, "A study of orbital angular momentum generated by parabolic reflector with circular array feed," in *2016 Int. Symp. Antennas Propag. (ISAP)*, Okinawa, Japan, 2016, IEEE, pp. 708–709.

[89] W. J. Byun and Yo. H. Cho, "Generation of an orbital angular momentum mode based on a Cassegrain reflectarray antenna," in *2017 IEEE Antennas Propag. Soc. Int. Symp. USNC/URSI Natl. Radio Sci. Meet.*, San Diego, USA, 2017, IEEE, pp. 1191–1192.

DOI: 10.17185/duepublico/76528
URN: urn:nbn:de:hbz:465-20220824-110358-4